



Deliverable 7.3: Technical report on thermal effects on near field properties

Work Package 7

The project leading to this application has received funding from the European Union's Horizon 2020 research and innovation programme under grant agreement No 847593.



<http://www.ejp-urad.eu/>

Document information

Project Acronym	EURAD
Project Title	European Joint Programme on Radioactive Waste Management
Project Type	European Joint Programme (EJP)
EC grant agreement No.	847593
Project starting / end date	1st June 2019 – 30 May 2024
Work Package No.	7
Work Package Title	Influence of temperature on clay-based material behaviour
Work Package Acronym	HITEC
Deliverable No.	7.3
Deliverable Title	Technical report on thermal effects on near field properties
Lead Beneficiary	[CNRS (ULorraine)]
Contractual Delivery Date	October 2023
Actual Delivery Date	June 2024
Type	Final report of WP7 Task 2.1
Dissemination level	Public
Authors	Dragan GRGIC [CNRS (ULorraine)], Pierre BESUELLE [CNRS (UGrenoble)], Robert CUSS [UKRI-BGS]

To be cited as

Grgic, D., Bésuelle, P. & Cuss, R., 2023. Technical report on thermal effects on near field properties. Final version as of 01.11.2023 of deliverable D7.3 of the HORIZON 2020 project EURAD. EC Grant agreement no: 847593.

Disclaimer

All information in this document is provided "as is" and no guarantee or warranty is given that the information is fit for any particular purpose. The user, therefore, uses the information at its sole risk and liability. For the avoidance of all doubts, the European Commission has no liability in respect of this document, which is merely representing the authors' view.

Acknowledgement

This document is a deliverable of the European Joint Programme on Radioactive Waste Management (EURAD). EURAD has received funding from the European Union's Horizon 2020 research and innovation programme under grant agreement No 847593.

Status of deliverable		
	By	Date
Delivered (Lead Beneficiary)	[CNRS (ULorraine)]	1 November 2023
Verified (WP Leader)	Markus Olin [VTT]	15 February 2024
Reviewed (Reviewers)	Robert Charlier [ULiege]	10 March 2024
	Nico Kampman	9 May 2024
Approved (PMO)	Bharti.Reddy	31 May 2024
Submitted to EC	Andra (Coordinator)	03 June 2024

Authors

Organisation	Name	E-mail
[CNRS (ULorraine)]	Dragan Grgic	dragan.grgic@univ-lorraine.fr
[CNRS (UGrenoble)]	Pierre Bésuelle	pierre.besuelle@3sr-grenoble.fr
[UKRI-BGS]	Robert Cuss	rjcu@bgs.ac.uk

Table of content

Executive Summary.....	6
List of Figures.....	8
List of Tables.....	12
Glossary.....	13
1. Introduction.....	14
2. CNRS (ULorraine).....	18
2.1 Introduction.....	18
2.2 Material and methods.....	18
2.2.1 Material and sampling.....	18
2.2.2 Experimental devices and procedures.....	19
2.2.2.1 Experimental device.....	19
2.2.2.2 Experimental protocols.....	20
2.2.2.3 3D X-Ray Tomography: Acquisition and Analysis.....	21
2.2.2.4 Permeability Measurements.....	21
2.2.3 Research plan.....	22
2.3 Results and discussion.....	23
2.3.1 Experimental results.....	23
2.3.1.1 Influence of the sample orientation on the self-sealing process.....	23
2.3.1.2 Influence of the calcite content on the self-sealing process.....	24
2.3.1.3 Influence of the crack aperture on the self-sealing process.....	26
2.3.1.4 Influence of temperature on the self-sealing process.....	28
2.3.2 Discussion.....	33
2.3.2.1 Influence of the calcite content.....	33
2.3.2.2 Influence of sample orientation and crack aperture.....	34
2.3.2.3 Influence of temperature.....	35
2.4 Conclusion.....	36
3. CNRS (UGrenoble).....	37
3.1 Introduction.....	37
3.2 Material and methods.....	37
3.2.1 Material and sampling.....	37
3.2.2 Experimental devices and procedures.....	37
3.2.3 Research plan.....	38
3.3 Results and discussion.....	38
3.3.1 Test 3 at 90°C and parallel to the bedding.....	38
3.3.2 Test 1 at 25°C and parallel to the bedding.....	42



3.4	Conclusion.....	45
4.	UKRI-BGS	47
4.1	Introduction.....	47
4.2	Material and methods.....	48
4.2.1	Material and sampling.....	48
4.2.2	Experimental devices and procedures	50
4.2.2.1	The Heated Shear Rig (HSR)	50
4.2.2.2	Testing protocol.....	55
4.2.2.3	Fracture surface scanner	57
4.2.2.4	Fracture Roughness Measurements.....	57
4.2.2.5	Calculation of fracture transmissivity	59
4.2.2.6	Calculation of self-sealing potential (SSP).....	59
4.2.2.7	Calibration	60
4.2.3	Research plan.....	60
4.1	Results and discussion	61
4.1.1	Example test: OPA2065 (FPR_23_055) – Opalinus Clay	62
4.1.1.1	Initial shear.....	62
4.1.1.2	Flow stage.....	64
4.1.1.3	Repeat shear.....	66
4.1.1.4	Results from test OPA2065	69
4.1.2	Comparison of all tests	70
4.1.3	Repeatability in Opalinus Clay.....	70
4.1.4	Influence of temperature on shear strength in Opalinus Clay	74
4.1.5	Self-sealing potential of Opalinus Clay	75
4.1.6	Fracture topology of sheared Opalinus Clay	76
4.1.7	Repeat shear in Opalinus Clay	77
4.1.8	Results for Callovo-Oxfordian claystone	78
4.2	Conclusion.....	80
5.	General conclusions	83
	Acknowledgements	85
	References	85

Executive Summary

The overall aim of the work package EURAD-WP7 HITEC (“Influence of temperature on clay-based material behaviour”) of the European Joint Programme on Radioactive Waste Management (EURAD) is to improve the Thermo-Hydro-Mechanical (THM) description of the clay-based materials – host clay rock and bentonite buffer - at elevated temperatures. Within this WP, Task 2 is focussing on the behaviour of the clay host rocks at temperatures of up to 120°C to help to optimise the repository design. Indeed, the heat generated by waste must not affect the favourable properties of the host rock, especially its transport properties, for containment. The overpressure generated by the difference between thermal expansion coefficient of pore water and the solid rock skeleton may have deleterious consequences. In the near field (i.e., in the vicinity of the cell) characterised by a fractured zone, this could induce fracture opening or propagation in this fractured zone, altering the permeability. Laboratory experiments in subtask 2.1 were performed to provide answers about the impact of heating on the self-sealing processes in the near-field. Different testing cells (triaxial, oedometric and shear ring) and monitoring tools (X-ray and neutron tomography) have been used by the different partners to analyse, at different test stages and temperatures, the evolution of crack volume and permeability of fractured samples due to water percolation. The materials used in this study were: Callovo Oxfordian claystone (COx), Opalinus clay (OPA) and Boom clay.

CNRS (ULorraine) analysed the self-sealing process in the Callovo-Oxfordian claystone by performing self-sealing tests on initially (artificially) fractured samples under different temperatures with water injection. Cylindrical samples oriented in parallel and perpendicularly to the bedding plane with an artificial initial fracture were used in a triaxial compression cell transparent to X-rays. Water permeability was measured and the evolution of cracks volume was analysed from X-ray tomography 3D images to characterize the self-sealing process. All tests performed at 20 °C with water injection showed a rapid drop in permeability at the beginning followed by a progressive decrease and a stabilization after one month. The permeability of fractured samples decreases significantly after self-sealing but is still higher (by 2 orders of magnitude) than the permeability of healthy claystone. Otherwise, the less calcite the sample contains (i.e., the more clayey it is), the faster the crack self-seals. The smaller the opening of the initial crack is, the faster the water permeability decreases and the crack closes. No significant influence of the sample orientation on the self-sealing kinetic was identified at this stage. Finally, temperature doesn't seem to have a significant impact on the self-sealing process (permeability decrease and crack volume reduction).

CNRS (UGrenoble) carried out a comparative study of self-sealing at different temperatures (between 25 and 90°C) to investigate the re-sealing phenomenon in Callovo-Oxfordian clay rock. The samples, which had an initial opening, were monitored throughout the test under in operando conditions, using tomography with simultaneous combined x-ray and neutron imaging. X-ray tomography was used to quantify variations in mass density and, combined with digital image correlation (DIC), to quantify the kinematic field (in particular the volume strain field). Neutron tomography is used to quantify the presence of water in the material, as neutron absorption is very sensitive to the hydrogen in water. The samples were first heated (outside the tomography line) and then, once installed in the tomograph, synthetic water (with in situ salinity) was injected into the initial crack. Scans were taken every fifteen minutes for several hours. The comparative analysis revealed similarities and differences in the sealing process, depending on the temperature. Reclosure of the initial crack is fairly rapid, taking a few hours. However, if we reason in terms of mass density, the density of the material filling the initial crack does not reach the density of the sound material during the few hours of testing. The self-sealing process is a multi-stage process, with a rapid filling phase and a slower process, which could not be studied here. One difference attributed to temperature concerns the self-sealing mechanisms. At room temperature, the filling of the initial crack is induced by the formation of a dense network of secondary micro-cracks in the vicinity of the initial crack, forming a highly damaged material that fills the empty space. There is also swelling of the material in the remainder of the sample. At a temperature of 90°C, the self-sealing process is essentially attributed to diffuse swelling of the material in the sample, the amplitude of which is greater than at room temperature. Secondary cracking, as described at room temperature, is not

observed here, or only sporadically. The neutron tomography images show that, in both cases, the initial crack opening is replaced by a material with a slightly higher water content than the intact material and that the water propagates through the sample, accompanying the swelling process.

UKRI-BGS performed self-sealing experiments in Opalinus Clay (OPA) and Callovo-Oxfordian claystone (COx). Starting with intact cylindrical sample, a shear-fracture was created at the mid-plane in a direct shear apparatus. The addition of an injection bore then allowed synthetic pore fluid to be delivered directly to the fracture plane to monitor flow. The decrease in initial flow to a steady value determined the self-sealing potential (SSP) from hydration, while comparing flow on the static fracture with changes in flow as a result of shear determined the self-sealing potential from shear. Two batches of experiments were conducted: the first had fractures formed at ambient temperatures, which were then tested for flow at elevated temperatures between 20 and 90°C. The second batch had the fracture and flow parts of the experiment both conducted at temperature. Temperature was seen to have a considerable effect on the shear properties of OPA and COx, with peak strength and shear modulus increasing with temperature. Self-sealing potential as a result of hydration and shear was seen to reduce to a negligible amount at 90 °C in both OPA and COx. In COx, two orders of magnitude reduction in SSP as a result of hydration was seen. The study has shown the favourable self-sealing properties of OPA and COx reduces with temperature and becomes almost negligible at 90 °C.

List of Figures

CNRS (ULorraine)

Figure 1 - Geometry of the artificially fractured cylindrical samples ($\varnothing = 20$ mm ; h = 40 mm) for self-sealing tests.....	18
Figure 2 - PEEK triaxial compression cell for self-sealing tests in an X-ray nano-tomograph.	20
Figure 3 - Triaxial compression cell made of PEEK: scheme (with the cylindrical sample inside) and photo.....	20
Figure 4 - Evolution of water permeability of parallel sample EST63744-7 and perpendicular sample EST63744-11 during self-sealing test at 20°C.	23
Figure 5 - X-ray 3D tomography images of perpendicular sample EST63744-11 showing the evolution of the crack volume with time (initial crack opening = 0.4 mm) during self-sealing test at 20°C (Day 0-: after hydrostatic loading; Day 0+: after crack saturation).....	23
Figure 6 - X-ray 3D tomography images of parallel sample EST63744-7 showing the evolution of the crack volume with time (initial crack opening = 0.4 mm) during self-sealing test at 20°C (Day 0-: after hydrostatic loading; Day 0+: after crack saturation).	24
Figure 7 - X-ray 3D tomography images of perpendicular sample EST59996-71 showing the evolution of the crack volume with time (initial crack opening = 0.4 mm) during self-sealing test at 20°C (Day 0-: after hydrostatic loading; Day 0+: after crack saturation).....	25
Figure 8 - X-ray 3D tomography images of perpendicular sample EST60007-71 showing the evolution of the crack volume with time (initial crack opening = 0.4 mm) during self-sealing test at 20°C (Day 0: after hydrostatic loading).	25
Figure 9 - X-ray 3D tomography images of perpendicular sample EST60018-71 showing the evolution of the crack volume with time (initial crack opening = 0.4 mm) during self-sealing test at 20°C (Day 0-: after hydrostatic loading; Day 0+: after crack saturation).....	26
Figure 10 - Evolution of water permeability of parallel sample EST60766-3 and parallel sample EST62690-2 during self-sealing test at 20°C.	27
Figure 11 - X-ray 3D tomography images of parallel sample EST60766-3 showing the evolution of the crack volume with time (initial crack opening = 0.4 mm) during self-sealing test at 20°C (Day 0-: after hydrostatic loading; Day 0+: after crack saturation).	27
Figure 12 - X-ray 3D tomography images of parallel sample EST62690-2 showing the evolution of the crack volume with time (initial crack opening = 0.8 mm) during self-sealing test at 20°C (Day 0: after hydrostatic loading).	28
Figure 13 - Evolution of water permeability during self-sealing tests on parallel sample EST66418-10 at 80°C and parallel sample EST66727-05 at 40 °C, compared to parallel sample EST60766-3 at 20°C.	29
Figure 14 - X-ray 3D tomography images of parallel sample EST66418-10 showing the evolution of the crack volume with time (initial crack opening = 0.4 mm) during a self-sealing test at 80 °C (Day 0-: after hydrostatic loading; Day 0+: after crack saturation).....	29
Figure 15 - X-ray 3D tomography images of parallel sample EST66727-05 showing the evolution of the crack volume with time (initial crack opening = 0.4 mm) during a self-sealing test at 40 °C (Day 0-: after hydrostatic loading; Day 0+: after crack saturation).....	30

Figure 16 - Evolution of water permeability during self-sealing tests on perpendicular sample EST66723-12 at 80°C and perpendicular sample EST66721-17 at 40 °C, compared to perpendicular sample EST66721-13 at 20°C. 31

Figure 17 - X-ray 3D tomography images of perpendicular sample EST66723-12 showing the evolution of the crack volume with time (initial crack opening = 0.4 mm) during a self-sealing test at 80 °C (Day 0- : after hydrostatic loading; Day 0+: after crack saturation)..... 31

Figure 18 - X-ray 3D tomography images of perpendicular sample EST66721-17 showing the evolution of the crack volume with time (initial crack opening = 0.4 mm) during a self-sealing test at 40 °C (Day 0- : after hydrostatic loading; Day 0+: after crack saturation)..... 32

Figure 19 - X-ray 3D tomography images of perpendicular sample EST66721-13 showing the evolution of the crack volume with time (initial crack opening = 0.4 mm) during a self-sealing test at 20 °C (Day 0- : after hydrostatic loading; Day 0+: after crack saturation)..... 32

Figure 20 – Top: volume variation percentage of the initial crack (normalized with the volume after hydrostatic loading) obtained from X-ray tomography 3D images during all self-sealing tests with water, for parallel (left) and perpendicular (right) orientations. Bottom: volume variation percentage of the initial crack at the end of the test as a function of the calcite content for both orientations. 33

CNRS (UGrenoble)

Figure 1 – Scheme and photograph of the cell developed for tests with dual x-ray and neutron CT. ... 37

Figure 2 – Test at 90°C, time evolution of a horizontal x-ray tomographic section at mid-height..... 39

Figure 3 – Test at 90°C, time evolution of a vertical x-ray tomographic section. 39

Figure 4 – Test at 90°C, (a) evolution with time of the interface volume ; (b) profiles of x-ray absorption across the interface and (small) evolution with time of the minimum if x-ray absorption in the interface. 40

Figure 5 – Test at 90°C, evolution of a horizontal neutron tomographic section at mid-height. 40

Figure 6 – Test at 90°C, evolution of a vertical neutron tomographic section..... 41

Figure 7 – Test at 90°C, profiles of neutron absorption across the interface. 41

Figure 8 – Test at 90°C, vertical projection (average) of the volume strain field. 42

Figure 9 – Test at 90°C, horizontal projection (average) of the volume strain field. 42

Figure 10 – Test at 25°C, time evolution of a horizontal x-ray tomographic section at mid-height..... 43

Figure 11 – Test at 25°C, time evolution of a vertical x-ray tomographic section. 43

Figure 12 – Test at 25°C, (a) time evolution of the interface volume; (b) profiles of x-ray absorption across the interface and (small) evolution with time of the minimum if x-ray absorption in the interface. 43

Figure 13 – Test at 25°C, time evolution of a horizontal neutron tomographic section at mid-height. . 44

Figure 14 – Test at 25°C, time evolution of a vertical neutron tomographic section..... 44

Figure 15 – Test at 25°C, profiles of neutron absorption across the interface..... 44

Figure 16 – Test at 25°C, vertical projection (average) of the volume strain field. 45

Figure 17 – Test at 25°C, horizontal projection (average) of the volume strain field. 45

UKRI- BGS

Figure 1 - Callovo-Oxfordian Claystone sample being cut on a lathe during the careful sample preparation process. 48

Figure 2 - Schematic of the Heated Shear Rig (HSR). 51

Figure 3 - Components of the Heated Shear Rig. a) Photo of the complete apparatus; b) Loading frame with normal load cells at the bottom; c) normal load ram (yellow); d) sample assembly, shear load cell and horizontal displacement sensor. 52

Figure 4 - Sample holder arrangement. a) cylindrical sample of rock; b) sample holder; c) sample holder and sample; d) sample holder and lower block arrangement; e) complete sample holder arrangement. 53

Figure 5 - Components of the heating system of the Heated Shear Rig. a) Heating cartridge; b) Heating cartridge installed into the base of the shear bath; c) Band heater. 54

Figure 6 - Temperature distribution measured in the sample assembly when heated by cartridges alone, showing a considerable undesired temperature gradient. 54

Figure 7 - Graphical summary of the test stages. 55

Figure 8 - Laser scanning of fracture surfaces. a) NextEngine 3D Scanner HD; b) Revopoint MINI 3D Scanner. 57

Figure 9 - Summary of stages involved in analysis of measured profile to obtain a roughness profile (From ASTM standard, 2009). 58

Figure 10 - Initial shear stage of test OPA2065. a) Stress response; b) Normal stress; c) Normal displacement; d) Temperature of the sample. 63

Figure 12 - Topology of the fracture of test OPA2065 after initial shearing. 64

Figure 13- Flow shear stage of test OPA2065. a) Stress response; b) Normal stress; c) Normal displacement; d) Temperature of the sample; e) Shear movement. 65

Figure 14 - Flow during test OPA2065. a) Flow; b). Detail of flow; c) Log of flow. 66

Figure 15 - Repeat shear stage of test OPA2065. a) Stress response; b) Normal stress; c) Normal displacement; d) Temperature of the sample. 67

Figure 16 - Comparison of shear test results for both shear tests conducted on sample OPA2065. ... 68

Figure 18 - Topology of the fracture of test OPA2065 after re-shearing. a) Bottom fracture face; b) Top fracture face. 69

Figure 19 - Repeatability of shear data in Opalinus Clay. a) Repeatability tests; b) All tests initially sheared at ambient temperature. 74

Figure 20 - Shear stress-strain result for four tests conducted over a range of temperatures in Opalinus Clay. 75

Figure 21 - Relationship between shear properties and temperature for Opalinus Clay. a) Peak shear strength; b) Shear modulus; c) residual strength. 75

Figure 22 - Influence of temperature on self-sealing potential. a) Self-sealing potential as a result of hydration; b) Self-sealing potential as a result of active shear. 76

Figure 23 - Surface analysis of the laser scan data from Opalinus Clay. a) Roughness; b) RMS roughness; c) Peak to valley height. 77

Figure 24 - Relationship between shear properties and temperature for repeat shearing in Opalinus Clay. a) Peak shear strength; b) Shear modulus; c) Residual strength. 78

Figure 25 - Shear stress-strain result for four tests conducted over a range of temperatures in Callovo-Oxfordian claystone..... 79

Figure 26 - Relationship between shear properties and temperature for Callovo-Oxfordian claystone. a) Peak shear strength; b) Shear modulus; c) Residual strength..... 79

Figure 27 - Influence of temperature on self-sealing potential in Callovo-Oxfordian claystone. a) Self-sealing potential as a result of hydration; b) Self-sealing potential as a result of active shear..... 80

List of Tables

CNRS (ULorraine)

Table 1 - Composition of Andra’s synthetic water.....	19
Table 2 - References of the different samples with corresponding characteristics and experimental conditions.....	22

CNRS (UGrenoble)

Table 1 - Experimental program of self-sealing characterization.....	38
--	----

UKRI- BGS

Table 1 - Reference Boom Clay pore water after De Craen et al. (2004).....	49
Table 2 - Recipe for making Boom Clay synthetic pore water.....	50
Table 3 - Recipe for making Callovo-Oxfordian claystone synthetic pore water.....	50
Table 4 - Pore-water chemistry used as test fluid on all samples, from Pearson (2003).....	50
Table 5 - Description of test stages.....	56
Table 6 - List of parameters calculated to describe surface characteristics of a test fracture.....	58
Table 7 - Planned experimental programme.....	61
Table 8 - Summary of experiments completed. Note: tests in red have yet to be conducted and will be complete by the end of the project.....	61
Table 9 - Results for test OPA2065.....	69
Table 10 - Results for all tests. Note: OPA – Opalinus Clay; COx – Callovo-Oxfordian claystone; + good test; - incomplete test.....	72
Table 11 - Fracture roughness results for all tests. Note: OPA – Opalinus Clay; COx – Callovo-Oxfordian claystone.....	73

Glossary

BC	Boom Clay
COx	Callovo-Oxfordian claystone
EDZ	Excavation Damaged Zone
HLW	High-Level Waste
HSR	Heated Shear Rig
OPA	Opalinus Clay
SSP	Self-sealing potential
WP	Work Package

1. Introduction

The WP7 “Influence of Temperature on Clay-based Material Behaviour” of the EURAD Project aims to develop and document an improved thermo-hydro-mechanical (THM) understanding of clay-based materials (host rocks and buffers) exposed at high temperatures (>100°C) or having experienced high temperature transients for extended durations. The heat generated by waste must not affect the favourable properties of the host rock, especially its transport properties, for containment. The overpressure generated by the difference between thermal expansion coefficient of pore water and the solid rock skeleton may have deleterious consequences. In far field (subtask 2.2), this could induce rock damage and reactivate fractures/faults. In the near field (subtask 2.1), i.e., in the vicinity of the cell, characterised by a fractured zone, this could induce fracture opening or propagation, altering the permeability. Laboratory experiments in subtasks 2.1 and 2.2 investigate the near-field and far-field effects of heating on the properties and behaviour of the host rocks and in subtask 2.3 several THM models are developed and improved.

Thus, the main objective is to increase knowledge of the THM behaviour of clay host rock to help to optimise the repository design. More specifically, from experiments (for both near and far fields), modelling and benchmarking, the following questions will be addressed:

- Do we sufficiently understand the processes leading to the observed overpressures and changes in the stress state? How can experiments be best designed to characterise the most sensitive parameters?
- How good are the current THM models in representing the stress changes at repository-relevant conditions?
- What are the THM criteria that can act as credible site-specific design criteria? The basic assumption is that no irreversible or long-term damage to the rock should occur. How can one best demonstrate that these design criteria can be met?
- In the very unlikely case of damaging (fracturing) the rock, what will be the consequences and can we expect self-sealing in clay rich rock to occur as soon as the energy is released?

The characterisation of in-situ THM behaviour of the clay host rock is significant for the design of the underground nuclear waste disposal facility and to provide long-term safety. When temperature increases in a low-permeability medium, the pore water is compressed as a consequence of the difference between its thermal expansion coefficient and that of the solid skeleton of the rock, which leads to an overpressure. An improved knowledge of the THM behaviour will help to optimise repository design (spacing in between HLW cells, load on casing/canister).

In the near field (**subtask 2.1**), the excavation of galleries or micro tunnels creates a fractured zone around them. The evolution of the effective stress field in the vicinity of the galleries due to the temperature rise can induce fracture opening or propagation of the excavation-induced fractured zone. The temperature rise can also affect the crack self-sealing process in the claystone. From a mechanistic point of view, the self-sealing capacity of fractured claystone is associated with various thermo-hydro-mechanical and -chemical processes and controlled by the prevailing state conditions. Mechanical closure of fractures (e.g., crack closure, fracture sliding) and hydro-chemical interactions of the pore water with the clay-bearing solid phase of the geomaterial (e.g., swelling, disaggregation) have been identified as typical self-sealing mechanisms in clay-rich materials.

The present report “D7.3 - Technical report on thermal effects on near field properties” is the final deliverable for **subtask 2.1**. It is based on laboratory experiments to provide answers about the effects of increased temperature on fracturing and self-sealing processes in the excavated-damaged zone. The impact of temperature on the self-sealing processes (evolution of crack volume and permeability) will be investigated experimentally using X-ray and neutron tomography scanning on fractured samples at different test stages and temperatures to analyse the closure of fractures under heat and water percolation.

Excavation of underground galleries (such as radioactive waste repository) in rocks creates generally a network of cracks near the excavation zone called an Excavation Damaged Zone (EDZ). Indeed, the stress that was supported by the material removed during construction must be taken up by the remaining rock, leading to stress concentrations and, in most of cases, the formation of fractures. In the Underground Research Laboratory (URL) of the National Agency of Radioactive waste Management (Andra) located in Meuse/Haute-Marne (Bure, France) and excavated in the Callovo-Oxfordian (COx) claystone, EDZs have been observed. This network of cracks desaturates the claystone and causes it to lose its mechanical and hydraulic (i.e., sealing) properties. However, over the lifetime of a disposal facility the temperature and saturation around the repository will evolve.

During the resaturation of clay-rich host rocks, the fractures generated during the excavation can self-seal and cause both a significant decrease in water permeability in the EDZ and a partial restoration of the mechanical properties of the rock (Bock et al. 2010). That phenomenon is called self-sealing. More precisely, sealing is the reduction of fracture permeability by any hydromechanical, hydrochemical or hydrobiochemical processes in the EDZ (Bastiaens et al. 2007). In contrast to healing, sealing is characterized by only part of the restoration of the initial rock properties. Healing corresponds to sealing with loss of memory of the pre-healing state; thus the healed fracture will not be a preferred site for new fracturing just because of its history (Bastiaens et al. 2007). Several authors have studied the phenomenon of cracks self-sealing in claystones induced by the percolation of water. For Auvray et al. (2015), self-sealing is a result of a rearrangement of minerals and porosity in the fracture region. For these authors, there are three main processes involved. The first is swelling between sheets of smectite phases (intraparticle swelling), the second is inter-particle swelling due to osmotic effects, and the last is plugging or blockage of the fractures by particle aggregation. These processes lead to structural rearrangement within the self-sealed zone, which in turn determines the hydromechanical and transfer properties of the sealed fracture zone. Furthermore, Bastiaens et al. (2007) and Van Geet et al. (2008) proposed a synthesis of several in situ experiments on Opalinus clay (indurated claystone) and Boom clay (plastic claystone) presenting the capabilities of these clays to self-seal rather than self-restore. Concerning the Callovo-Oxfordian claystone, De La Vaissière et al. (2015) have shown the partial restoration of its permeability during in-situ resaturation experiments. Over a one-year resaturation period, the hydraulic conductivity measured in the boreholes decreased by up to four orders of magnitude, approaching, but not reaching, the value of the healthy claystone. This result illustrated the ability of the COx claystone to self-seal. In addition, high temperatures in the near-field may have a deleterious effect on the performance (barrier to fluid flow) of the clay host rock. These effects can include permanent damage to the EDZ impacting the self-sealing capacity of the rock, alterations in hydromechanical behaviour caused by prolonged thermal heating and the generation of thermally induced pore water pressures.

In the context of radioactive waste disposal, knowing the long-term hydro-mechanical behaviour of the damaged area (EDZ) over time is of great importance. In addition, in the case where clay-based materials are fractured by the repository construction, the ability of clays to continue to self-seal will be critical for ensuring the performance of geological repositories for radioactive waste.

Table - Synthesis of partners experimental program in subtask 2.1.

Partner Material	[CNRS (ULorraine)]	[CNRS (UGrenoble)]	[UKRI- BGS]
COx	Self-sealing tests in triaxial cell	Self-sealing tests in oedometric cell	Self-sealing tests in shear ring
OPA			
Boom clay			

The Table above presents a synthesis of experiments to be performed by the different partners for subtask 2.1.

The materials used in this subtask 2.1 are:

- **Callovo Oxfordian claystone (COx)** taken in the clayey unit. Origin: The Industrial Centre for Geological Disposal (Cigeo) located at Bure (Meuse/Haute-Marne, France).

Callovo-Oxfordian (COx) claystone is the host rock chosen in France for the storage of radioactive waste, more precisely in Meuse/ Haute-Marne (Bure, France). It is 160 million years old and, with a thickness of about 130 m, and located under Bure at a depth of 400 to 600 m. The COx claystone is a very low permeability rock. Its mineral composition varies as a function of depth mainly due to geological sedimentary cycles (Lefranc et al. 2008) and the clay mineral content is roughly anti-correlated with the carbonate content. It corresponds to (Mohajerani 2011; Montes et al. 2004; Robinet et al. 2012, 2015; Sammartino et al. 2003): 20–60% of phyllosilicates (illite, interstratified illite/smectite, kaolinite, mica, chlorite), 10–40% of tectosilicates (quartz, feldspars), 15–80% of carbonates (calcite, dolomite), 0–3% of pyrite, iron oxides with less than one percent organic matter. The three main phases are clay minerals, quartz, and calcite (Yven *et al.* 2007). It is worth emphasizing that this argillite contains a high content of swelling clay minerals (smectites).

From the base to the top of the layer, the COx formation was divided into four lithostratigraphic units (C2a to C2d) and several petrophysical units (UA1, RIO, UA2, UA3, UT, USC1, RSO, and USC2) defined for the Andra project (Pellenard et al. 2014). The COx claystone consists mainly of three different layers to be more precise (Giot et al. 2019). There is the silto-carbonated unit (USC) which is on the top of the COx layer and is the most carbonated one. Its mineralogical composition is contrasted and variable; its porosity is about 15%. Then, there is the transition unit (UT), which is more homogeneous and with a clay content between 30 and 40%. The carbonate content increases from the bottom (20%) to the top (30%). Finally, there is the clay unit (UA), which is the most clayey unit, with clays, carbonate and quartz contents of about 45–50%, 27% and 24%, respectively. Armand *et al.* (2017) report that the UA unit makes up two-thirds of the total geological layer thickness.

The work of Andra (Andra 2005) showed that the pore space of the COx claystone represents about 18%. This porosity is made up of approximately 10% macropores (> 1 µm), 86% (0.1 µm to 1 µm) mesopores and 4% (< 1 µm) micropores according to the three classes listed in the work of Coll (2005). Initial stresses within the claystone are about 12 MPa at the level of the radioactive waste storage which corresponds to the lithostatic pressure at a depth of 500 m (Gratier et al. 2004). Water permeability tests (Andra 2005; Escoffier 2002) give values between $5 \cdot 10^{-20}$ and $5 \cdot 10^{-21}$ m².

- **Opalinus clay (OPA)**. Origin: Mont Terri underground laboratory (Mont Terri, Switzerland).

The Opalinus Clay (OPA) is a Jurassic (Aalenian, ~180 Ma) shallow marine clayshale found in Switzerland. The formation, named after the ammonite *Leioceras opalinum*, consists of indurated dark grey micaceous claystones (shales) that are subdivided into several lithostratigraphic units. Some of them contain thin sandy lenses, limestone concretions, or siderite nodules. The clay-mineral content ranges from 40 – 80 wt% (9 – 29 % illite, 3 – 10 % chlorite, 6 – 20% kaolinite, and 4 – 12 % illite/smectite mixed layers in the ratio 70/30). Other minerals are quartz (15 – 30 %), calcite (6 – 40 %), siderite (2 – 3 %), ankerite (0 – 3 %), feldspars (1 – 7 %), pyrite (1 – 3 %), and organic carbon (<1 %). The total water content ranges from 4 – 19 % (Gautschi, 2001). At the Mont Terri underground research laboratory, three facies can be distinguished: a shaly facies in the lower half of the sequence, a 15 metre thick sandy, carbonate-rich facies in the middle of the sequence and a sandy facies interstratified with the shaly facies in the upper part. For the current study, samples from the shaly facies were used. The

OPA at Mont Terri is an over-consolidated shale with a maximum burial depth of 1,200m and is presently around 280m depth.

- **Boom clay.** Origin: HADES Underground Research Laboratory (Mol, Belgium).

The geological and hydrogeological setting of the Boom Clay in northern Belgium has been summarised by Beerten & Leterme (2012) and in the Netherlands by Vis & Verweij (2014). The Boom Clay (usually referred to as the Rupel Clay in the Netherlands) is of lower Oligocene (ca 28 to 34 Ma) age and forms part of the Rupel Formation. In the Netherlands the Rupel Formation has been subdivided into the Vesseem, Rupel Clay and Steensel members (Wong *et al.*, 2007). These members are diachronous, with both the basal Vesseem and the overlying Steensel members being sandy marine deposits (Vis & Verweij; 2014) laid down close to the palaeo-shorelines. The Boom Clay is a pyritic, grey to dark brown marine clay with septarian (carbonate rich) concretions. Towards the basin margins the clays grade into sands. The formation reaches a maximum thickness of up to 250 m, with a mean thickness of around 65 m, and dips gently towards the north-east at between 1 and 2°.

The core material used in the current study was taken from the HADES underground research laboratory at Mol in Belgium. Here, the Boom Clay consists mainly of mixed clay and silt, with additional minor sand (Bernier & Bastiaens, 2007). Mineralogical composition of the Boom Clay is widely reported, predominantly assessed using XRD. The clay content is generally reported to vary from between 23 and 60 % of the bulk material composition and is predominantly made up of illite, smectite, and kaolinite, which is often seen in interlaminated zones (Blanchart *et al.*, 2012; Dehandschutter *et al.*, 2004; Wemaere *et al.*, 2008; Yu *et al.*, 2012). The non-clay fraction of the Boom Clay primarily consists of quartz, again widely reported to vary between 23 and 60 %. The remaining percentage of the non-clay fraction consists of feldspars, calcite, and pyrite. Honty & De Craen (2011) report the composition to be 22-77 % quartz, 0-6.3% albite, 0.4-17.3% k-feldspar, 0-1.5% siderite, 0-4.6% calcite, 0-2% apatite, 0.3-5% pyrite, 5-37% illite/muscovite, 6.8-35% smectite + illite/smectite, 2-16% kaolinite, and 14-4% chlorite. This demonstrates the variability of Boom Clay.

2. CNRS (ULorraine)

2.1 Introduction

The ability of claystone to self-seal has then been proven by several authors, but there are very little informations on the self-sealing process when the crack is subjected to different temperatures and fluids. Auvray et al. (2015) performed self-sealing tests on the COx argillite in a PEEK triaxial cell under room temperature but with only 2D X-ray scans. Giot et al. (2019) performed the same kind of tests with 3D X-ray scans but with a limited amount of data and basic voxel data analysis. The objective of our study is to analyse the impact of temperature, calcite content, sample orientation and initial crack width on the self-sealing process of artificial cracks in core samples of the COx claystone. To achieve these objectives, self-sealing tests with water injection under different temperatures, calcite contents, sample orientations and initial crack openings will be performed. 3D X-ray scans will be performed on all tested samples before, during and after the experiment and the voxel data will be analysed with a high-end software for the visualization and analysis of computed tomography (CT) data to estimate the evolution of the crack volume. In addition, water permeability will be measured continuously during all tests. To our knowledge, there are no similar studies in the literature that characterize the self-sealing process in clay host rocks under such different and complex conditions.

2.2 Material and methods

2.2.1 Material and sampling

Cylindrical samples of 20 mm diameter and 40 mm height were used for the self-sealing tests. They were cored from Andra's boreholes. Each core sample was preserved in a bell jar (with water at the bottom) to keep its water saturation level above 90%. Before each test, the samples were artificially fractured. In the first step, they were sawn in two along a plane containing the axis of the cylinder, and in the second step, one of the faces was machined to obtain a crack on a one-third of the diameter whose opening was controlled as precisely as possible. The opening of the artificial crack was carried out by milling with a high-precision tool. This regular milling method allows the creation of an artificial space without generating significant damage. In fact, a small number of particles are extracted from the matrix until the desired depth is reached. It is worth emphasizing that artificial crack realization induces a drying of the crack tips, which is probably moderate given that this process is relatively fast (about half an hour). In addition, the crack is rapidly resaturated during the first stage of the self-sealing test.

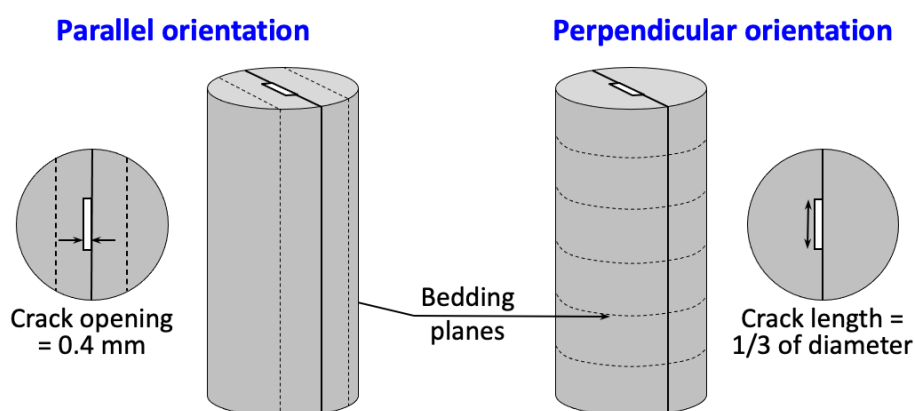


Figure 1 - Geometry of the artificially fractured cylindrical samples ($\varnothing = 20 \text{ mm}$; $h = 40 \text{ mm}$) for self-sealing tests.

For our tests, two orientations of the sample axis were considered, namely parallel and perpendicular to the bedding plane, to take into account the effect of the clay anisotropy. According to previous works

(Auvray et al. 2015; Giot et al. 2019) and Andra’s recommendations, we chose an aperture of 400 μm for the initial crack. We also tested a wider aperture (800 μm) to verify if self-sealing is also an efficient process for wide cracks. Figure 1 presents the geometry of the artificially cracked samples for both parallel and perpendicular orientations. Therefore, the initial crack has a theoretical initial volume equal to 106.5 mm^3 and 213 mm^3 for an aperture of 0.4 mm and 0.8 mm, respectively.

We used the synthetic water of Andra, the simple version for geomechanical experiments, whose chemical composition is close to the in situ porewater at the Andra URL and which is supposed to be sufficiently chemically balanced with the rock to prevent any structural damage due to geochemical reactions (the chemical composition is given in Table 1).

Table 1 - Composition of Andra’s synthetic water.

Chemical element	Content (g/l)
NaCl	1.950
NaHCO ₃	0.130
KCl	0.035
CaSO ₄ ,2H ₂ O	0.630
MgSO ₄ ,7H ₂ O	1.020
CaCl ₂ ,2H ₂ O	0.080
Na ₂ SO ₄	0.700

2.2.2 Experimental devices and procedures

2.2.2.1 Experimental device

We developed an innovative mini-triaxial cell with a height of 250 mm and a diameter of 100 mm in which cylindrical samples of a diameter of 20 mm and height of 40 mm can be tested. The particularity of this cell is that its body is made of PEEK CF30 (PolyEtherEtherKetone, 30% carbon fibers) and thus is transparent to X-rays, which made it possible to follow the evolution of the crack volume in the sample at different times under a high-resolution X-ray computed tomography (CT) scanner (Fig. 2). A confining pressure up to 12 MPa can be applied on the samples. At both end caps (outlets) of the cell, drainage holes allow to inject fluids (water) at different pressures in the sample.

The fluids are injected with pressure generators (syringe pumps) into these outlets using flexible connections and injection circuit connectors in PEEK material, which allows a 360° rotation of the sample in the X-ray tomography, and then 3D scans of the sample before, during and after the self-sealing test. During self-sealing tests, upstream and downstream fluids pressures and exchanged fluid volumes are continuously recorded with our high-precision syringe pumps, thus allowing the continuous measurement of fluid flow rate and then crack permeability.

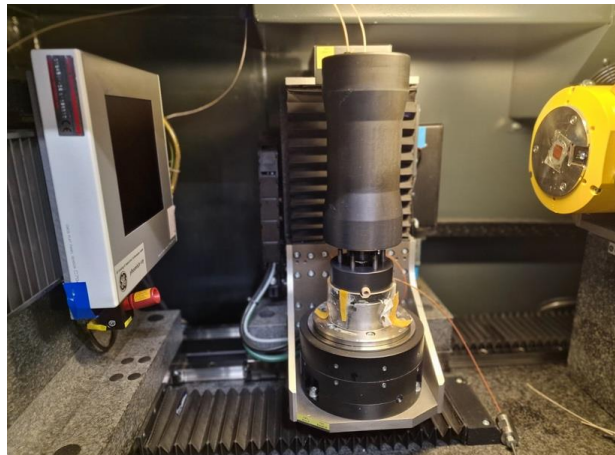


Figure 2 - PEEK triaxial compression cell for self-sealing tests in an X-ray nano-tomograph.

2.2.2.2 Experimental protocols

The artificially fractured samples (isolated from the confining oil by a waterproof Viton© membrane) is put in the triaxial cell and then the hydrostatic stress (i.e., confining pressure) is then increased to 4 MPa, which corresponds to the pressure applied on the galleries wall by swelling clays (bentonite) of the plug. This confining pressure is kept constant during the whole test. Once the confining pressure is stabilized, an initial 3D X-ray scan is performed to record the initial shape of the crack. Just after, synthetic water is injected from the bottom (upstream) of the sample at a constant rate of 0.05 ml/min to saturate the fracture. As soon as the water comes out of the cell at the top (downstream), the injection is stopped and a 3D X-ray scan is performed to analyze the crack just after its saturation with water. Then, water circulation is imposed in the fractured sample with a water pressure gradient of 0.2 MPa (upstream/bottom pressure = 1 MPa; downstream/top pressure = 0.8 MPa), with a flow rate limit of 0.02 ml/min to avoid too fast water circulation and fracture damage. A scheme (with a cylindrical sample inside) and a photo of a triaxial compression cell made of PEEK are represented in Fig. 3. Once steady state flow is achieved with a stable gradient pressure of 0.2 MPa, water permeability can be measured. This is obviously impossible at the beginning of the self-sealing test because the crack permeability is infinite (the crack is totally open). So far, all these steps are performed at room temperature (~20 °C).

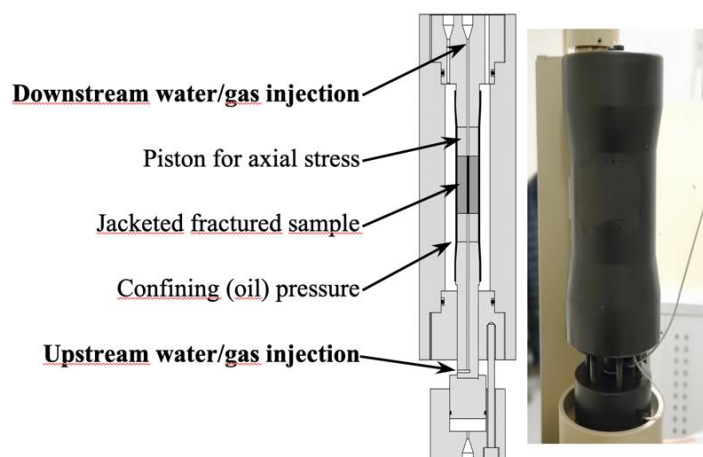


Figure 3 - Triaxial compression cell made of PEEK: scheme (with the cylindrical sample inside) and photo.

Concerning the self-sealing test under high temperature, the temperature is increased once the flow rate is stabilized. The temperature is controlled with a heating system around the triaxial cell (temperature regulated bath). For this test, only one additional 3D X-ray scan is performed, at the end of the experiment once the temperature has cooled.

2.2.2.3 3D X-Ray Tomography: Acquisition and Analysis

The PEEK triaxial cell is placed in a GE Phoenix Nanotom S CT scanner (Fig. 2) and 3D scans with a relatively high voxel resolution of 24 μm are performed at different times during each self-sealing test. The resolution is limited by the size (diameter) of the peek triaxial cell which imposes a relatively large distance between the X-ray source and the detector. This scanner is equipped with a 180 kV microfocus X-ray tube/generator and a CMOS 5 MPx detector. The scintillator type is: Hamamastu 2300 x 2300 CsI (iodure Cesium). The micro-focus and Flat CMOS systems enable high-definition X-ray images to be obtained at acquisition frequencies of 500 ms to several tens of minutes. The Phoenix CT scanner has an auto-protected chamber to enable safe access to the hydraulic circuits that generate the confining and water injection pressures in the triaxial cell. The acquisition parameters are: 1500 projections, 3 images per projection, image every 1000 ms, exposure time 1000 ms, which allows us to have at the end of the scan 1500 projections, voltage of 120 kV and intensity of 200 μA of the rays.

After 3D reconstruction of the sample volume, images were analysed with the VGStudio MAX Software (Volume Graphics GmbH). It allows to isolate and visualize the evolution of the fracture and to quantify the variations of its volume during the self-sealing test. The volume was estimated from the count of the voxels number assigned to the crack from the reconstructed sample. Here, the main issue was to discriminate the void from the rest of the sample after reconstruction (the void is filled with water). The method was based on porosity/inclusion analysis of VGSTUDIO MAX 3.5 working with the threshold only. Basically, it consists in:

- Overlay perfectly all the 3D scans of a sample using the tools of VGSTUDIO MAX 3.5: all the points are merged and put at the same scale. The only difference is at the crack surface.
- Determine the zone where the fracture is situated on the first 3D scan and extract this zone from all other scans.
- Once all the interest zones are extracted, determine the voids with the method based on porosity/inclusion analysis of VGSTUDIO MAX 3.5 with the threshold-only option on pore mode.

It is worth emphasizing that the software VG Studio Max helps the user to determine the threshold value. First, the user chooses the pixels corresponding to the background (voids or cracks in our case) and the pixels corresponding to the material (claystone in our case). Then, the software approximates the threshold value that varies from one scan to another. After all these steps are performed, the software gives us a lot of usable data such as total pore volume, connected pore volume, pore surface, and average pore radius. These pores represent the void in the crack (filled by water) and therefore allow us to have the volume of the crack during the self-sealing tests.

2.2.2.4 Permeability Measurements

The water permeability of the cracked samples was calculated from the volumes measured with the syringe pumps at both upstream and downstream sides of the sample during the self-sealing test. It is based on a steady-flow approach taking into consideration Darcy's law, which describes the flow across a porous medium induced by a pressure gradient:

$$k = \frac{Q\mu L}{S(P_u - P_d)} \quad (1)$$

where k is the intrinsic permeability (m^2), Q the volumetric flow rate (m^3s^{-1}) measured at both upstream and downstream sides of the sample, μ the liquid (water in our case) dynamic viscosity (Pa.s), S the

injection surface (cross section) of the sample (m^2), L the length of the sample (m), and P_u and P_d the upstream and downstream fluid pressures (Pa).

Since we are measuring the flow rate in a cracked porous sample and since the Darcy law describes the flow across a porous medium, the permeability k corresponds here to an “apparent permeability” of a cracked sample. But actually, since the matrix permeability of this claystone is very low (less than $10^{-20} m^2$), the measured permeability corresponds probably to the crack permeability.

It is worth emphasizing that the flow rate is very fast at the beginning of the self-sealing experiment because of the large crack aperture and the applied pressure gradient. Therefore, the Darcy law doesn't apply due to inertial forces and/or turbulence (Navier-Stokes flow). Anyway, it was never possible to measure the permeability at the beginning of the self-sealing experiments when the Darcy law doesn't apply. Indeed, as said previously, a water pressure gradient of 0.2 MPa, with a flow rate limit of 0.02 ml/min to avoid too fast water circulation and fracture damage, was applied in these experiments. Once steady state flow was achieved with a stable gradient pressure of 0.2 MPa, which wasn't possible at the beginning of the self-sealing test because the crack permeability is infinite (the crack is totally open), water permeability was measured.

2.2.3 Research plan

Ten samples were tested in total. The references of the different samples with corresponding characteristics and experimental conditions are given in Table 2. Each self-sealing test lasts at least one month.

Table 2 - References of the different samples with corresponding characteristics and experimental conditions.

Samples	%CaCO ₃	Solid grain density (g/cm ³)	Fracture opening (µm)	Orientation	Temperature (°C)
EST60766-3	21	2.67	400	//	20
EST62690-2	20.6	2.67	800	//	20
EST63744-7	32	2.69	400	//	20
EST66727-05	21	2.68	400	//	40
EST66418-10	25.4	2.69	400	//	80
EST63744-11	32	2.69	400	⊥	20
EST60007-71	52.8	2.71	400	⊥	20
EST60018-71	5.3	2.61	400	⊥	20
EST59996-71	68.1	2.71	400	⊥	20
EST66723-12	20.8	2.66	400	⊥	80

2.3 Results and discussion

2.3.1 Experimental results

2.3.1.1 Influence of the sample orientation on the self-sealing process

To observe the influence of the sample orientation on the self-sealing process, self-sealing tests were carried out (at room temperature) on samples with different orientations, i.e., parallel (EST63744-7) and perpendicular (EST63744-11) to the bedding plane, but with the same calcium carbonate (calcite) content (32%) and the same crack opening (400 μm). The evolution of the water permeability and the 3D scans of these two tests are presented in Figs. 4, 5 and 6.

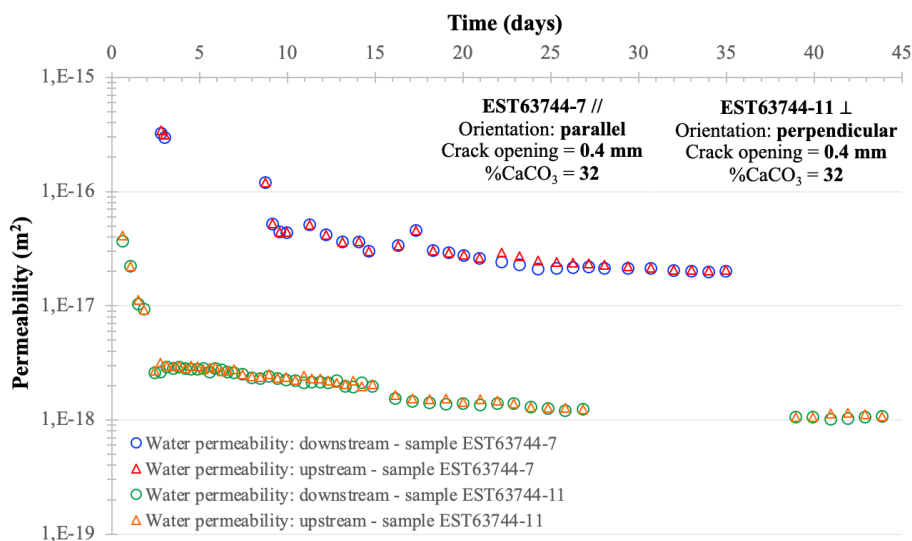


Figure 4 - Evolution of water permeability of parallel sample EST63744-7 and perpendicular sample EST63744-11 during self-sealing test at 20°C.

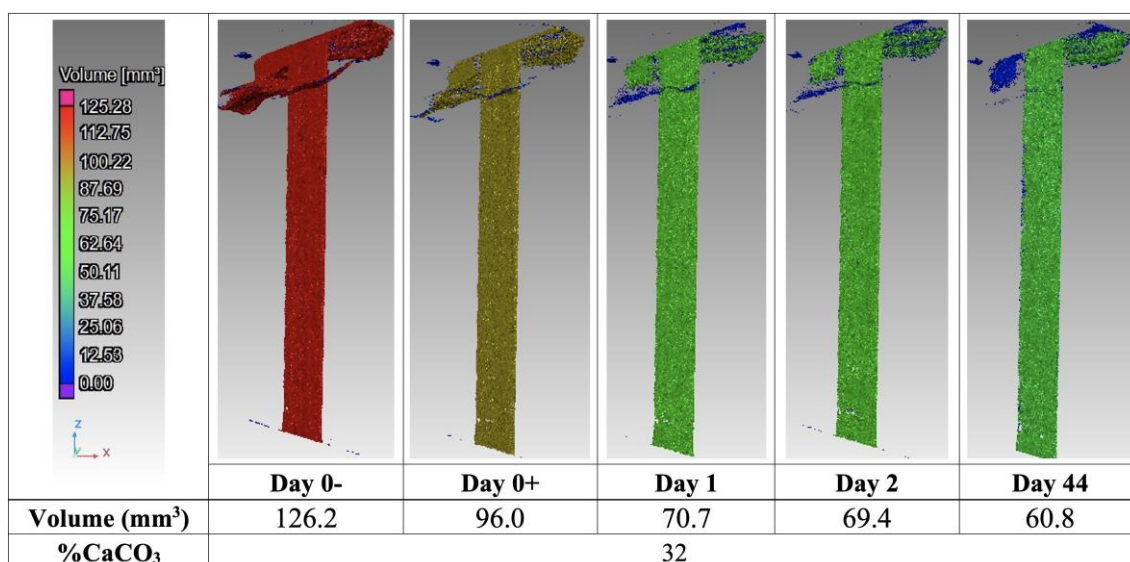


Figure 5 - X-ray 3D tomography images of perpendicular sample EST63744-11 showing the evolution of the crack volume with time (initial crack opening = 0.4 mm) during self-sealing test at 20°C (Day 0-: after hydrostatic loading; Day 0+: after crack saturation).

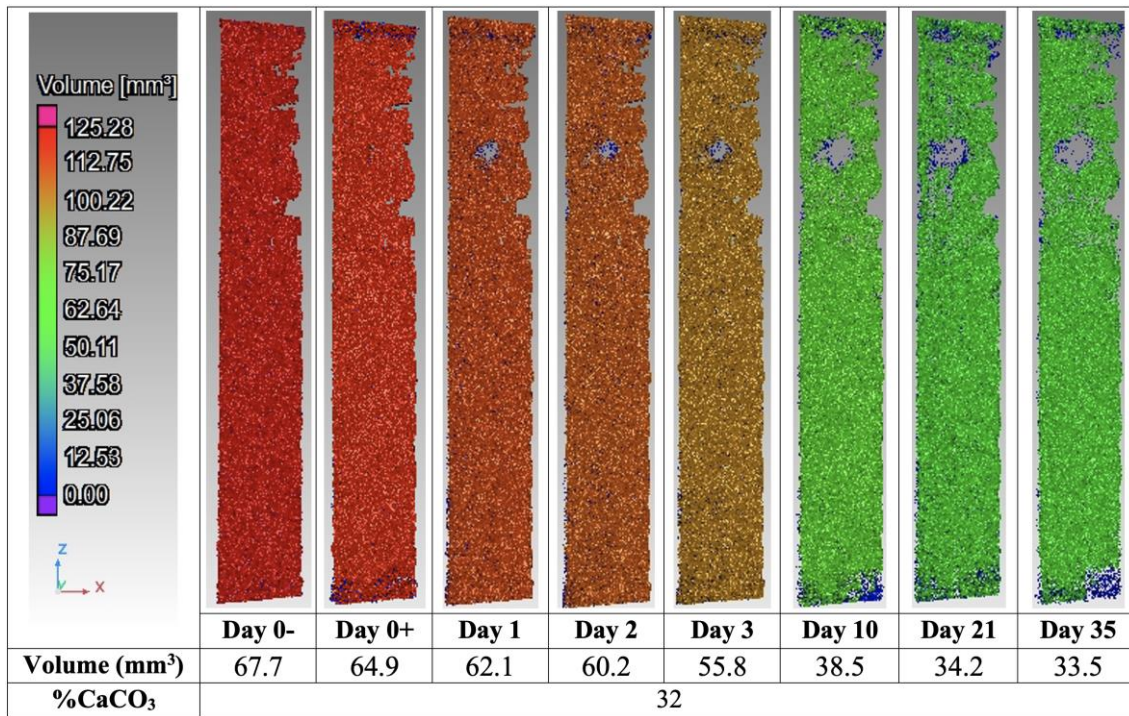


Figure 6 - X-ray 3D tomography images of parallel sample EST63744-7 showing the evolution of the crack volume with time (initial crack opening = 0.4 mm) during self-sealing test at 20°C (Day 0-: after hydrostatic loading; Day 0+: after crack saturation).

First, it is worth noting that the hydrostatic loading at a confining pressure of 4 MPa induces a partial closure of the initial crack. This mechanical closure is much more efficient for the parallel sample, probably because of the clay mineral’s orientation. The sample saturation induces also a partial closure of the initial crack. Contrary to what was supposed, the self-sealing process doesn’t seem more efficient for the parallel sample, i.e., when the bedding plane (and clay minerals alignment) is parallel to the axis of the sample and to the artificial fracture surface.

2.3.1.2 Influence of the calcite content on the self-sealing process

To observe the influence of the mineralogical composition (calcite content) of the COx on the self-sealing process, several tests were performed on core samples with an artificial crack aperture of 400 μm, parallel orientation, but with different carbonate contents. The self-sealing test performed on the specimen EST59996-71 with perpendicular orientation and a very high calcium carbonate content of 68.1% (crack opening = 400 μm) lasted 42 days. Figure 7 shows the evolution of the fracture geometry obtained from the analysis of 3D X-ray tomography images. Before water saturation (just after hydrostatic loading), the fracture volume was equal to 111 mm³. Just after crack saturation, it decreased to 98 mm³. After 14 days of the self-sealing experiment, the volume decreased a little (87 mm³). After 42 days, the volume was equal to 84 mm³. Thus, self-sealing was very moderate and the fracture remained globally open. Therefore, no water permeability measurements of the fracture could be performed since the flow rate was too fast.

The self-sealing test performed on specimen EST60007-71 with perpendicular orientation and a high calcium carbonate content of 52.8% (crack opening = 400 μm) lasted 25 days. Figure 8 shows the evolution of the fracture geometry obtained from the analysis of 3D X-ray tomography images. The self-sealing test was also very moderate for this perpendicularly oriented sample and the fracture remained globally open, as for the very carbonated sample EST59996-71. Therefore, no water permeability measurements of the fracture could be performed for this carbonated sample.

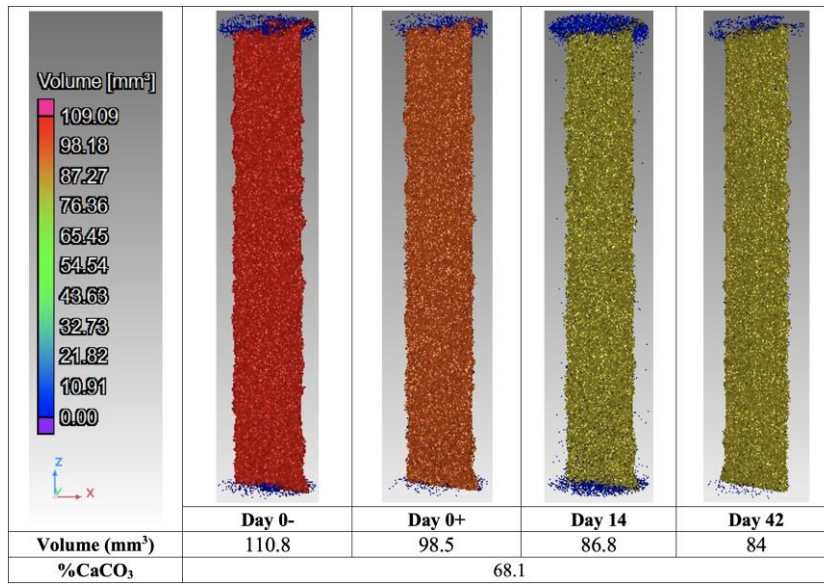


Figure 7 - X-ray 3D tomography images of perpendicular sample EST59996-71 showing the evolution of the crack volume with time (initial crack opening = 0.4 mm) during self-sealing test at 20°C (Day 0-: after hydrostatic loading; Day 0+: after crack saturation).

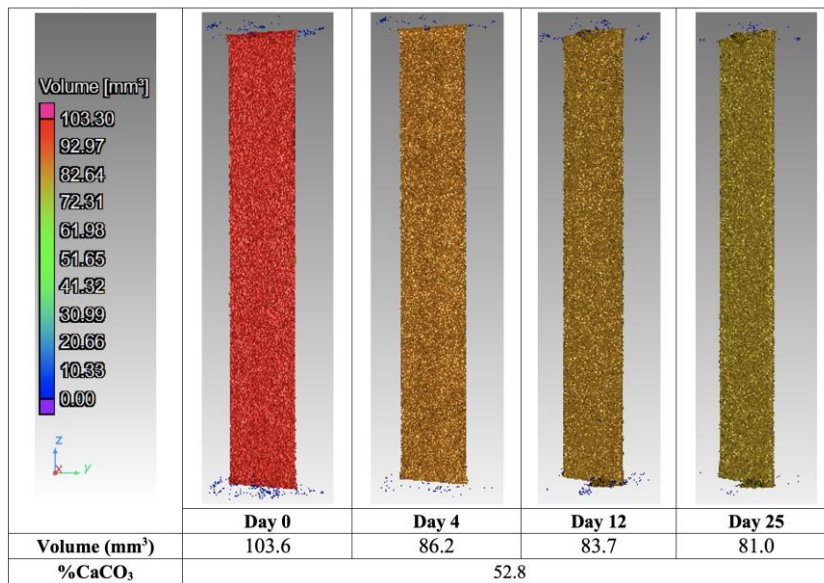


Figure 8 - X-ray 3D tomography images of perpendicular sample EST60007-71 showing the evolution of the crack volume with time (initial crack opening = 0.4 mm) during self-sealing test at 20°C (Day 0: after hydrostatic loading).

The self-sealing test performed on specimen EST60018-71 with perpendicular orientation and a very low calcium carbonate content of 5.3% (crack opening = 400 μm) lasted 21.4 days. The very rapid sealing induced the plugging of the inlet capillary, making further water injection and permeability measurement impossible, and stopped the self-sealing process. Figure 9 shows the evolution of the fracture geometry obtained from the analysis of 3D X-ray tomography images. Before water saturation (just after hydrostatic loading), the fracture volume was equal to 60 mm³. Immediately after water saturation, the fracture volume reduced to 40 mm³ and it did not change until the end of the test, probably due to the plugged capillary as a result of the collapse in the crack due to the rapid swelling of clay minerals.

From these results, it seems obvious that the calcite content has a strong impact on the self-sealing process in argillite.

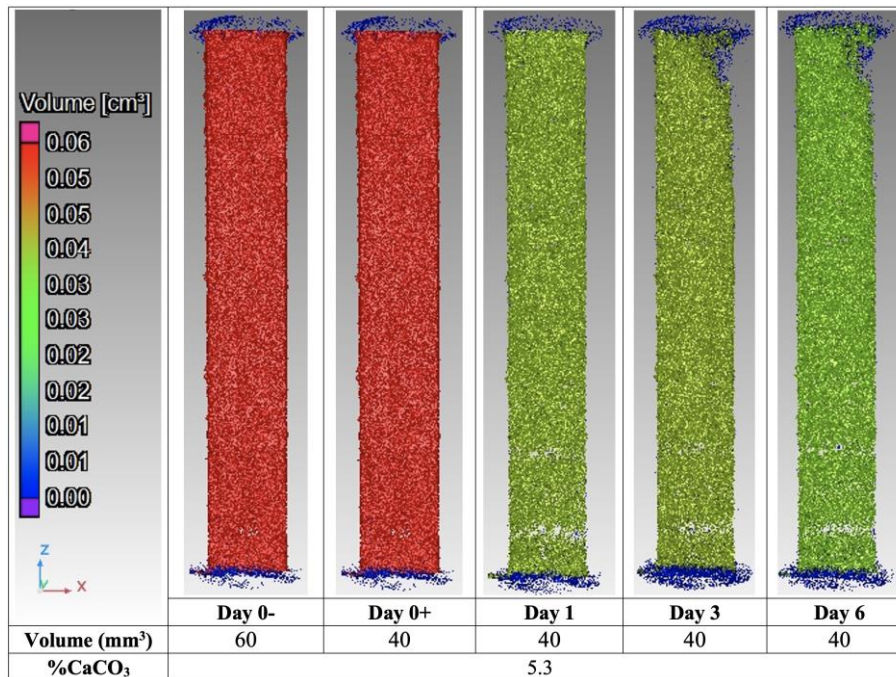


Figure 9 - X-ray 3D tomography images of perpendicular sample EST60018-71 showing the evolution of the crack volume with time (initial crack opening = 0.4 mm) during self-sealing test at 20°C (Day 0-: after hydrostatic loading; Day 0+: after crack saturation).

2.3.1.3 Influence of the crack aperture on the self-sealing process

The influence of the crack opening was studied by performing self-sealing tests on clayey samples with the same low carbonate content (~ 20%), parallel orientation, but with different crack widths. The first one EST60766-3 has an artificial crack opening of 400 µm and a carbonate content of 21%. The second sample EST62690-2 has a crack opening of 800 µm and a carbonate content of 20.6%. The evolution of the water permeability and the crack volumes of these two samples are represented in Figs. 10, 11 and 12.

It is noticed that the smaller the initial crack opening is, the faster the water permeability decreases. Indeed, the permeability of sample EST60766-3 with an initial crack opening of 0.4 mm decreased from 10^{-17} to 10^{-18} m² in 20 days, while the permeability of sample EST62690-2 with an initial crack opening of 0.8 mm decreased from 10^{-15} to less than 10^{-18} m² in 41 days. Concerning sample EST62690-2, the permeability data are missing from day 26 to day 40 because of a technical problem. A last permeability measurement was performed on day 41 and the test was stopped. At the end of this experiment, the permeability is even smaller than the permeability of sample EST60766-3. X-ray tomography images show that the smaller the initial crack opening is, the faster the crack closes. Also, at the end of the experiment, the crack is more closed in sample EST60766-3 with an initial crack opening of 0.4 mm than in sample EST62690-2 with an initial crack opening of 0.8 mm. These results seem obvious because it takes longer to fill a larger volume. However, it is worth emphasizing that the self-sealing mechanism is still efficient even for a wide fracture (although it takes a little longer), especially for these two samples that have a low carbonate content (~ 20%).

Generally, the water permeability decreases rapidly during the first hours of injection followed by a slower decrease. However, the initial permeability of the healthy (i.e., initial) claystone is never

recovered. The final water permeability is around 10^{-18} – 10^{-19} m² and it is higher by almost 2 orders of magnitude compared to the value of the intrinsic permeability of the healthy COx claystone which is estimated between 10^{-21} and 10^{-20} m², depending on the orientation of the sample (Andra 2005; Escoffier 2002; Giot et al. 2011, 2012, 2014; Homand et al. 2004). Concerning the crack volume, the self-sealing process induces a significant reduction but the crack is never completely closed, at least for the duration of our tests.

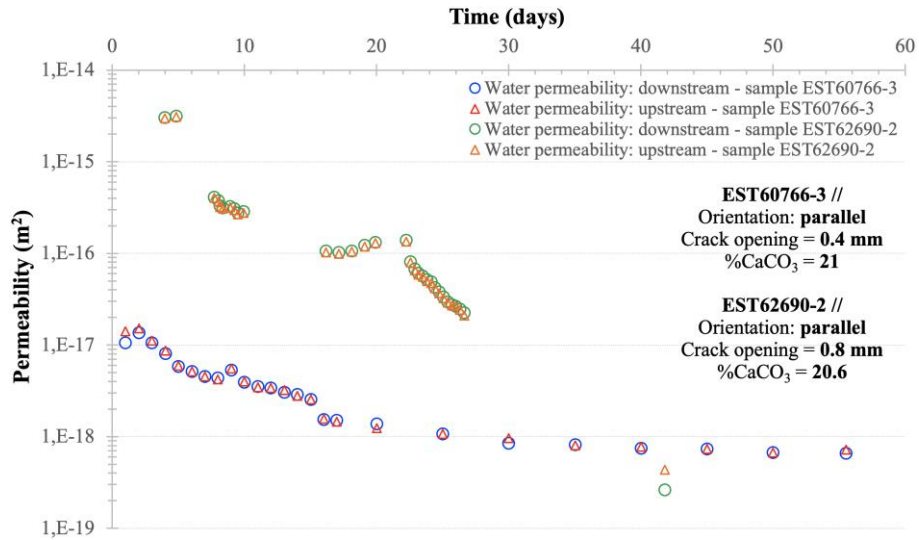


Figure 10 - Evolution of water permeability of parallel sample EST60766-3 and parallel sample EST62690-2 during self-sealing test at 20°C.

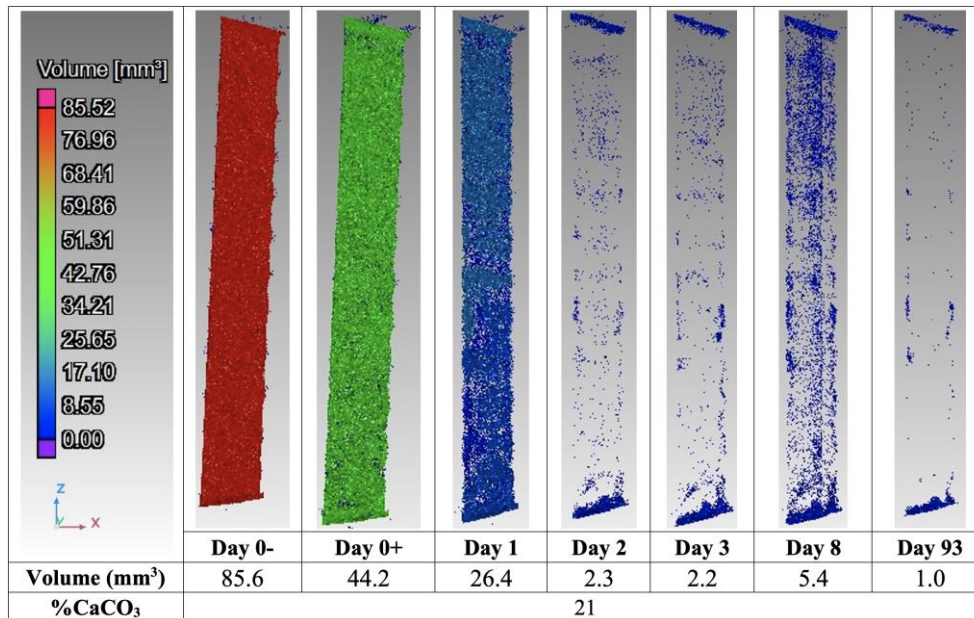


Figure 11 - X-ray 3D tomography images of parallel sample EST60766-3 showing the evolution of the crack volume with time (initial crack opening = 0.4 mm) during self-sealing test at 20°C (Day 0-: after hydrostatic loading; Day 0+: after crack saturation).

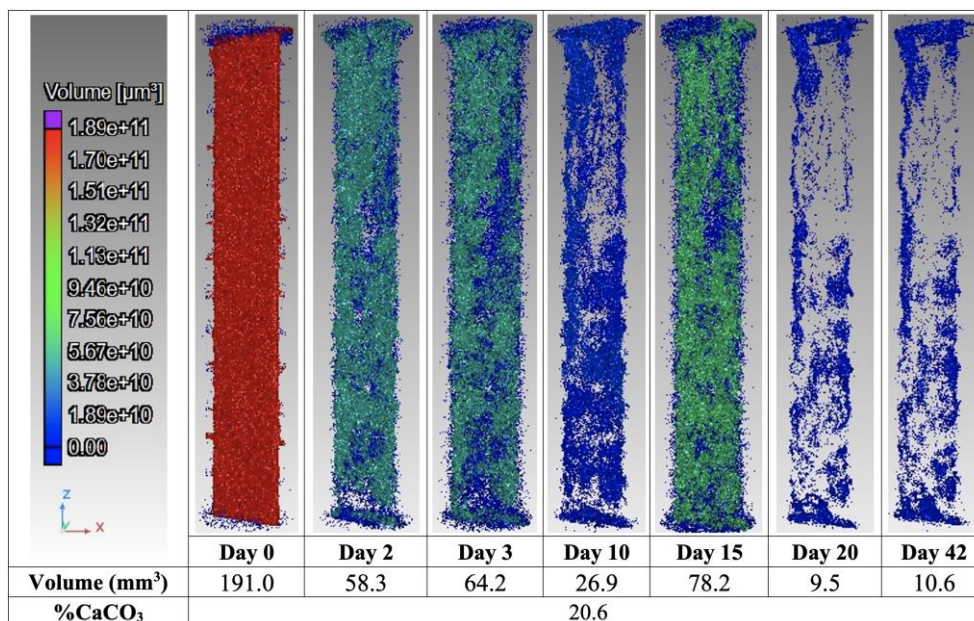


Figure 12 - X-ray 3D tomography images of parallel sample EST62690-2 showing the evolution of the crack volume with time (initial crack opening = 0.8 mm) during self-sealing test at 20°C (Day 0: after hydrostatic loading).

2.3.1.4 Influence of temperature on the self-sealing process

The influence of temperature on the self-sealing process has been studied by performing self-sealing tests on parallel samples at temperatures up to 80 °C following the protocol described previously. The following samples have been tested up to now:

- Parallel sample EST66418-10 with an artificial fracture of 400 µm and a carbonate content of 25.4%, at T = 80 °C
- Parallel sample EST66727-05 with an artificial fracture of 400 µm and a carbonate content of 21.2%, at T = 40 °C
- Parallel sample EST60766-3 with an artificial fracture of 400 µm and a carbonate content of 21%, at T = 20 °C

The evolution of the water permeability during the self-sealing tests performed on parallel sample EST66418-10 at 80 °C and parallel sample EST66727-05 at 40 °C is presented in Fig. 13. Only the upstream curve was represented (the downstream curve is almost the same) and it was compared with the upstream curve of the sample EST60766-3 (also represented in Fig. 10), which is a similar sample but performed at ambient temperature (20 °C). An increase of the water permeability just after the heating at 80 °C is observed for sample EST66418-10, followed by a fast and then moderate decrease of the water permeability. Just after this rapid decrease, the water permeability drop follows then the water permeability drop pattern observed in the other tests at room temperature (e.g., sample EST60766-3). Concerning the sample EST66727-05 performed at 40 °C, the water permeability evolves almost in the same way as for the sample EST60766-3 performed at 20 °C. Figure 14 shows the evolution of the fracture geometry obtained from the 3D X-ray tomography data on sample EST66418-10 performed at 80 °C. Before water saturation (just after hydrostatic loading), the fracture volume was equal to 60 mm³. After 37 days of self-sealing experiment, the volume decreased until 10 mm³. Figure 15 shows the evolution of the fracture geometry obtained from the 3D X-ray tomography data on sample EST66727-05 performed at 40 °C. Before water saturation (just after hydrostatic loading), the fracture volume was equal to 69 mm³. Just after crack saturation, it decreased to about 40 mm³. After 35 days of self-sealing experiment, the volume decreased until only 2 mm³.

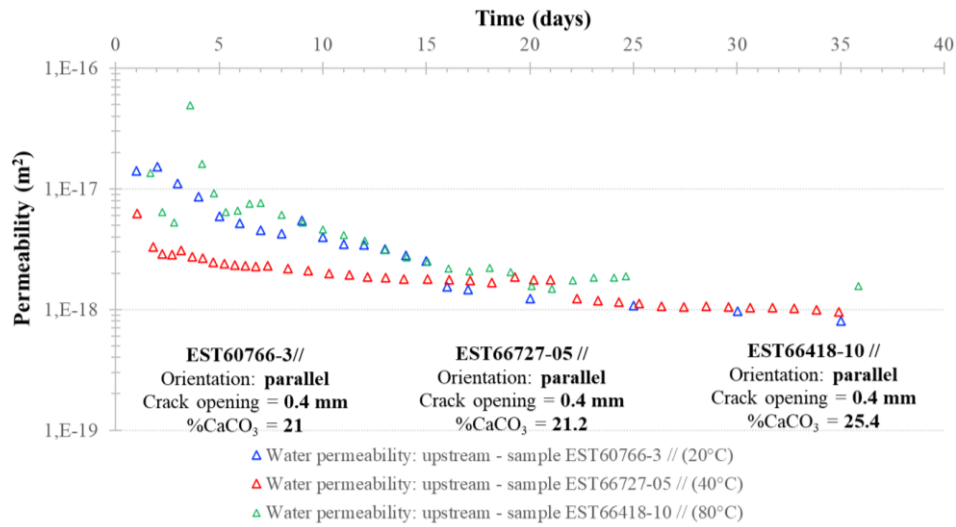


Figure 13 - Evolution of water permeability during self-sealing tests on parallel sample EST66418-10 at 80°C and parallel sample EST66727-05 at 40 °C, compared to parallel sample EST60766-3 at 20°C.

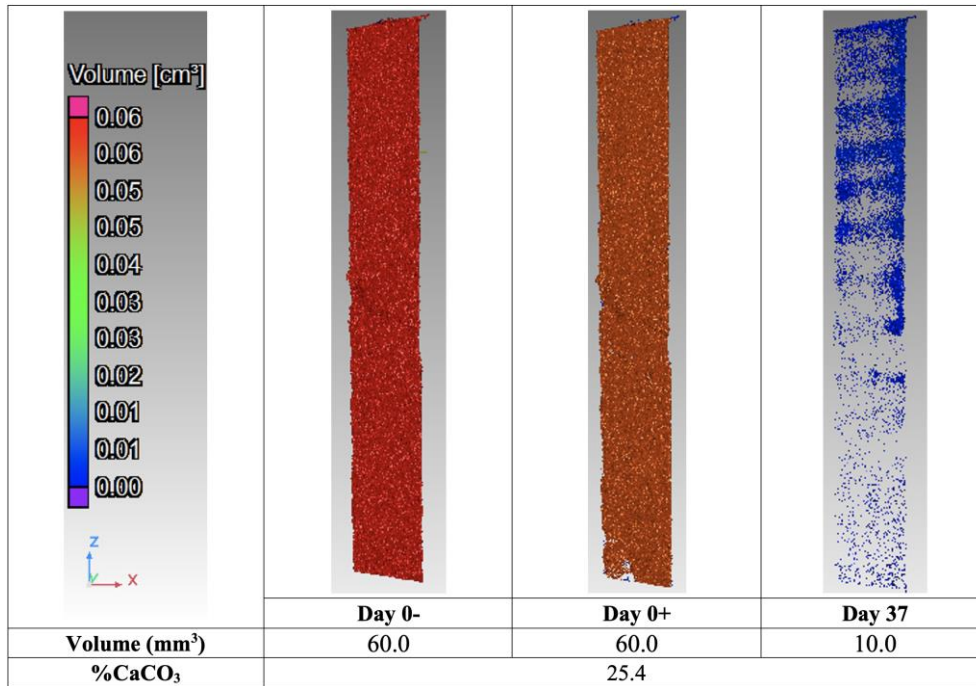


Figure 14 - X-ray 3D tomography images of parallel sample EST66418-10 showing the evolution of the crack volume with time (initial crack opening = 0.4 mm) during a self-sealing test at 80 °C (Day 0-: after hydrostatic loading; Day 0+: after crack saturation).

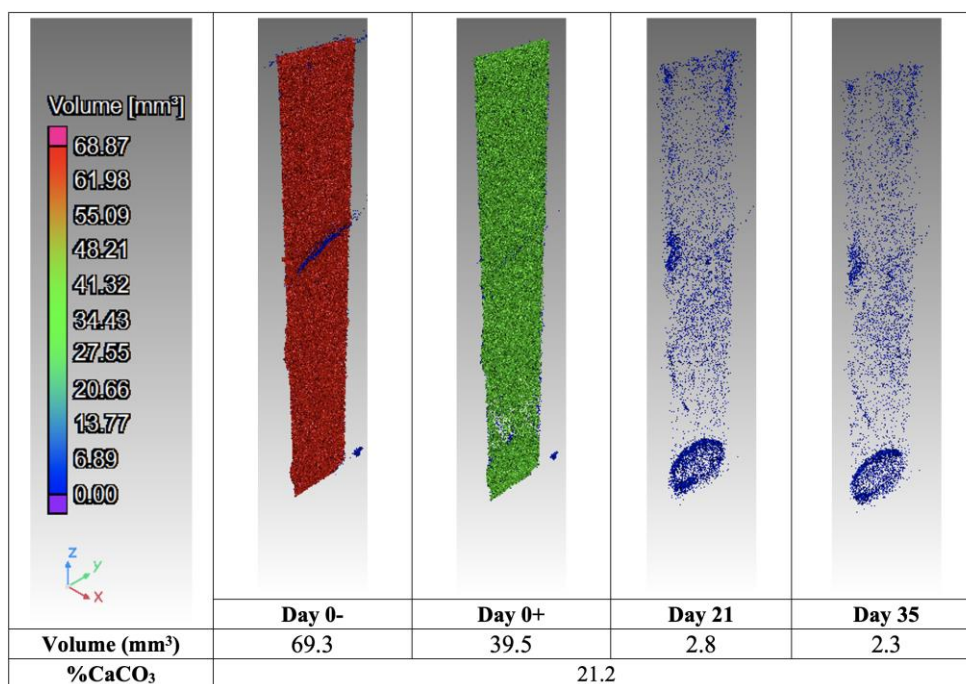


Figure 15 - X-ray 3D tomography images of parallel sample EST66727-05 showing the evolution of the crack volume with time (initial crack opening = 0.4 mm) during a self-sealing test at 40 °C (Day 0-: after hydrostatic loading; Day 0+: after crack saturation).

The influence of temperature on the self-sealing process has also been studied by performing self-sealing tests on perpendicular samples at temperatures up to 80 °C following the protocol described previously. The following samples have been tested up to now:

- Perpendicular sample EST66723-12 with an artificial fracture of 400 µm and a carbonate content of 20.8%, at T = 80 °C
- Perpendicular sample EST66721-17 with an artificial fracture of 400 µm and a carbonate content of 22.3%, at T = 40 °C
- Perpendicular sample EST66721-13 with an artificial fracture of 400 µm and a carbonate content of 22.3%, at T = 20 °C

The evolution of the water permeability during these self-sealing tests is presented in Fig. 16. Only the upstream curve was represented (the downstream curve is almost the same). Unfortunately, it was not always possible to measure the water permeability because of the sealing of the crack and/or the inlet capillaries. An increase of the water permeability just after the heating at 80 °C is observed for sample EST66723-12, followed by a fast and then moderate decrease of the water permeability. Just after this rapid decrease, the water permeability drop follows then the water permeability drop pattern observed in the other tests at room temperature (e.g., sample EST60766-3). Concerning the sample EST66721-17 performed at 40 °C, after the initial significant decrease of permeability, there is no significant decrease during the remaining testing time. Concerning the sample EST66721-13 performed at 20 °C, after the initial significant decrease of permeability, there is no significant evolution of the permeability during the test even though a lot of data are missing. In addition, the permeability the sample EST66721-13 performed at 20 °C is significantly lower than for the other samples tested at 40 °C and 80 °C. Figures 17-19 show the evolution of the fracture geometry obtained from the 3D X-ray tomography data on samples EST66721-13 (80 °C), EST66721-17 (40 °C) and EST66723-12 (20 °C). For sample EST66721-13 performed at 80 °C, self-sealing process was efficient. Indeed, before water saturation (just after hydrostatic loading), the fracture volume was equal to 44 mm³. Just after crack saturation, it decreased to about 19 mm³. After 43 days of self-sealing experiment, the volume decreased until only 9 mm³. For sample EST66721-17 performed at 40 °C, before water saturation (just after hydrostatic loading), the fracture volume was equal to 93 mm³. Just after crack saturation, it decreased to about 47

mm³. After 29 days of self-sealing experiment, the volume barely decreased (until 40 mm³). For sample EST66721-13 performed at 20 °C, self-sealing process was efficient. Indeed, before water saturation (just after hydrostatic loading), the fracture volume was equal to 107 mm³. Just after crack saturation, it decreased to about 55 mm³. After 32 days of self-sealing experiment, the volume decreased until only 7 mm³.

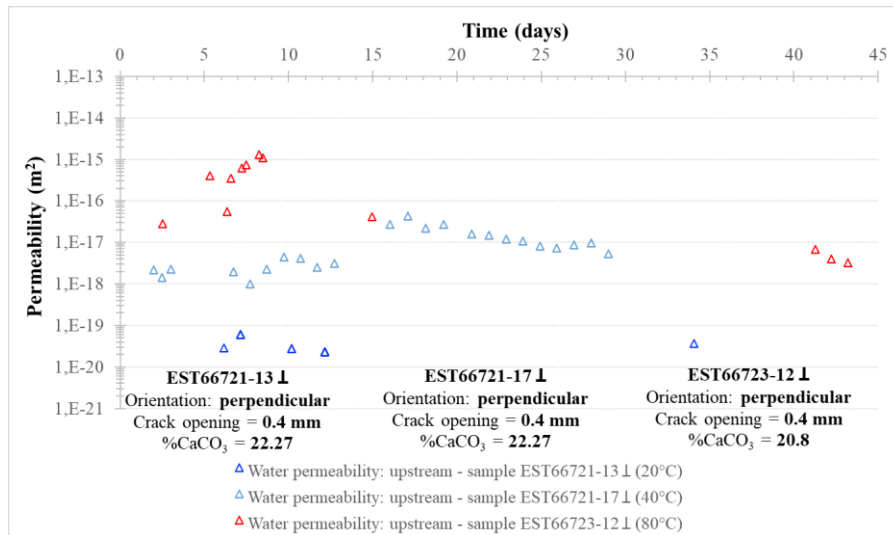


Figure 16 - Evolution of water permeability during self-sealing tests on perpendicular sample EST66723-12 at 80°C and perpendicular sample EST66721-17 at 40 °C, compared to perpendicular sample EST66721-13 at 20°C.

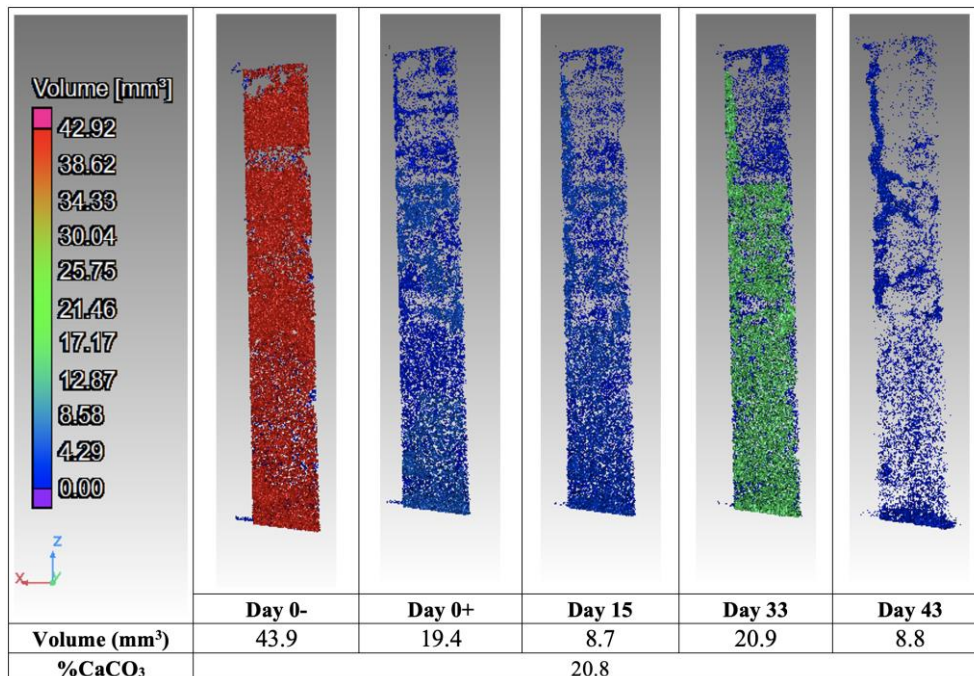


Figure 17 - X-ray 3D tomography images of perpendicular sample EST66723-12 showing the evolution of the crack volume with time (initial crack opening = 0.4 mm) during a self-sealing test at 80 °C (Day 0- : after hydrostatic loading; Day 0+ : after crack saturation).

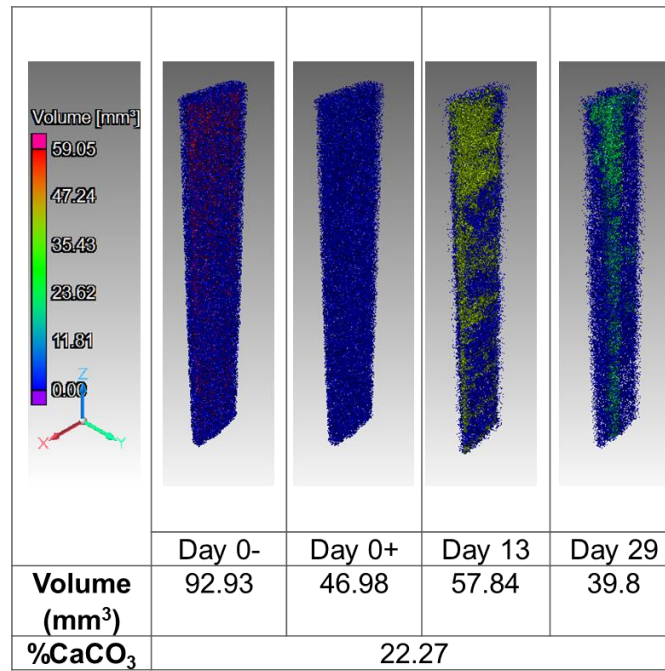


Figure 18 - X-ray 3D tomography images of perpendicular sample EST66721-17 showing the evolution of the crack volume with time (initial crack opening = 0.4 mm) during a self-sealing test at 40 °C (Day 0- : after hydrostatic loading; Day 0+: after crack saturation).

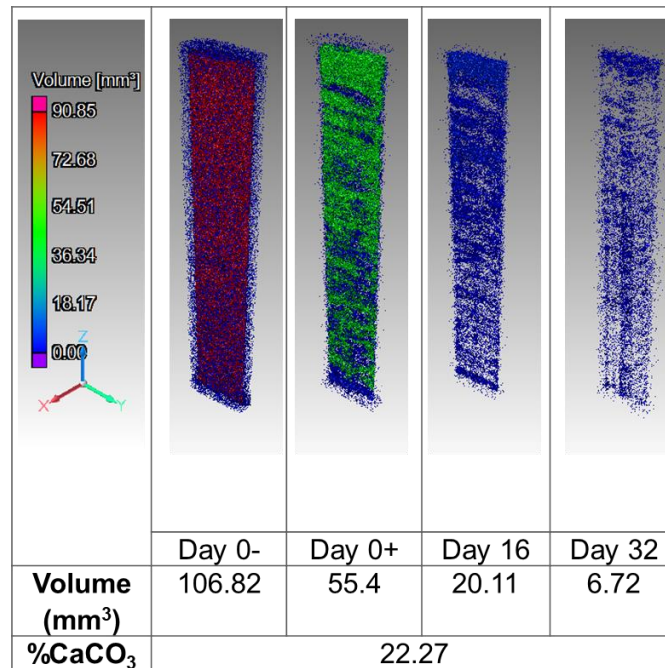


Figure 19 - X-ray 3D tomography images of perpendicular sample EST66721-13 showing the evolution of the crack volume with time (initial crack opening = 0.4 mm) during a self-sealing test at 20 °C (Day 0- : after hydrostatic loading; Day 0+: after crack saturation).

2.3.2 Discussion

2.3.2.1 Influence of the clay content

The results of the different self-sealing tests that were carried out on the COx claystone seem to indicate that several parameters have an influence on the physicochemical self-sealing process (permeability reduction and closure of the initial artificial crack). The first parameter is the calcium carbonate (calcite) content. This parameter is roughly anti-correlated with the clay content. Indeed, the higher the carbonate content, the slower the self-sealing process. And for very high carbonate content, i.e., for very low clay content (sample EST59996-71, Fig. 7), there is almost no self-sealing. These processes are described in Auvray et al. (2015).

This is very well illustrated in Fig. 20 (top), which represents the volume variation percentage of the initial crack (normalized with the volume after hydrostatic loading) obtained from X-ray tomography 3D images during all self-sealing tests with water, for parallel and perpendicular orientations. Only the most clayey sample EST60018-71 (%CaCO₃ = 5.3) wasn't represented in this Fig. 20 because the very rapid sealing induced the plugging of the inlet capillary (which didn't allow permeability measurements) and stopped the self-sealing process. Actually, whatever the sample orientation (parallel or perpendicular) and the test temperature (which doesn't affect significantly the self-sealing process, as said previously), this trend is verified. The bottom of Figure 20 represents the volume variation percentage of the initial crack at the end of the test (even though the test duration is not the same for all samples) as a function of the calcite content for both orientations. It shows that the self-sealing capacity is strongly correlated to the calcite content. This result is very important because it highlights the importance of the mineralogy (i.e., clay and then carbonates content) of the clay host rock to allow a good sealing of fractures in the EDZ during the resaturation of the underground structures for radioactive waste storage in clayey rocks, which will guarantee the safety of the site.

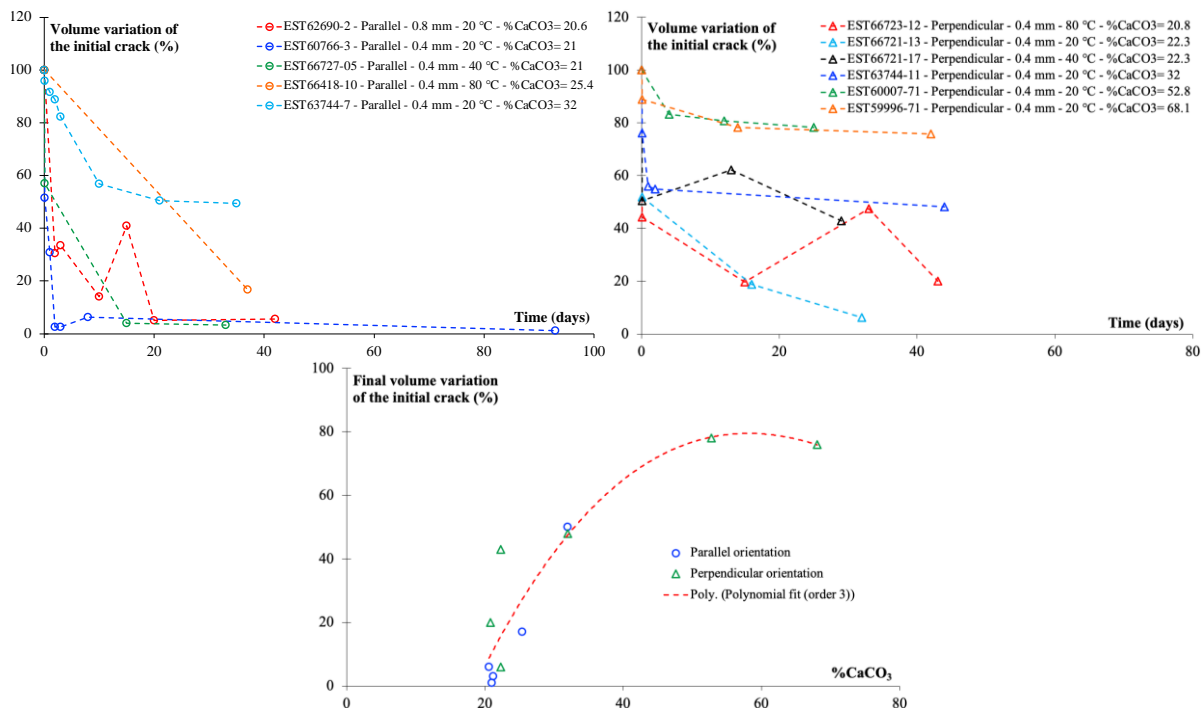


Figure 20 – Top: volume variation percentage of the initial crack (normalized with the volume after hydrostatic loading) obtained from X-ray tomography 3D images during all self-sealing tests with water, for parallel (left) and perpendicular (right) orientations. Bottom: volume variation percentage of the initial crack at the end of the test as a function of the calcite content for both orientations.

Concerning the most carbonated samples EST59996-71 (%CaCO₃ = 68.1) and EST60007-71 (%CaCO₃ = 52.8), the crack volume barely changed during the self-sealing experiments (Figs. 7, 8 and 20) and it was not possible to measure the water permeability because the crack remained completely open, which prevented obtaining a stable pressure gradient, which suggests Navier-Stokes (e.g., non-Darcy) flow. Concerning the samples with low carbonate contents, whatever the initial crack aperture, orientation and temperature, it was possible to measure the water permeability (Figs. 4, 10, 13 and 16) during the self-sealing experiments. These permeability measurements, as well as the analysis of the evolution of cracks volume (Figs. 5, 6, 7, 8, 11, 12, 14, 15, 17, 18 and 19), support the work of Giot et al. (2019) where it is indicated that the threshold regarding the carbonate content to observe self-sealing would be around 40%. Below this threshold, self-sealing process is effective, but almost non-existent when the carbonate content is above. The value of this threshold is consistent with the evolution of the volume variation percentage of the initial crack at the end of the test as a function of the calcite content, which is represented in the Fig. 20 (bottom).

2.3.2.2 Influence of sample orientation and crack aperture

The X-ray tomography 3D images (Figs. 5 and 6) and permeability measurements (Fig. 4) obtained on samples EST63744-11 (perpendicular, %CaCO₃ = 32) and EST63744-7 (parallel, %CaCO₃ = 32) didn't provide evidence for the influence of anisotropy on the self-sealing process. These two core samples were taken from the same borehole EST63744 (same mineralogical and petrophysical parameters, therefore), have the same initial crack opening (400 μm) but are oriented differently, i.e., perpendicularly and in parallel to the bedding plane, respectively. First, the initial mechanical closure due to the initial hydrostatic loading with a confining pressure of 4 MPa induces the closure of the artificial crack, whose theoretical initial volume is equal to 106.5 mm³. This mechanical closure is much more efficient for the parallel sample, probably because of the clay minerals orientation which is parallel to the crack surface (and to the cylindrical sample axis).

Second, concerning the self-sealing process, Auvray et al. (2015) suggested that it is more efficient for parallel orientation than for perpendicular orientation, even though their statement is not obvious considering the experimental curves presented in their paper. Giot et al. (2019) proposed that the first phase of the self-sealing process is due to the crystalline swelling of smectite clay minerals, by adsorption of water in the clay sheets since the samples are partially saturated (actually a little desaturated in our case), before the self-sealing experiment starts (i.e., during the initial crack saturation stage). Then, during the self-sealing experiment, follows an osmotic swelling of the clay minerals, by absorption of water between clay particles at higher water saturation. The third and final phase is the formation of the first clay plugs. Samples oriented in parallel to the bedding plane have water infiltrating more easily between the sheets, and this initiate the self-sealing process more quickly. During these quick phases, there is a rapid decrease in the water permeability and the crack volume. Then, there is a moderate and progressive decrease in water permeability and crack opening due to the progressive swelling of smectite clay minerals in the whole sample from the artificial central crack to the sample borders, and the expansion and densification of clay plugs.

From that, one can suppose for the parallel samples, that clay minerals can swell freely laterally towards the inside of the fracture without any constraint. Contrariwise, when the sample axis is perpendicular to the bedding plane, one can suppose that the axial contraction (due to the 4 MPa confining pressure in our case) prevents a free swelling of the clay minerals surfaces in the axial direction and the swelling in the lateral direction (i.e., perpendicular to the crack surfaces) is probably not that significant. For all self-sealing tests performed with only water injection at room temperature (20 °C), the same evolution of the water permeability and the crack volume was globally observed and the physical mechanisms describes above could explain this evolution. However, the influence of sample orientation is not obvious in our experimental results and it seems that the self-sealing process is equally efficient for both parallel and perpendicular orientations. The (crystalline and osmotic) swelling mechanisms are certainly more efficient in the parallel samples than in the perpendicular samples, but the final phases of plugs

formation, expansion and densification, which are maybe less dependent on the sample orientation, are possibly much more efficient to seal cracks. This could explain why, finally, there is no significant influence of the sample orientation in our self-sealing experiments. Obviously, this conclusion has to be verified with additional self-sealing tests.

The X-ray tomography 3D images (Figs. 11 and 12) and the permeability measurements (Fig. 10) obtained on samples EST60766-3 (parallel, %CaCO₃ = 21, initial crack opening = 0.4 mm) and EST62690-2 (parallel, %CaCO₃ = 20.6, initial crack opening = 0.8 mm) provide evidence for the influence of initial crack opening on the self-sealing process. These experiments showed that the sample with a crack opening of 400 μm self-seals faster than the sample with a larger crack opening (800 μm), which is also illustrated in Fig. 15. But at the end of both experiments, the permeability is almost the same (~10⁻¹⁸ m²). Even though this result has to be verified with additional similar experiments, it is obvious because it takes longer to fill larger volume, while the swelling speed of the swelling clay minerals is probably the same in both cases. As explained by Giot et al. (2019), water must infiltrate the sheets to make them swell. So, when the two crack lips are closer, the crack closes faster and therefore the value of the water permeability and the opening of the crack reduce faster. Moreover, the permeability evolution of sample EST62690-2 with an initial crack opening of 0.8 mm (Fig. 10) has a non-monotonic trend. This means that fracture self-sealing is not a continuous and linear mechanism if the crack opening is wide. Indeed, in that case (wide aperture), some sealing material can be torn off due to the water flow, which can occasionally increase the permeability.

2.3.2.3 Influence of temperature

The self-sealing test performed with water injection at a high temperature (80 °C) on the parallel sample EST66418-10 (%CaCO₃ = 25.4, initial crack opening = 0.4 mm) showed that just after the temperature rise, a rapid increase of the water permeability (Fig. 13). It is worth emphasizing that the water viscosity has been updated to take into account this temperature change (Eq. 1). This rapid increase can be explained by the water overpressure inside the fracture, which spreads the fracture lips and thus increases the water permeability of the fracture. Indeed, the coefficient of thermal expansion of water (2.6×10⁻⁴ (°C)⁻¹ at 25 °C and 5.8×10⁻⁴ (°C)⁻¹ at 80 °C) is an order of magnitude greater than that of solid grains in the COx claystone (2.6×10⁻⁵ (°C)⁻¹ at 25 °C and 11×10⁻⁵ (°C)⁻¹ at 80 °C) (Mohajerani 2011). This pore water overpressure inside the fracture (induced by this differential thermal expansion) dissipates thereafter as soon as drained conditions are restored. Therefore, the rapid increase in fracture permeability is transient. Thereafter, the permeability (Fig. 13) evolution behaves like for the other tests, i.e., decrease first rapidly, then slowly and progressively. The self-sealing test performed with water injection at 40 °C on the parallel sample EST66727-05 (%CaCO₃ = 21.2, initial crack opening = 0.4 mm) didn't show a similar (and transient) rapid increase of the water permeability just after the temperature rise (Fig. 13), maybe because the temperature wasn't that high (only 40 °C) in that case. The permeability evolution behaved like for the other tests, from the beginning till the end, i.e., decrease first rapidly, then slowly and progressively (Fig. 13).

Temperature seems to have a slight delay effect on the self-sealing process since the volume of the crack decreases slower for 80 °C (sample EST66418-10) and 40 °C (sample EST66727-05) than for 20 °C (sample EST60766-3), as illustrated in Fig. 11, 14 and 15. This is also well illustrated in Figs. 20 which shows that crack volume decreases slower for the sample EST66418-10 (80 °C) than for the other samples (EST66727-05 and EST60766-3). However, sample EST66418-10 (80 °C) has a slightly higher calcite content than samples EST66727-05 (40 °C) and sample EST60766-3 (20 °C), so it is difficult to conclude considering the material heterogeneity (variations in the calcite content) and experimental uncertainties (in particular the procedure for calculating the volume of fractures from voxel data). In addition, the permeability decrease with time seems to not be impacted by the temperature, as illustrated in Fig. 13. Obviously, this relative impact of the temperature on the self-sealing process (crack closure and water permeability decrease) has to be confirmed by additional similar experiments at high temperatures, but given the state of knowledge, no significant impact could be identified.

Concerning the perpendicular samples EST66723-12 (80 °C), EST66721-17 (40 °C) and EST66721-13 (20 °C), the sealing of the crack and/or the inlet capillaries didn't allow good measurement of the crack permeability during the self-sealing tests. The higher temperature (80 °C) also induced a rapid increase of the water permeability just after the heating. Therefore, it is difficult to conclude concerning an impact of temperature on the self-sealing process (permeability decrease and crack volume reduction) for the perpendicular orientation.

2.4 Conclusion

In this work, the influence of different parameters on the self-sealing process in the Callovo-Oxfordian claystone was shown. With our X-ray transparent triaxial cell, and our experimental setup, it was possible to follow the evolution of the volume (with X-ray tomography 3D images) and the water permeability of cylindrical core samples of the COx claystone that were initially fractured artificially. Self-sealing tests with water injection were performed under different temperatures, sample orientations, calcite contents and initial crack openings. 3D X-ray scans have been performed on all tested samples before, during and after the experiment and the voxel data were analysed with high-end software for the visualization and analysis of computed tomography (CT) data to estimate the evolution of the crack volume. Also, water permeability was measured continuously during all tests.

It resulted first from our study that the mineralogical composition of the COx claystone influences the self-sealing process. The higher the calcium carbonate content (and therefore the lower the clay content), the less effective the self-sealing process, whatever the sample orientation (parallel or perpendicular). To have an effective sealing, it is necessary to have a carbonate content lower than 40%. Second, the mechanical closure (due to the application of the confining pressure) is much more efficient for the parallel sample because of the clay minerals orientation (bedding plane) which is parallel to the crack surface. The clay sheets oriented in parallel to the initial artificial crack surfaces (lips), and then parallel to the cylindrical core sample axis and water flow direction, favour probably a faster swelling of crack surfaces. However, the influence of sample orientation is not obvious in our experiments and it seems that the self-sealing process is equally efficient for both parallel and perpendicular orientations. Third, the opening of the initial artificial crack influences the kinetic of the self-sealing process. It is faster for an initial crack opening of 400 µm than 800 µm. Finally, considering the material heterogeneity (variations in the calcite content) and experimental uncertainties, temperature doesn't seem to have a significant impact on the self-sealing process (permeability decrease and crack volume reduction). Generally speaking, the self-sealing process is fast at the beginning of the test and then stabilizes after one month. Thanks to the self-sealing process, the permeability of the COx claystone samples is partially restored ($\sim 10^{-18}$ - 10^{-19} m²) compared to the initial permeability of the healthy (i.e., without fracture) claystone ($\sim 10^{-20}$ - 10^{-21} m²). It is all the more promising that the duration of our experiments is much shorter than the in-situ time scale.

In all our experiments, whatever the experimental conditions, self-sealing is always an efficient mechanism if the clay content is high enough. These first results are very promising and give confidence to the positive impact of the self-sealing process on the restoration of the initial mechanical and hydraulic (i.e., sealing) properties of the clay host rock. This physico-chemical mechanism will allow a good sealing of fractures in the EDZ during the resaturation of the underground structures for radioactive waste storage in clayey rocks, which will guarantee the safety of the site. However, our first results have to be confirmed with additional similar experiments to better analyse the impact of some parameters on the self-sealing process, in particular sample orientation and temperature.

3. CNRS (UGrenoble)

3.1 Introduction

Fractures subject to water circulation in some clayey rocks can fully or partially close, leading to a self-sealing process. The swelling phenomena of the material around the lips of the crack are sensitive to water re-saturation, they could also be sensitive to temperature. The experiments that have been conducted tended to make it possible to characterise both the swelling (volume deformation) of the material in the vicinity of the fault, as well as the evolution of the water content, at different temperature levels and with two orientations of the fault with respect to the bedding of the rock.

3.2 Material and methods

3.2.1 Material and sampling

The material is the Callovo-Oxfordian clay rock, which comes from the clay unit of the Meuse/Haute Marne research underground laboratory (URL) in France. All the samples were cut from the same core EST62674 (calcite content ~ 20%). The initial water content was 6.7%.

3.2.2 Experimental devices and procedures

The tests of fracture sealing have been performed in our in-house cell that has been developed initially for our laboratory x-ray tomograph. The device has been adapted to be used on the D50 beamline from ILL for dual x-ray and neutron tomography and with a temperature control up to 90°C (Figure 1).

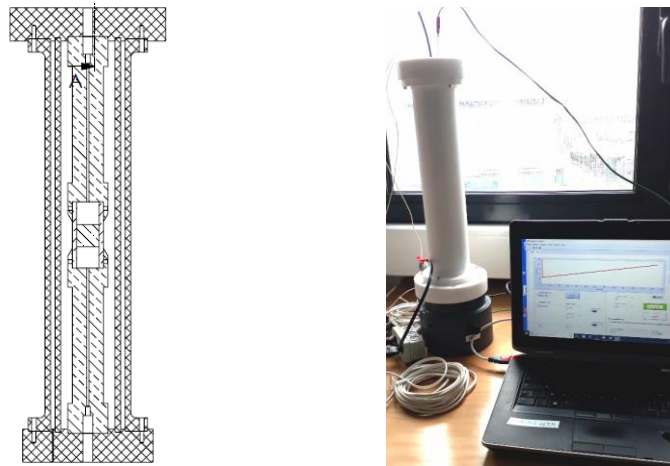


Figure 1 – Scheme and photograph of the cell developed for tests with dual x-ray and neutron CT.

A preliminary analysis was conducted to exploit the data from the bi-modal x-ray and neutron tomography. Radiation absorption depends on both the mass density of the solid phase and the mass density of the aqueous phase (free water and confined water). During a swelling process, these respective densities evolve, leading to an evolution of the absorption levels. In addition, the kinematic field (strain tensor) can be calculated from tomography images (mainly x-ray CT) by a digital image correlation (DIC) method. The link between volume strain and absorption level, subject to a few assumptions, also involves the variation in the saturation level of the rock. This theoretical analysis was compared to previous experimental results and shows a relatively good predictive character (Stavropoulou et al., 2020).

Then, sealing tests at different temperatures have been performed at D50 beamline. Due to reduced time access to the large facility, time duration of each test has been limited to a few hours, allowing characterising the short-term sealing process.

3.2.3 Research plan

Cylindrical specimens (centimetric size) were cut from in-situ collected cores and prepared with a synthetic crack in the middle axial plane. The crack was initially open and the specimen placed in oedometric conditions (no radial displacement of the outer boundary). Neutron and x-ray scans were done during the flow of synthetic host pore water (site salinity) through the crack every 15 minutes. Crack closure, local swelling around crack and water re-saturation (water content evolution) were quantified thanks to neutron and x-ray scans and DIC analysis. Tests were performed at three different temperatures to observe an eventual thermal impact on the sealing process. Because sealing can be also affected by material anisotropy, some specimens have been sampled parallel to the bedding, others perpendicular. A total of 6 tests were performed, as described in Table 1.

The synthetic water of Andra, whose chemical composition (given in the Table 1 of paragraph 2.2.1) is close to in-situ porewater at the Andra URL, was used in these experiments.

Table 1 - Experimental program of self-sealing characterization.

Tests	Temperature (°C)	Orientation/bedding
1	25	//
2	60	//
3	90	//
4	25	⊥
5	60	⊥
6	90	⊥

3.3 Results and discussion

X-ray and neutron scans were taken for each of the six tests, with a voxel size of 35 µm for x-ray CT and 70 µm for neutron CT. These images have neither the same spatial resolution (number of voxels), nor the same coordinate system, so they had to be realigned to enable image pairs to be compared. The x-ray images were of good quality, but the neutron tomography images were unexpectedly noisy when water was injected into the crack, most likely due to a diffraction phenomenon induced by the presence of the hydrogen in the water. This loud noise, which could not be corrected during the experimental campaign, severely hampered the possibility of the detailed analysis that was planned. Processing was carried out to extract information from these noisy images, but it was much coarser than originally envisaged. We detail here the procedure followed for two tests, the 90°C test with the bedding parallel to the crack and the 25°C test with the same orientation.

3.3.1 Test 3 at 90°C and parallel to the bedding

The water was injected into the crack after prior heating to 90°C. The scans were taken when the sample was at 90°C (heating prior to placement on the imaging platform), before and after water injection, in order to monitor the sample over time. Figure 2 shows the x-ray scans of a median horizontal section

over time. A gradual reclosure of the interface can be seen during the first three hours, as well as the formation of a few secondary cracks sub-parallel to the interface. The presence of these secondary cracks seems to be partly influenced by the presence of large pyrite inclusions. Figure 3 shows vertical sections of the same sample. The lower part of the sample closes more quickly, probably due to secondary cracks in this zone, unlike the upper part. The total volume of the interface disappeared around three hours (Figure 4a). At the end of almost 7 hours of observation, the crack gives the appearance of having closed, with a level of x-ray absorption in the interface that has largely increased, even if it does not reach the level of the intact material (Figure 4b).

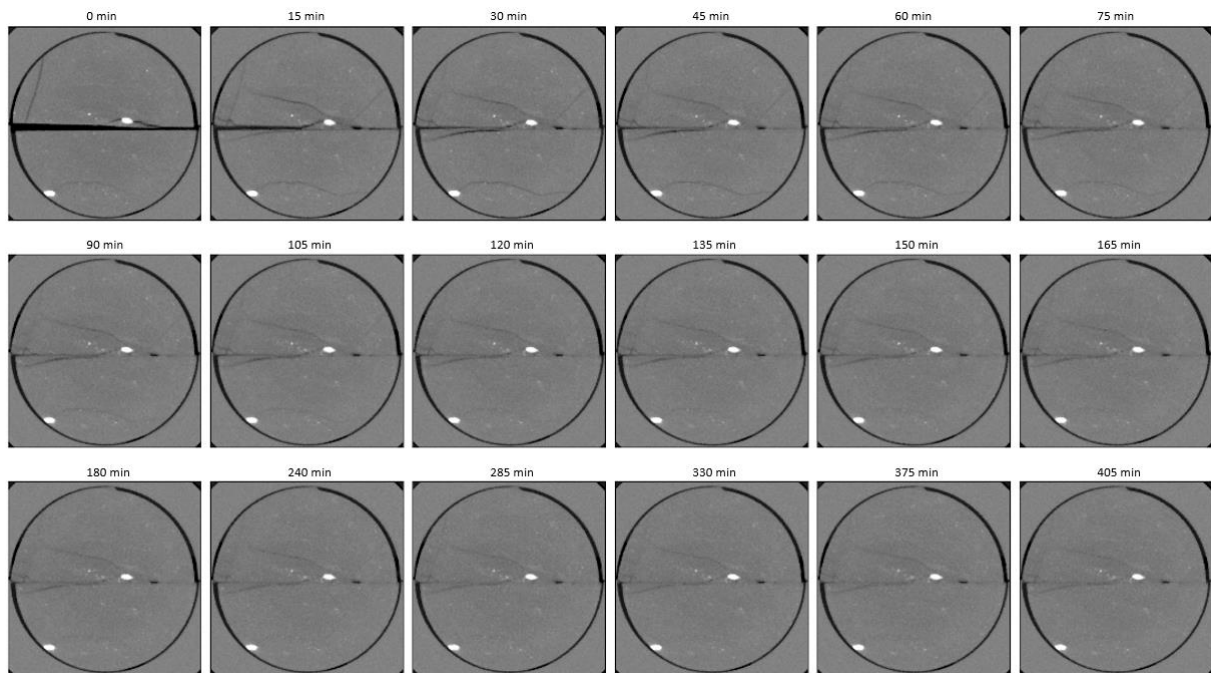


Figure 2 – Test at 90°C, time evolution of a horizontal x-ray tomographic section at mid-height.

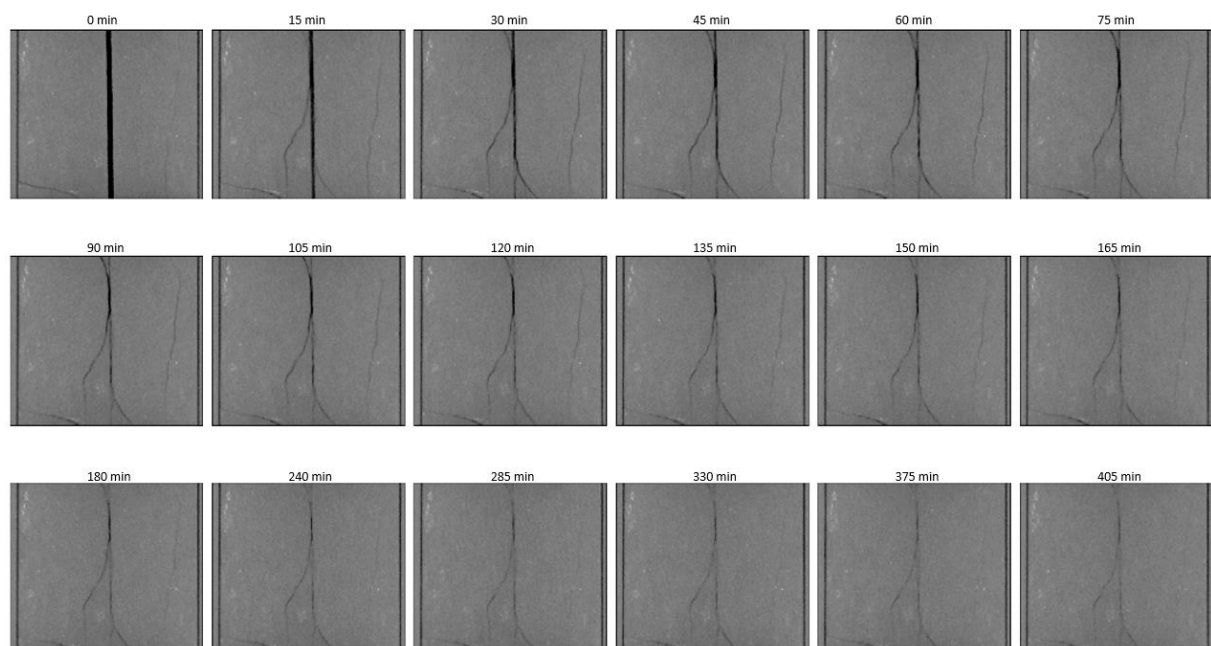


Figure 3 – Test at 90°C, time evolution of a vertical x-ray tomographic section.

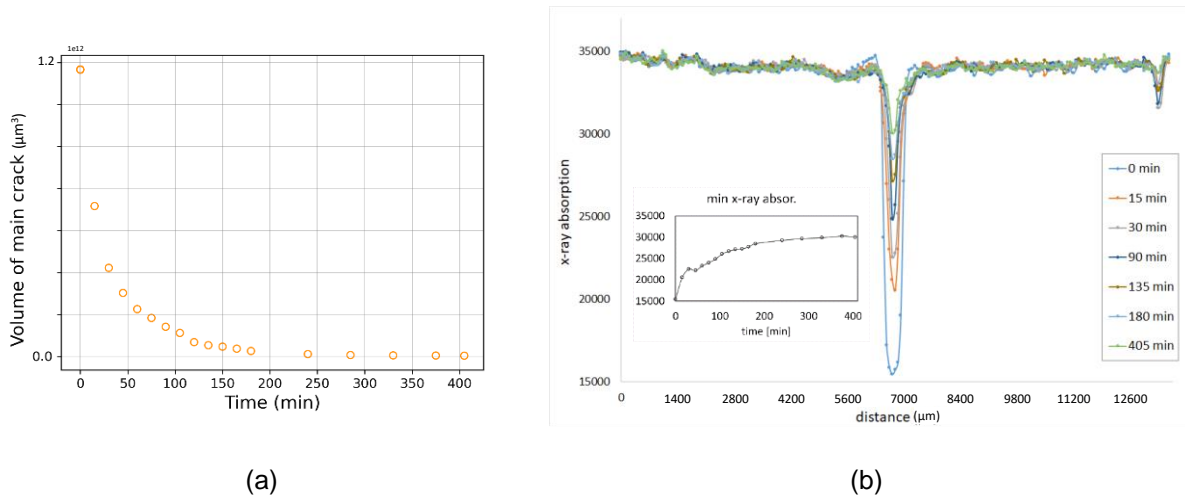


Figure 4 – Test at 90°C, (a) evolution with time of the interface volume ; (b) profiles of x-ray absorption across the interface and (small) evolution with time of the minimum if x-ray absorption in the interface.

Figures 5 and 6 show horizontal and vertical sections of the neutron absorption field. As soon as the water was injected, the absorption increased drastically across the interface, due to the strong absorption by the hydrogen in the water. Figure 7 shows the time evolution of absorption profiles across the interface. As soon as the water was injected, absorption increases in the interface and its immediate environment due to the rapid penetration of the water into the rock. The water penetration zone gradually expands over time to occupy the whole sample. Nevertheless, the central zone (initial position of the interface) remained a zone of higher water content than the rest of the material, which can be interpreted in different, potentially complementary ways: zone of higher porosity, zone of greater resaturation than the rest of the sample.

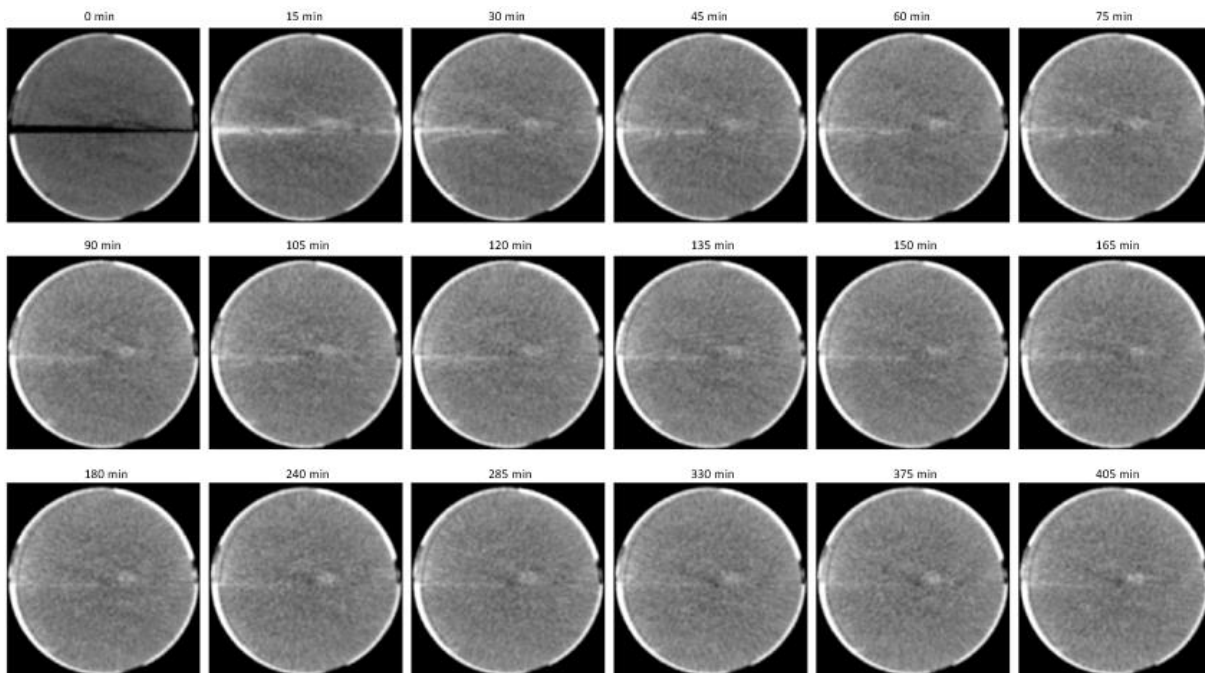


Figure 5 – Test at 90°C, evolution of a horizontal neutron tomographic section at mid-height.

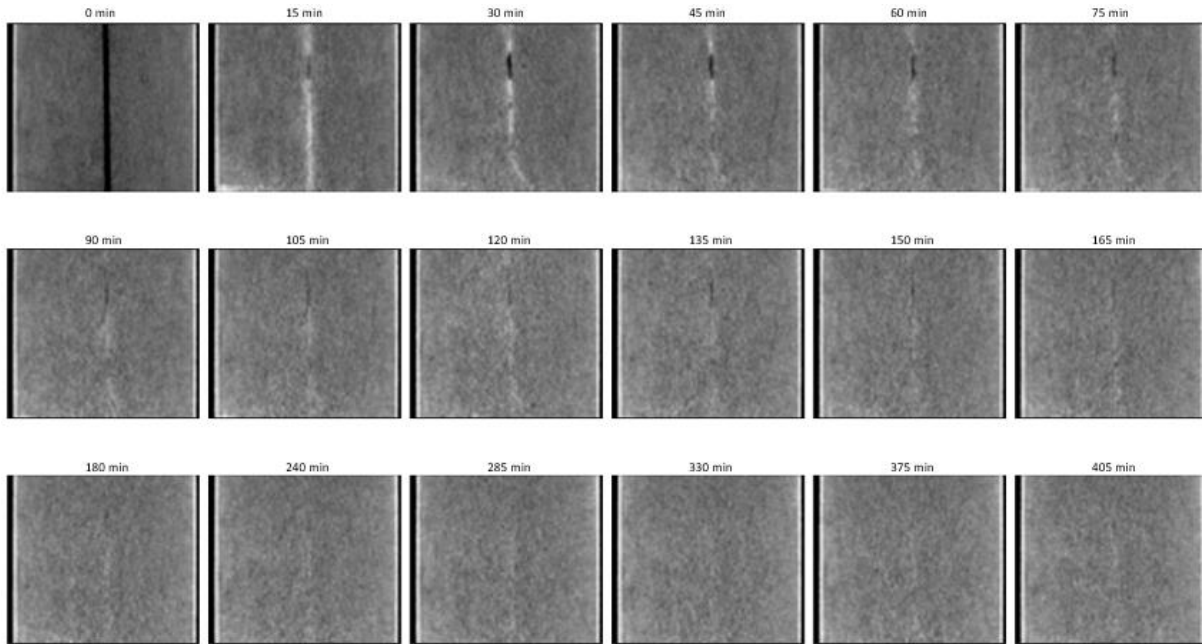


Figure 6 – Test at 90°C, evolution of a vertical neutron tomographic section.

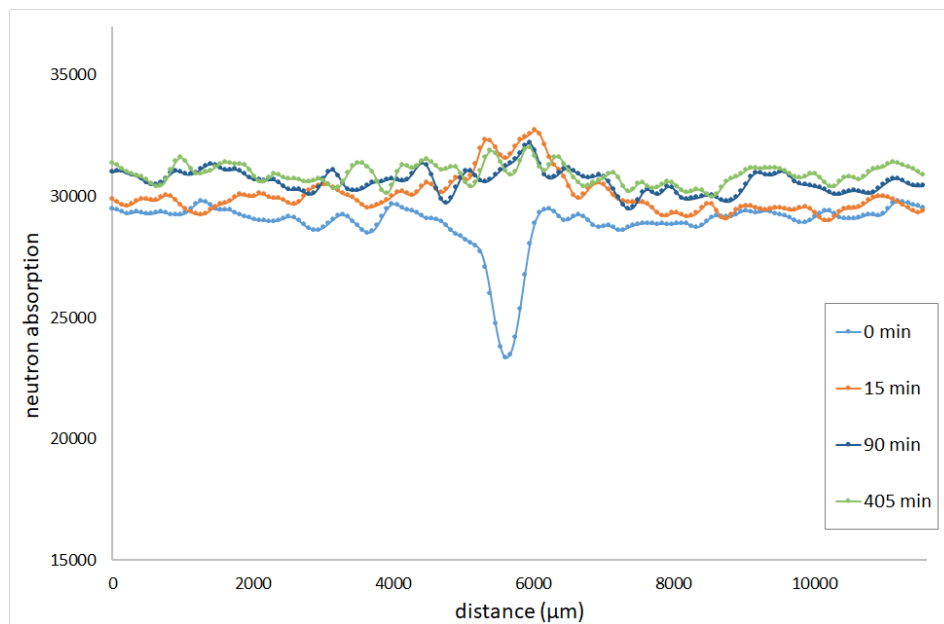


Figure 7 – Test at 90°C, profiles of neutron absorption across the interface.

From the x-ray tomographic images, the kinematic fields were measured using the digital image correlation (DIC) method developed in the code spam (Stamati et al., 2020). The displacement fields between the initial reference image and the various successive images were calculated, followed by the strain fields. Figures 8 and 9 show the projections of the volume deformation field, vertical and horizontal projection, respectively, using an average filter function. Obviously, the measurements are uninterpretable in the area of the initial interface due to the lack of material in the reference image. Outside this central zone, it is possible to observe extended swelling of the material, which increases over time and appears as the main closure mechanism, along with the formation of a few secondary cracks.

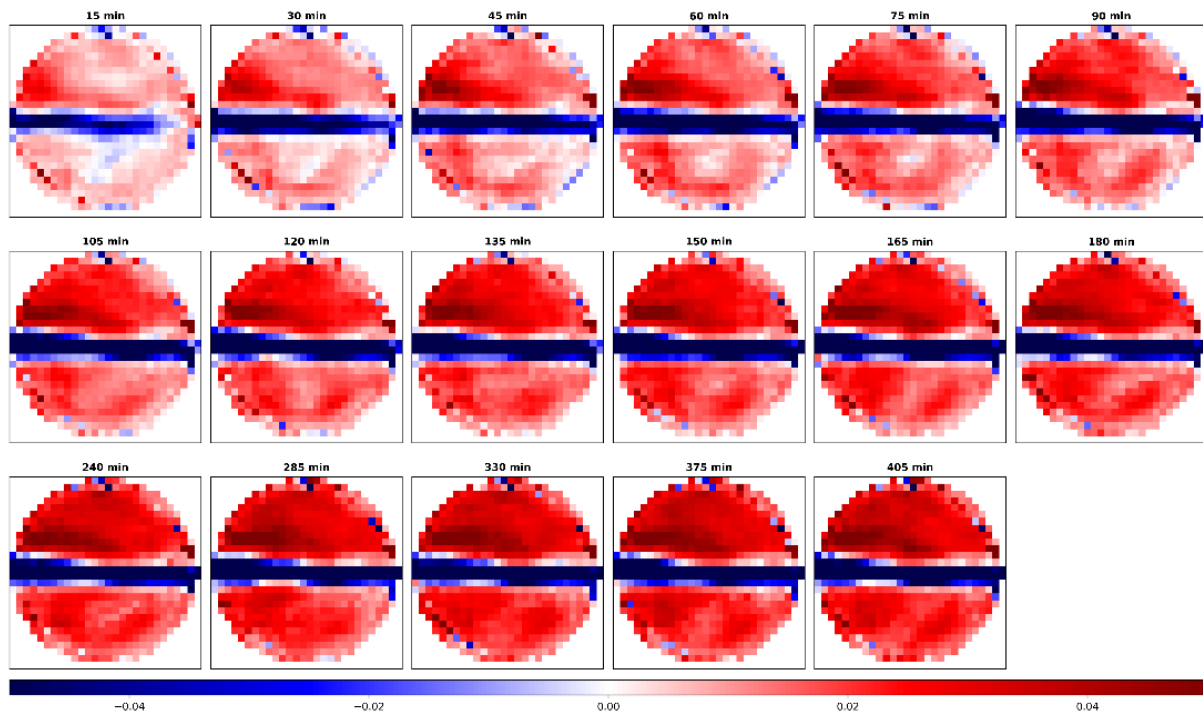


Figure 8 – Test at 90°C, vertical projection (average) of the volume strain field.

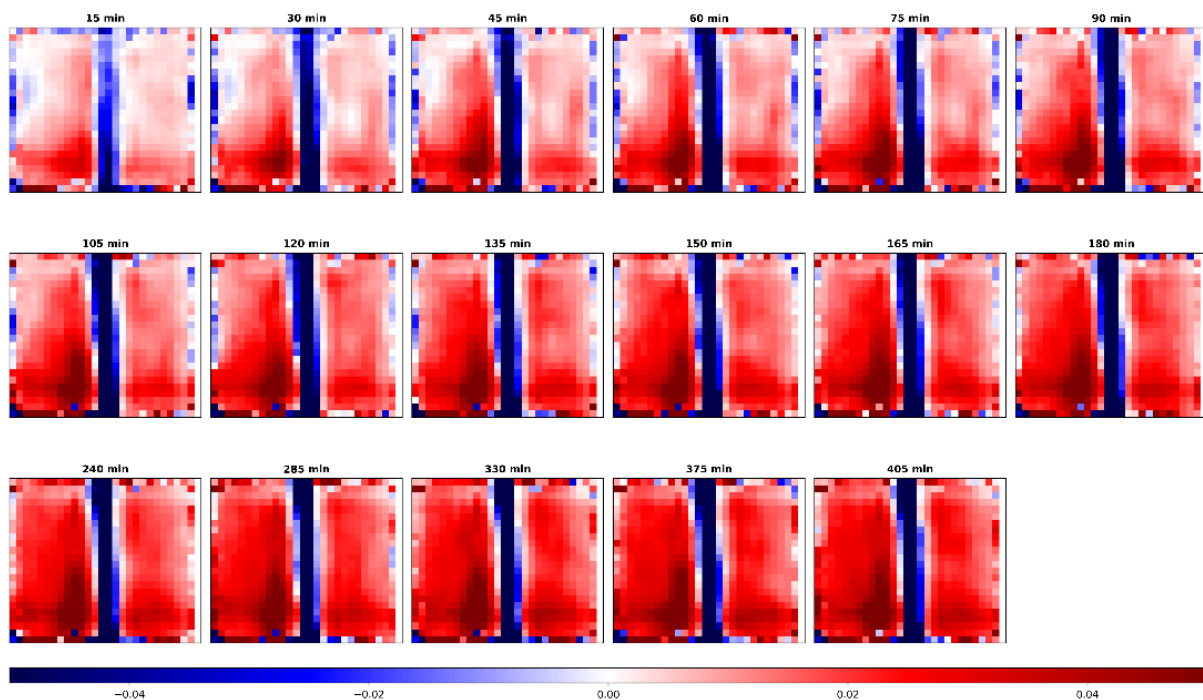


Figure 9 – Test at 90°C, horizontal projection (average) of the volume strain field.

3.3.2 Test 1 at 25°C and parallel to the bedding

Comparative results with those from the 90°C test are shown below. Figures 10 and 11 show the horizontal and vertical sections of the x-ray scans of the fairly rapid closure of the interface by the formation of a zone with a thickness of about twice the initial opening of the interface and where the level of x-ray absorption falls. This zone fills the interface almost instantaneously. This mechanism has

already been observed at room temperature, and is the site of multiple cracks sub-parallel to the bedding, which forms a very damaged material (Di Donna et al., 2022). If we consider the evolution of the overall volume of the interface (Figure 12a), the kinetics of complete reclosure are of the order of 3 hours and the levels of x-ray absorption reached at the end of these three hours (Figure 12b) are comparable to those observed at 90°C.

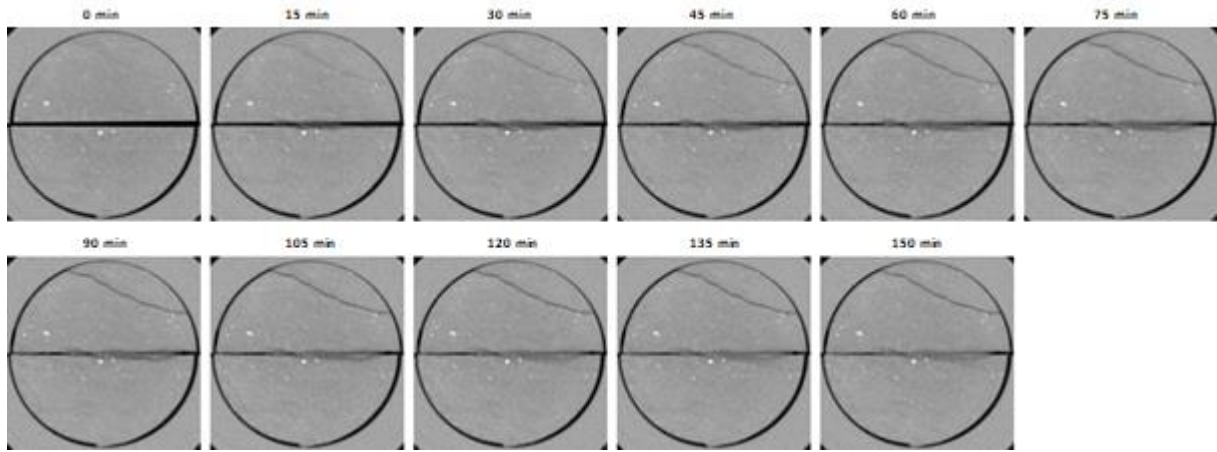


Figure 10 – Test at 25°C, time evolution of a horizontal x-ray tomographic section at mid-height.

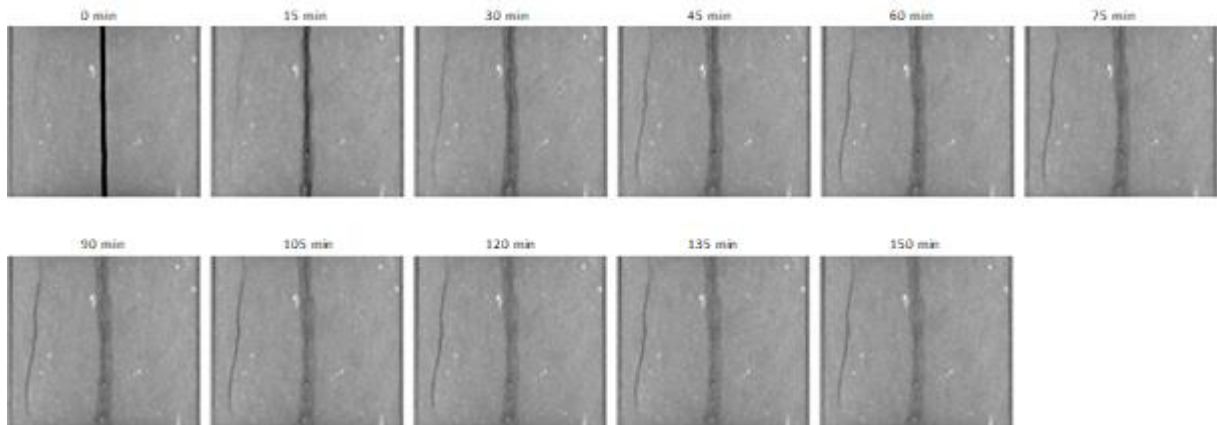


Figure 11 – Test at 25°C, time evolution of a vertical x-ray tomographic section.

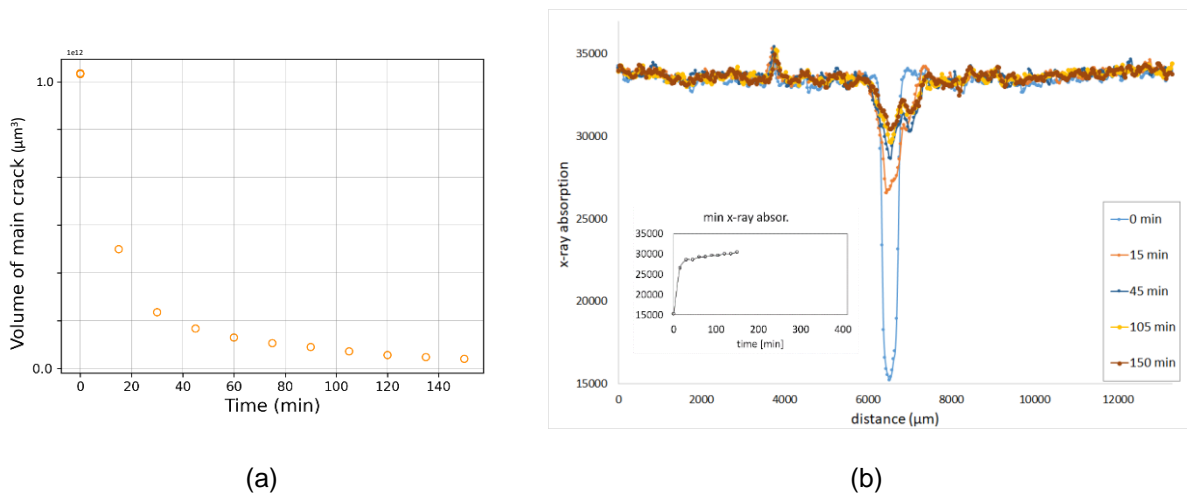


Figure 12 – Test at 25°C, (a) time evolution of the interface volume; (b) profiles of x-ray absorption across the interface and (small) evolution with time of the minimum of x-ray absorption in the interface.

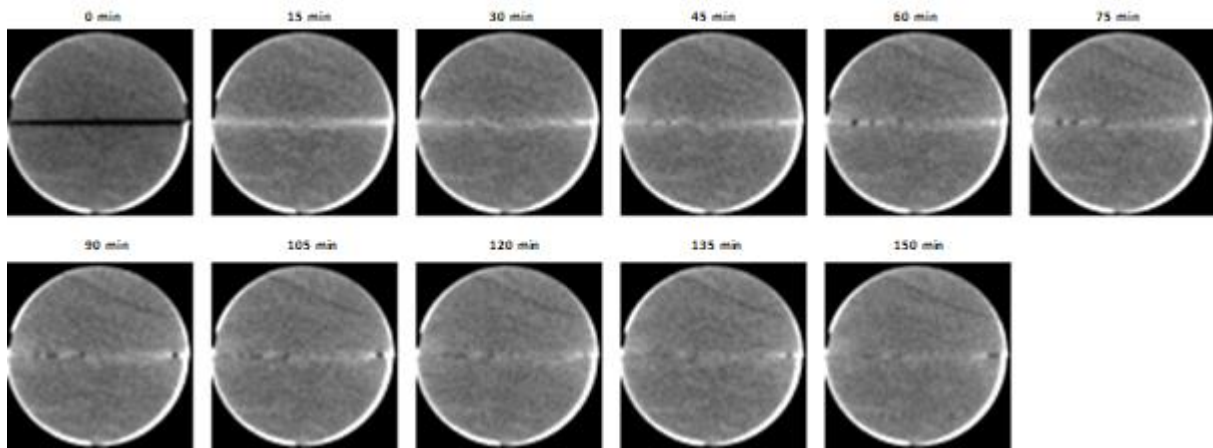


Figure 13 – Test at 25°C, time evolution of a horizontal neutron tomographic section at mid-height.

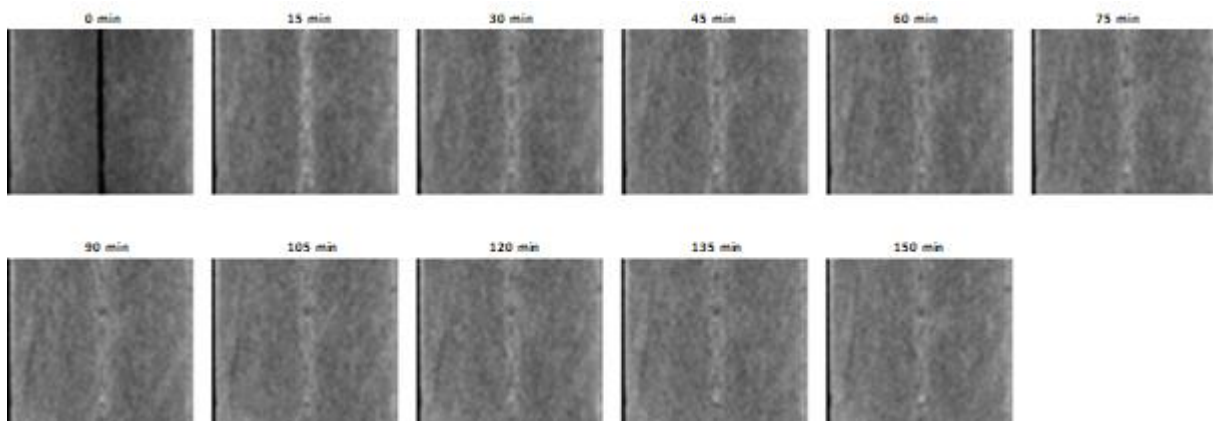


Figure 14 – Test at 25°C, time evolution of a vertical neutron tomographic section.

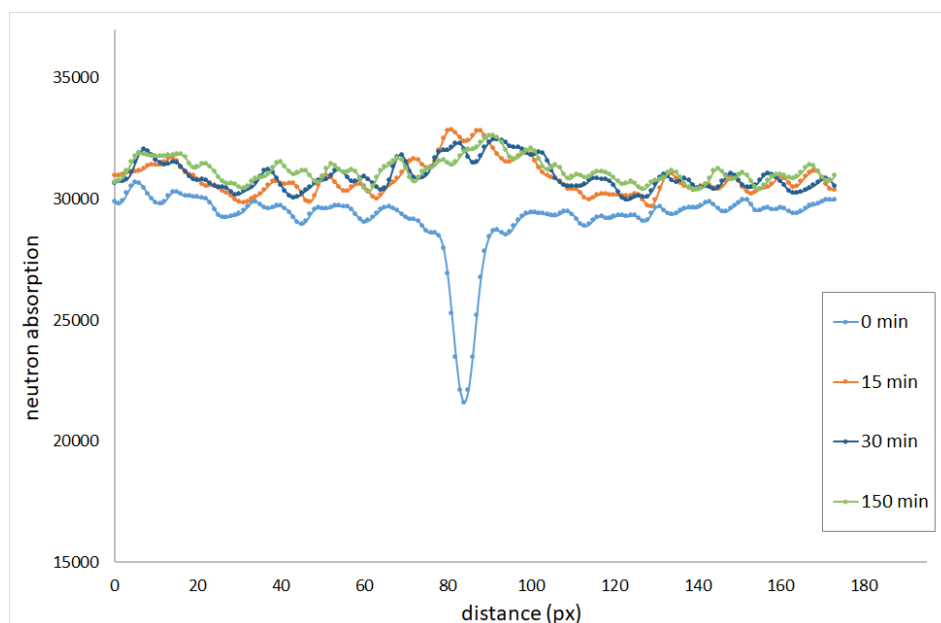


Figure 15 – Test at 25°C, profiles of neutron absorption across the interface.

The neutron tomography images (Figures 13 and 14) show a zone of high water content in the interface. In Figure 15, the zone appears wider and more pronounced than in the 90°C test. This corroborates the x-ray CT observations. The central zone of intense cracking absorbs a large amount of water.

The volume strain fields measured by DIC from the x-ray tomography images indicate the distribution of the swelling zones (Figures 16 and 17). It should be remembered that measuring contraction in the central zone is not viable due to significant reworking in the material in this area which distorts DIC measurement. Outside this central zone, the material swells progressively over time. It can be seen that the overall swelling is largely accommodated by the opening of a secondary crack at the top right of the horizontal section projections. The vertical sections in Figure 16 show greater swelling in the lower zone of the sample, associated with cracks.

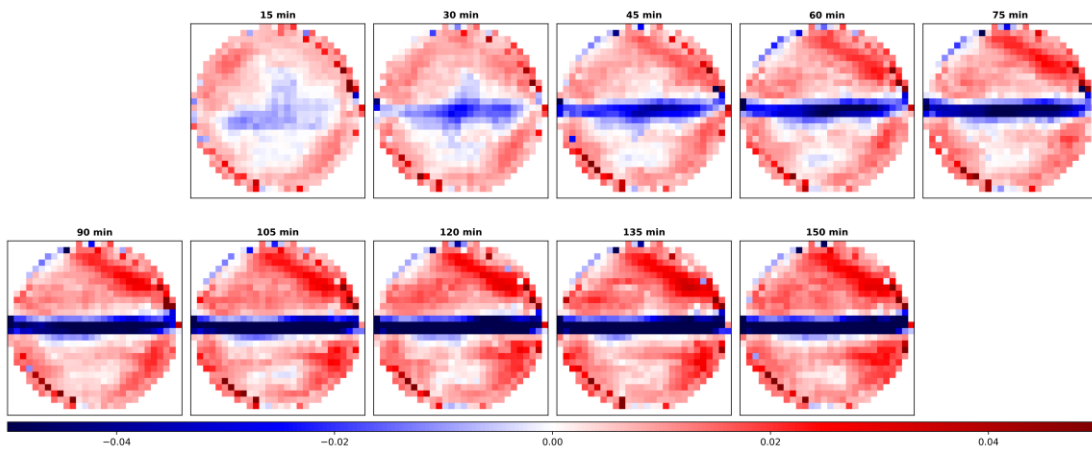


Figure 16 – Test at 25°C, vertical projection (average) of the volume strain field.

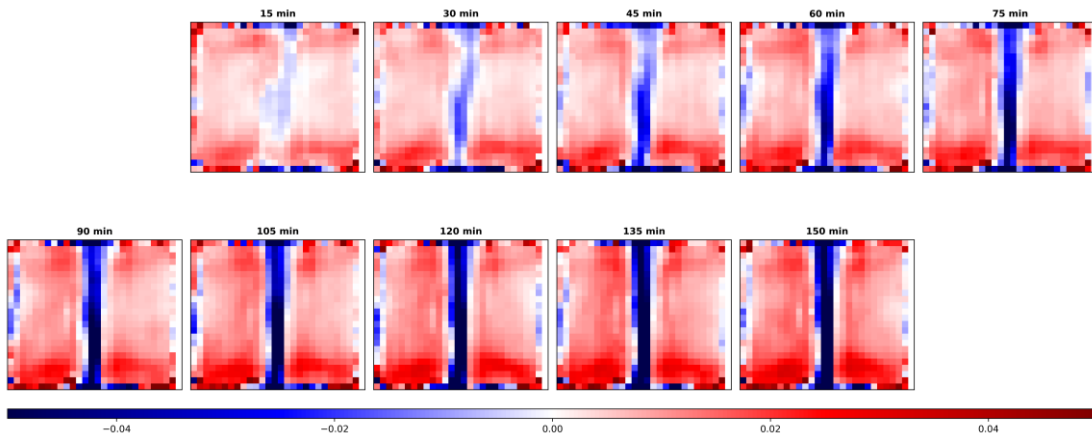


Figure 17 – Test at 25°C, horizontal projection (average) of the volume strain field.

3.4 Conclusion

It should be remembered that we are only considering the reclosure process over a very short period, which cannot predict the phenomena and kinetics over longer periods.

If we compare the phenomena at 90°C and 25°C, the reclosure mechanism is not fully identical. At low temperatures, quasi-instantaneous closure is favoured by the formation of a dense network of micro-

cracks sub-parallel to the bedding in the area close to the interface lips, creating a highly damaged material that fills the interface space. At 90°C, the mechanism is more diffuse and any secondary cracks are scattered. The reclosure kinetics are more gradual and are favoured by a diffuse swelling in the whole sample, much greater in intensity than at 25°C. In both cases, the interface with an initial opening of around 0.3 mm was completely filled within around 3 hours, although the mechanisms were slightly different, showing a more ductile character at 90°C.

A better understanding of the self-sealing mechanism would require the ability to quantify and compare changes in water content and volume deformation. This comparison would provide a better understanding of whether the degree of saturation of the material changes during self-sealing. The quality of the neutron tomographic images needs to be improved, which could not be done in this study due to the very restrictive access conditions to the large facility. Stress conditions should also be introduced to recreate *in situ* conditions and analyse an eventual stress effect. Finally, a measurement of the hydraulic conductivity of the interface during self-sealing would enable the quality of the sealing to be quantified.

4. UKRI-BGS

4.1 Introduction

The evolution of temperature in the EDZ means that at times fractures may form at ambient temperatures or may form at elevated temperatures. Additionally, flow may occur along fractures at times when they are at elevated temperatures or when heat has dissipated to back-ground levels. Therefore, it is important to understand the self-sealing properties of fractures at a range of temperatures from ambient up to 95°C. The higher temperature range is imposed by the safe operational limits of the apparatus used in the current study. To investigate the self-sealing potential of fractures within the EDZ a series of direct shear experiments were conducted by BGS.

The properties of fractures in clay-rich rocks shows that self-sealing and shear can have a marked influence on the hydraulic and gas properties of near-field fractures (EDZ), far-field faults, natural fractures, and joints. Limited experiments have been conducted on transport within fractured rocks of interest. These data suggest that fractures act as foci for flow. Understanding the interaction between resaturation and the mechanical behaviour therefore requires further quantification.

To directly address these issues, BGS performed a series of novel experiments using a highly instrumented (normal stress, shear stress, shear displacement, normal displacement, porewater pressure/flow, temperature, etc) bespoke direct shear apparatus, modified to operate at elevated temperatures; the Heated Shear Rig (HSR). Previous experiments at BGS have looked at fracture transmissivity in Opalinus Clay along an idealised fracture (Cuss *et al.*, 2009; Cuss *et al.*, 2011). A follow-on study investigated hydraulic flow along a realistic fracture (Cuss *et al.*, 2012). This work showed that hydration alone reduced fracture transmissivity by one order of magnitude, while shear displacement reduced it by a second order of magnitude. Continued shear then resulted in increased flow, eventually increasing by five orders of magnitude, three orders of magnitude greater than the starting transmissivity. The injection of fluorescein showed that only around 25% of the fracture surface was conductive. Two later studies on Callovo-Oxfordian claystone (COx) looked at the flow properties of the COx (Cuss *et al.*, 2017) and the interface between COx and concrete (Cuss *et al.*, 2019; 2018). However, none of these studies looked at flow along fractures at elevated temperatures.

The current experimental programme was designed to answer the following research questions:

- What is the mechanical strength of intact rock during direct shear and the variability of this data?
- What influence does temperature have on the mechanical properties of repository rocks?
- What is the topology/texture of the fracture formed and the variability found with repeat testing?
- What influence does temperature have on the surface characteristics of fractures?
- What influence does temperature have on the self-sealing of fractures by water flow?
- What influence does temperature have on the self-sealing of fractures by shear movement?
- What influence does temperature have on the mechanical and textural properties of fractures during re-shear?
- Is there a fundamental difference between fractures formed at ambient temperatures and those formed at elevated temperatures? Is there a difference between the properties seen in different host rocks?

The main expected outcome of this experimental study was to provide detailed process understanding of the evolution of permeability, swelling, and mechanical behaviour of fractured host rock materials under high thermal loads in the near-field.

The study was conducted in Boom Clay, Callovo-Oxfordian claystone, and Opalinus Clay. However, at the time of reporting, only Opalinus Clay had been completed, with some tests in Callovo-Oxfordian claystone.

4.2 Material and methods

4.2.1 Material and sampling

Boom Clay

Cores of Boom Clay were acquired from SCK-CEN (Belgium) from the HADES URL from a depth of 220m.

Callovo-Oxfordian claystone

Upon receipt of preserved T-cell core barrels from Andra, the material was catalogued and stored under refrigerated conditions of 4 °C to minimize biological and chemical degradation. The preserved core barrels consisted of a multi-layered arrangement designed to re-stress the core to *in situ* stress and to environmentally seal it to reduce chemical, biological, and drying effects. Samples were prepared by lathing the core barrels to the test dimensions and the sample ends were made parallel on the lathe. Samples were tested within 12 months of the core being extracted from the Meuse/Haute-Marne URL. Small batches of up to three samples were prepared and temporarily stored in a fridge within vacuum packed plastic bags.

Opalinus Clay

All core material used in the current study came from the shaly facies at the Mont Terri underground research laboratory. Core material derived from boreholes BFI-3 or BGT-1, which were drilled perpendicular to bedding. The latter was drilled for the Gas Transfer (GT) project of the Mont Terri Consortium and was agreed for use in the current study by GT project partners.

Sample Preparation

Callovo-Oxfordian claystone arrived at BGS in a pre-stressed state in a T-cell. The Opalinus Clay samples were taken by BGS or contractors at Mont Terri and were stored in clamped arrangements similar to a T-cell. The Boom Clay samples were stored in vacuum packed foil. Once extracted from the storage arrangement, lengths of approximately 300mm of core were supplied, which were subsampled for testing.



Figure 1 - Callovo-Oxfordian Claystone sample being cut on a lathe during the careful sample preparation process.

During the sub-sampling process a section of core approximately 60 mm in length was cut using a diamond saw. This cut length of core was then trimmed on the lathe (Figure 1) to the sample dimensions of 60 mm in diameter and 53 mm in length; during this process care was taken to ensure the face of the sample was perpendicular to the length of the sample. This process was done as quickly as possible to reduce the time the sample was exposed to the atmosphere and therefore maintain, as much as possible, the in-situ properties of the core. Both the cut sample for testing, as well as the remains of the large core were then wrapped in cling film and vacuum packed for storage.

Testing fluids

All tests were conducted with helium as the gas permeant. Given the importance of fluid chemistry on the behaviour of clay-rich materials, it is crucial that transport and mechanical testing is conducted using water in equilibrium with the test material. For the hydraulic stage of the experiment, synthetic pore water was manufactured to ensure the water was chemically balanced with the test samples.

Boom Clay synthetic pore fluid

A detailed analysis of pore fluid data for the Boom Clay formation was conducted by De Craen *et al.* (2004) and a reference pore water composition defined for HADES (Table 1). Synthetic solutions were mixed in batches approximately every 6 months, depending on the amount of testing being conducted. The recipe for making the pore fluid is described in Table 2.

Callovo-Oxfordian claystone synthetic pore fluid

The hydrochemistry of the interstitial fluid was provided by Andra (Table 3). A stock solution was used when mixing all clay pastes.

Opalinus Clay synthetic pore fluid

A detailed analysis of the pore fluid chemistry of the Opalinus Clay was reported by Pearson *et al.* (2003), the so-called Pearson Water. Table shows the recipe of the pore fluids used in the current study.

Table 1 - Reference Boom Clay pore water after De Craen *et al.* (2004).

Ion	mg/l	mmol/l	Ion	mg/l	mmol/l
Ca	2.0	0.05	Al	0.6×10^{-3}	2.4×10^{-5}
Fe	0.2	0.003	Total S	0.77	0.02
Mg	1.6	0.06	Cl -	26	0.7
K	7.2	0.2	SO₄²⁻	2.2	0.02
Si	3.4	0.1	HCO₃⁻	878.9	14.4
Na	359	15.6			

Table 2 - Recipe for making Boom Clay synthetic pore water.

Chemical	mg/l	Chemical	mg/l	Chemical	mg/l
NaHCO ₃	1209	FeSO ₄	0.456	KCl	14.91
Na ₂ SiO ₃	12.2	MgSO ₄	2.046	NaCl	18.35
CaCl ₂	5.55	MgCl ₂	4.094	NaOH	27.44

Table 3 - Recipe for making Callovo-Oxfordian claystone synthetic pore water.

Ion	mg/l	Ion	mg/l	Ion	mg/l
CaSO ₄ ·2H ₂ O	930	NaCl	1724	NaHCO ₃	344
MgCl ₂ ·6H ₂ O	915	SrCl ₂ ·6H ₂ O	53		
KCl	45	Na ₂ SO ₄	1023		

Table 4 - Pore-water chemistry used as test fluid on all samples, from Pearson (2003).

Ion	mg/l	Ion	mg/l
NaCl	7598	CaCl ₂ ·2H ₂ O	816
KCl	231	Na ₂ SO ₄	1420
MgCl ₂ ·6H ₂ O	511	Na ₂ CO ₃	33

4.2.2 Experimental devices and procedures

4.2.2.1 The Heated Shear Rig (HSR)

The experiments were performed using the bespoke Heated Shear Rigs (HSR), a schematic of this is shown in Figure 2. This apparatus was designed to fracture intact, cylindrical cores with the added capability of being able to directly inject water or gas onto the fracture surface to observe the fracture transmissivity over time. The apparatus has been proven in several fracturing studies which have been applied to both radioactive waste disposal research and the field of carbon capture and storage (Cuss *et al.*, 2019; 2018^{1,2}; 2017; 2016; 2015; 2011; Harrington *et al.*, 2017; Wiseall *et al.*, 2018).

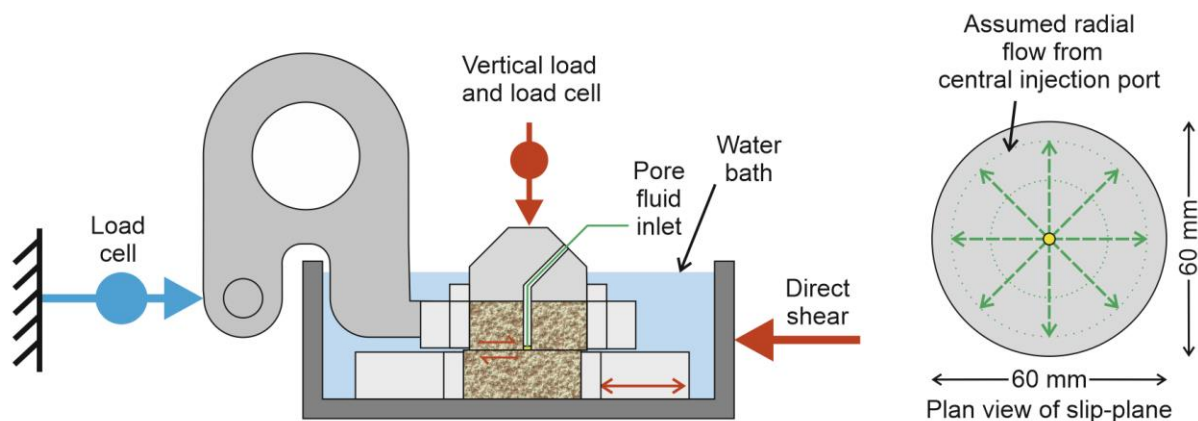


Figure 2 - Schematic of the Heated Shear Rig (HSR).

The custom-made Heated Shear Rig (Figure 2, Figure 3) comprises five main components:

1. Rigid steel frame that had been designed with a bulk modulus of compressibility and shear modulus approximately 2 orders of magnitude greater than the rock tested, resulting in minimal deformation of the apparatus compared to the test sample.
2. Vertical load system comprising an Enerpac hydraulic ram controlled by a Teledyne/ISCO 260D syringe pump, a rigid loading frame and an upper thrust block (up to 72 kN force). Vertical travel of the thrust block was measured by a high precision non-contact capacitance displacement transducer, which had a full range of ± 0.5 mm and an accuracy of 0.06 μm .
3. Shear force actuator comprised of a modified and horizontally mounted Teledyne/ISCO 500D syringe pump designed to drive shear as slow as 14 μm a day at a constant rate (equivalent to 1 mm in 69 days) or as fast as 0.5 mm per second along a low friction bearing. The movement of the bottom-block was measured using a linear variable differential transformer (LVDT), which had a full range of ± 25 mm and an accuracy of 0.5 μm .
4. Pore pressure system comprising a Teledyne/ISCO 500D syringe pump that could deliver water or gas to a pressure of up to 25.8 MPa.
5. A custom designed data acquisition system using National Instruments LabVIEW™ software facilitating the remote monitoring and control of all experimental parameters.
6. A sample assembly comprising two sample holders, where the bottom block was actively sheared, and the top block was connected through a linkage system (“Swan neck”) to a force gauge measuring the shear stress along the slip plane. Vertical load was applied to the rock samples by means of a steel thrust block.

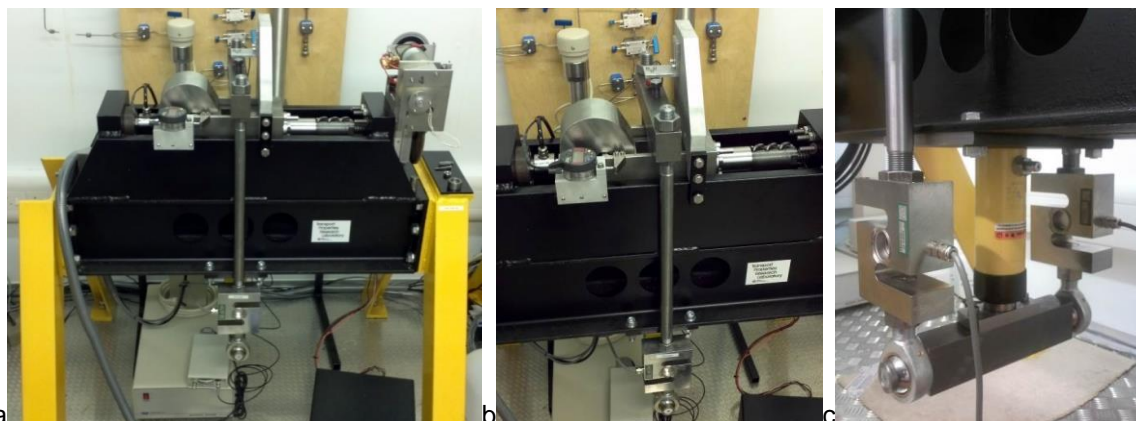




Figure 3 - Components of the Heated Shear Rig. a) Photo of the complete apparatus; b) Loading frame with normal load cells at the bottom; c) normal load ram (yellow); d) sample assembly, shear load cell and horizontal displacement sensor.

Cylindrical samples of 60 ± 0.01 mm diameter and 53 ± 1 mm height (Figure 4) were rigidly housed within two steel collars. The sample was loaded vertically by means of a hydraulic ram, which is actuated using an ISCO/Teledyne 260D syringe pump. The capacity of the pump and ram meant a maximum of 34.7 MPa could be achieved, although in practice vertical stress was lower. Load was measured by two Applied Measurements Limited load cells (DBBW-5T) with an accuracy of ± 0.01 MPa and vertical displacement by a MicroSense 4810/2810 induction sensor with a full range of ± 0.5 mm and an accuracy of ± 0.06 μm . Horizontal stress was created by the Poisson's effect in response to vertical loading in a K_0 geometry. The sample was sheared by means of a second (500D) syringe pump, which had been modified to directly shear the sample along a low-friction track. Shear stress transmitted through the sample/fracture was measured by a 50 kN rated load cell (17.6 MPa) with an accuracy of 0.01 MPa. Horizontal movement of the shear water bath was measured by a linear variable differential transformer (LVDT), which had a full range of ± 25 mm and an accuracy of 0.5 μm . Fluid was injected directly to the fracture through a 4 mm bore drilled to the fracture plane, which had a porous plastic filter at the end. Pore pressure was controlled by a third (500D) syringe pump. For the injection of gas, a 1,000 ml water/gas interface vessel was used. Injection pressure was measured using a Gems 3100 series pressure transducer with a maximum range of 10 MPa and an accuracy of ± 0.025 MPa. All three syringe pumps recorded pressure (± 0.003 MPa), flow rate (± 0.25 $\mu\text{l/h}$), and volume (± 1 μl).

The original Direct Shear Rig (DSR) used square samples, meaning that as a sample sheared, the contact area between the top and bottom sample changed, and as a result normal stress increased if normal load was maintained constant. The use of a cubic arrangement meant that the change in contact area was simple, and experience showed that it was not necessary to correct if strain was limited to a maximum of 0.1 (10 %). Subsequent studies required the apparatus to be modified to accommodate cylindrical samples (Figure 4a). Holders were designed with two semi-circular collars that were bolted together to create a complete circular sample holder (Figure 4b). These were held in blocks that had been machined to hold the circular holders (Figure 4d). These were manufactured to give a close fit, with a grub screw securing the holders. This arrangement meant that samples could be stored between experimental stages and that batch testing could occur as multiple sets of collars were available.

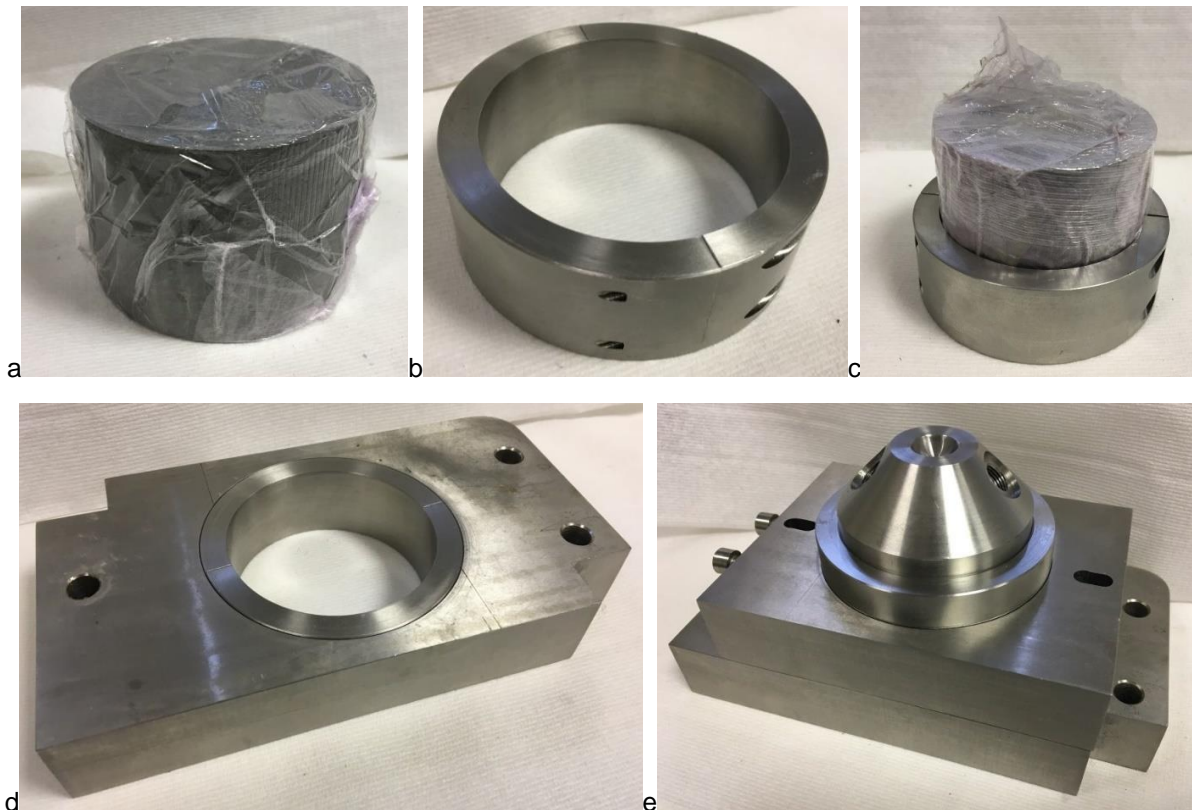


Figure 4 - Sample holder arrangement. a) cylindrical sample of rock; b) sample holder; c) sample holder and sample; d) sample holder and lower block arrangement; e) complete sample holder arrangement.

Figure 5ab Modifications were required in order to add heating to the existing Direct Shear Rig. Several approaches to heating the apparatus were considered, including heating mats, heating cartridges, Peltier devices, and placing the whole apparatus in an oven. It was decided that heating cartridges offered the greatest flexibility and were least likely to be damaged during operation of the experiment. Initially, four heating cartridges were bought from RSPro. These simple devices have no thermal control; therefore a bespoke controller was constructed to facilitate heating control. Four holes were drilled in the shear bath to accommodate the heating cartridges, with one having an additional hole to place the control thermocouple, as shown in. Initial trials of the heater system were problematic, with considerable gradients created within the test sample. The heating cartridges were moved to various available locations within the sample holder, yet the gradient persisted. The data for the least gradient is shown in Figure 6, with a near 50 °C variation in temperature with the heating cartridges set to 90 °C. Therefore, a change in design was required. The addition of a secondary heating system attached to the upper thrust block of the sample arrangement solved the problem. An RSPro band heater was added (Figure 5c), with its own dedicated heat controller. This meant that the temperature recorded by thermocouples in contact with the top and bottom surface of the sample registered temperature within 2-3 °C.

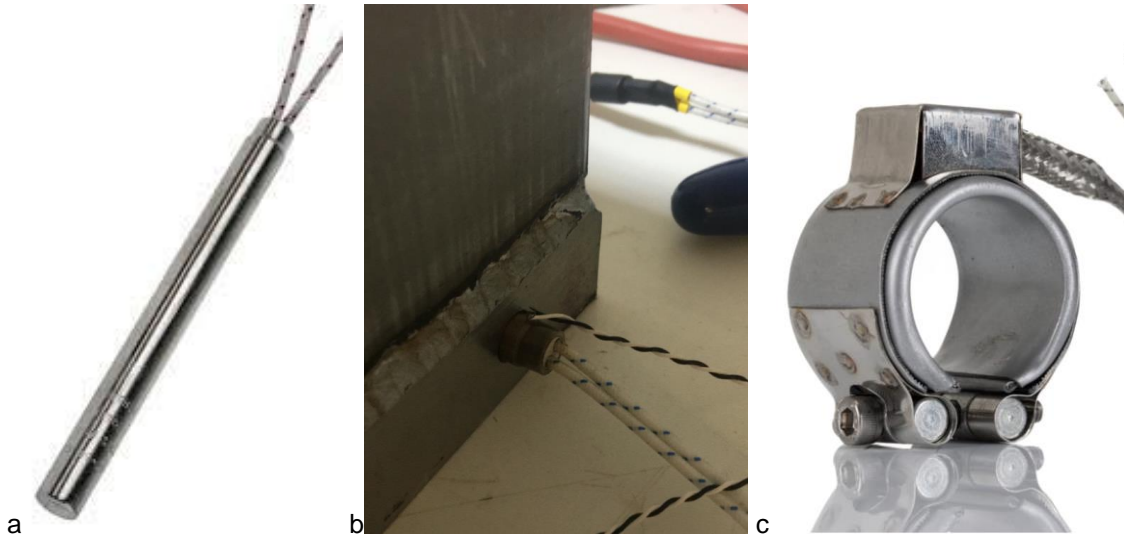


Figure 5 - Components of the heating system of the Heated Shear Rig. a) Heating cartridge; b) Heating cartridge installed into the base of the shear bath; c) Band heater.

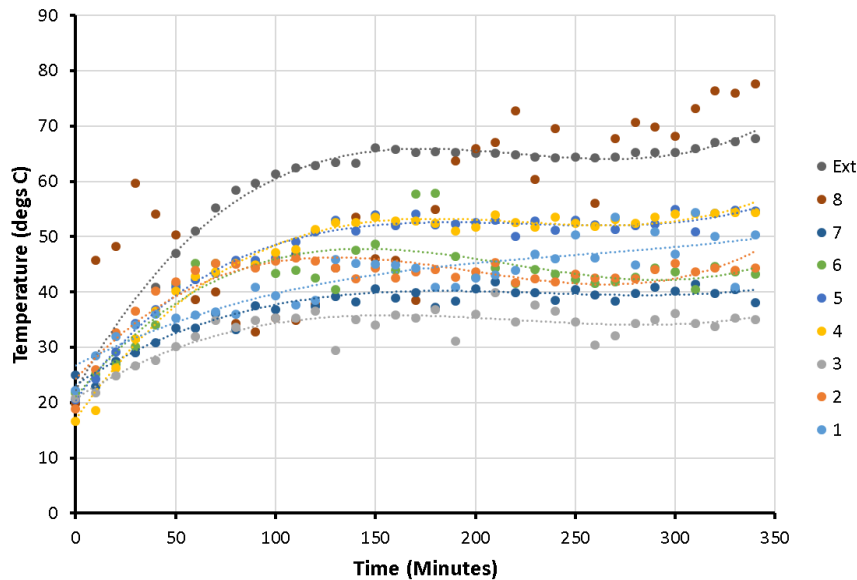


Figure 6 - Temperature distribution measured in the sample assembly when heated by cartridges alone, showing a considerable undesired temperature gradient.

It should be noted that the experimental geometry placed a significant limitation on the temperature of the experiments. The shear box arrangement has an arrangement where the sample assembly sits within a bath which is open to atmosphere. This means that any injected water into the fracture drains into the bath. Assessment for safe operation by the Health & Safety Officer at BGS placed a 95 °C limit on operation so that no chance of boiling water would be encountered. Vented extraction was added to the apparatus to withdraw any steam formed. Several considerations were evaluated on how to raise operational temperature and none of these were felt to be satisfactory. Therefore, an upper temperature limit was placed on experiments. This meant that the planned experimental program would operate between ambient (20 °C) and 90 °C.

4.2.2.2 Testing protocol

Cylindrical samples were prepared by machine lathing with dimensions of 60 ± 0.1 mm diameter and 53 ± 1 mm height. The height of the sample can vary between 52 and 54 mm without affecting the experiment, whereas the diameter of the sample must be as close to 60 mm as possible to fit closely within the steel collars. Tests were conducted using Boom Clay, Callovo-Oxfordian claystone, and Opalinus Clay. Samples were carefully preserved prior to testing to ensure they remained as close to in situ conditions as possible, therefore samples were close to fully saturated at the start of the test. Each test consisted of seven distinct steps as outlined below and summarized in Table 5 and Figure 7:

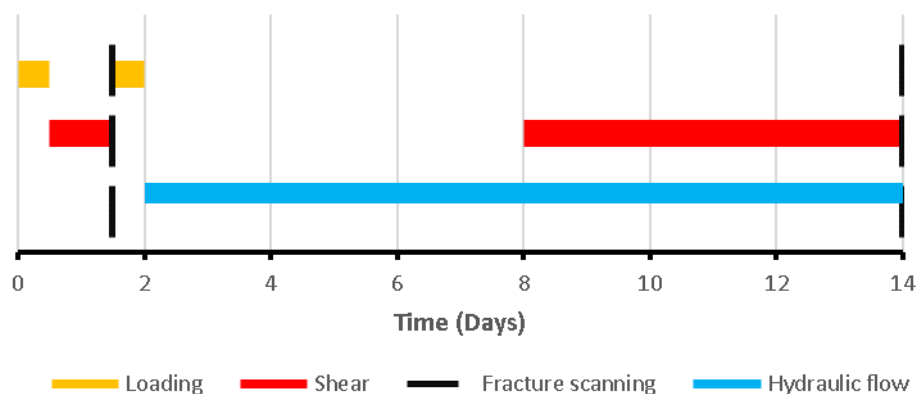


Figure 7 - Graphical summary of the test stages.

Stage 1: Sample loading. Each sample was weighed and measured, and then wrapped in cling film to minimize de-saturation of the sample during testing. Two stainless steel collars were attached, with the sample/collar arrangement loaded into the apparatus. Vertical load was placed upon the sample slowly in steps, taking a few minutes to reach the desired load. Once the sample was fully loaded, the evenness of the load across the load frame was noted and adjusted, if necessary, with the two normal load cells reading the same load within 2 or 3%. Temperature was applied and time allowed for the sample to come up to heat, as measured by two thermocouples on the top and bottom surface of the sample.

Stage 2: Intact Shear. The “intact” sample was sheared to create a fracture at the mid-plane of the sample and to determine baseline mechanical properties. The shear rate was set to achieve 10 % shear strain over a period of 24 hours. This data determined the shear modulus, yield shear stress, peak shear stress, and residual shear stress. In addition, data on dilation/contraction of the sample during shear was recorded.

Stage 3: Fracture Scanning. The heating system was turned off and the normal load on the fracture was removed. The apparatus was taken apart so that the sample could be extracted. Photographs were taken of the fracture during disassembly to note any features of interest and to reorient the samples correctly after scanning had been completed. The two fracture surfaces were scanned using either a NextEngine or a Revopoint Mini laser scanner. The top sample had a 4 mm hole drilled through it using a masonry drill. Care was taken to not heat the drill, which was centrally located by means of a former. The hole was drilled from the fracture face so as not to damage the fracture surface when drilling all the way through the sample. This hole allowed an injection bore to be added. This 4mm diameter pipe had a porous plastic filter at the end and was inserted into the hole to a depth flush with the fracture surface. A small quantity of silicone sealant was smeared on the bore prior to insertion, additional silicone was also smeared on the top-block to seal between this component and the top of the sample. The complete sample assembly was then carefully re-loaded into the apparatus so that re-shearing would occur in the same direction. A small degree of mismatch between the upper and lower fracture faces was likely. However, this was deemed more representative of fractures within the EDZ. Note: Stage 3 lasted less

than one hour and whenever necessary, the sample was stored in sealed plastic boxes to reduce drying effects.

Table 5 - Description of test stages.

Stage	Detail	Duration (days)
Sample loading	Sample weighed and measured, wrapped in cling film, and loaded into two steel rings. Sample loaded into the HSR and normal load increased in a series of steps to target stress. Temperature established and equilibrated.	0.5
Intact shear	Intact sample sheared at constant rate to create a realistic fracture.	1
Fracture scanning	Both fracture surfaces were laser scanned to determine fracture topology. Top fracture had a 4mm hole drilled to allow the addition of an injection bore directly to the fracture plane.	0.1
Sample reloading	Sample re-loaded into the apparatus. Normal load and temperature established.	0.5
Hydraulic flow	Injection of synthetic pore water at a constant pressure of 1 MPa	7
Repeat shear	Sample re-sheared at a constant rate and gas flow monitored	7
Repeat fracture scanning	Both fracture surfaces were laser scanned to determine fracture topology.	0.1

Stage 4: Sample loading 2. Normal load was then re-established, and the heating system was switched on, with temperature allowed to re-equilibrate in the sample.

Stage 5: Hydraulic Flow. Synthetic pore fluid was injected into the fracture to re-saturate the fracture and to encourage self-sealing. Pore pressure was set to 1 MPa with the pump volume determining the flow rate. Initial flow was relatively high as the air-filled asperities meant the system was compressible. However, flow quickly established and was not seen to be high enough (<100 µl/h) to be concerned about erosion of the fracture. Pore fluid was injected for one week, or shorter if flow averaged 0 µl/h for a prolonged period. This stage determined the hydraulic flow properties of the fracture, as well as swelling behaviour.

Stage 6: Flow During Shear. The sample underwent shear for a period of one-week, continuing water injection. This investigated the effect of shearing on water transmissivity. The shear rate was set to achieve ~10 % strain (6 mm). This stage determined the shear modulus, yield shear stress, peak shear stress, and residual shear stress of the fracture on re-shear. In addition, data on dilation/contraction of the sample during shear was recorded. Comparing the water flow rate of Stage 5 with Stage 6 determined the self-sealing capacity of the fracture to shear displacement.

Stage 7: Test decommissioning. The experiment was dismantled, and the fractures was scanned once more to determine whether repeat shearing had created a new failure surface or exploited the existing fracture. This would show whether any self-healing had occurred or whether only self-sealing had been seen. The sample was photographed and stored in sealed boxes that had holes drilled into them so that the sample could be stored in vacuum sealed bags. The use of plastic boxes meant that the vacuum sealing bag did not come in contact with the fracture surface.

All tests were conducted as near-identical as possible to allow comparison.

4.2.2.3 Fracture surface scanner

Understanding the topography of fracture surfaces (fracture roughness) is important in estimating the hydro-mechanical behaviour of discontinuities within a rock mass or along interfaces. Flow properties and mechanical strength will be affected by the spatial distribution of contact areas, which in turn affect the stress distribution and ensuing asperity damage during normal and shear loading.

Fracture surfaces were measured using laser triangulation, whereby the fracture surfaces were scanned to produce a 3D mesh model of the fracture surface. A NextEngine 3D Scanner HD, or latterly a Revopoint MINI 3D Scanner was used (Figure 8). The NextEngine scanner had an accuracy within an error of ± 65 microns, whereas the Revopoint MINI had an accuracy of ± 20 microns. The reason for changing scanners mid-experimental programme was the Revopoint MINI allowed the fractures to be scanned whilst still in the apparatus and did not require for the surface to be oriented vertically for scanning, which resulted in some loss of material. Both scanners output surface data that were processed using TrueMap 5.0 surface topography software. Note: Only the first three tests were scanned using the NextEngine 3D Scanner, with most tests being scanned with the Revopoint MINI.



Figure 8 - Laser scanning of fracture surfaces. a) NextEngine 3D Scanner HD; b) Revopoint MINI 3D Scanner.

4.2.2.4 Fracture Roughness Measurements

Fracture roughness can influence both the mechanical and hydraulic properties of a fracture and therefore influence the overall hydro-mechanical properties of the rock mass. On a fracture surface there may be areas both in contact and not in contact with the opposing fracture wall, this will create a non-uniform stress distribution on the fracture surface. In turn this will influence the formation of asperities on the fracture surface. The degree to which these asperities form can influence the connectivity of flow pathways on the surface, therefore having an effect on the transmissivity of fluids along or across a fracture surface.

In the present study, laser triangulation method was adopted, whereby the fracture surfaces were scanned using either a NextEngine 3D Scanner HD or a RevoPoint MINI 3D scanner. This produced a 3D mesh model of the fracture surface accurate within an error of ± 65 microns. Algorithms inbuilt within the data acquisition ScanStudio HD or RevoScan software produced clean surface data, which were used in subsequent empirical and statistical analysis.

The measured surface data was composed of three components: form, waviness, and roughness. The form corresponds to the underlying shape and tilt of the surfaces with respect to the measuring platform. A “corrected” profile obtained by removing form from the surface data can be used to obtain a 2-D profile

that describes the surface texture. This profile after removal of form is usually referred to as the “primary profile”. The stages are depicted in Figure 9.

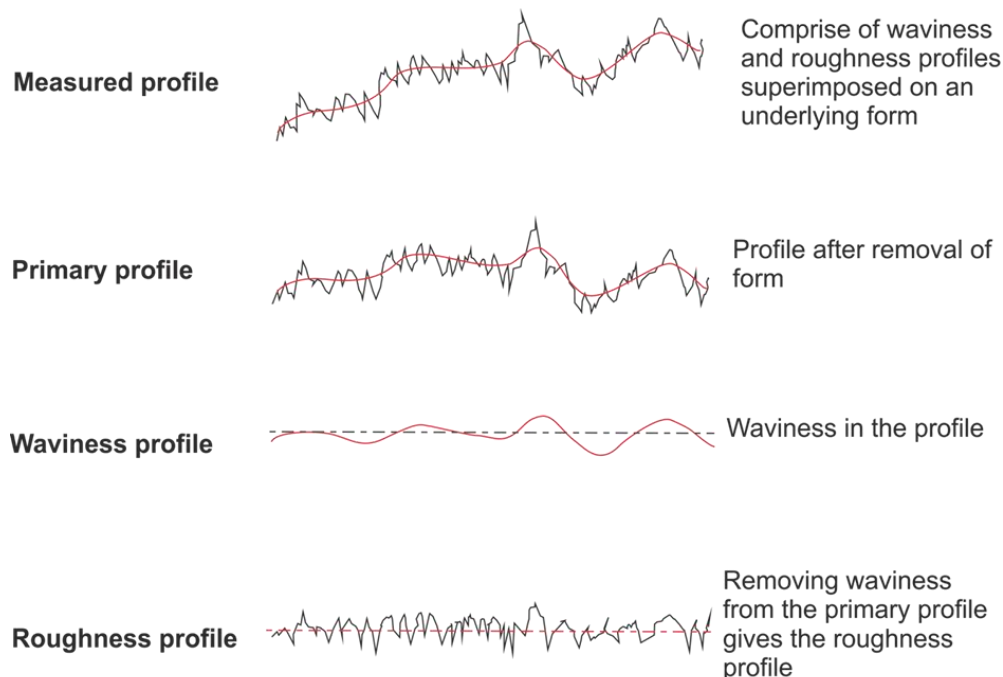


Figure 9 - Summary of stages involved in analysis of measured profile to obtain a roughness profile (From ASTM standard, 2009).

From the primary profile, the waviness profile is removed by applying a band-pass filter. In theory, difference between the primary and waviness profile gives the roughness profile. However, in the present study no band-pass filters were applied due to lack of uniform waviness in the dataset. Hence, surface roughness calculations were performed on “primary profile” datasets spanning the entire fracture surface. All the data processing and surface parameter calculations were performed in TrueMap 5.0 surface topography software. This software package was able to calculate surface or profile parameters using SI methods. Table lists the common parameters calculated for describing the fracture surfaces.

Table 6 - List of parameters calculated to describe surface characteristics of a test fracture.

Parameter	Symbol	Description
Roughness average	$R_a ; S_a$	Arithmetic mean of the absolute distances of the surface points from the mean plane/profile
Root Mean Square (RMS) Roughness	$R_q ; S_q$	Square root of average squared absolute height values of the surface profile from the mean line
Peak Height	$R_p ; S_p$	Maximum height above the mean line/plane
Valley Depth	$R_v ; S_v$	Maximum depth below the mean line/plane

Peak to Valley Height	$R_t; S_t$	Maximum peak to valley distance
Kurtosis	$R_{ku}; S_{ku}$	Measure of the sharpness of the surface/profile
Skewness	$R_{sk}; S_{sk}$	Measures the symmetry of the variation of a profile/surface about its mean line/plane
Texture Direction	S_{td}	Direction of the texture of a surface with respect to the y axis
Texture Index	S_{tdi}	Measure of how dominant the predominant direction is relative to the rest of the surface

4.2.2.5 Calculation of fracture transmissivity

Fracture transmissivity was calculated assuming radial flow from the injection hole given the steady state fluid flow rate Q and the pressure head H at the injection point. Steady flow in a cylindrical geometry can be given by:

$$Q = \frac{2\pi T(h_i - h_o)}{\ln(r_o) - \ln(r_i)} \quad (1)$$

where T is the transmissivity, h_i is the head on the inner surface with radius r_i , and h_o is the head on the outer surface at radius r_o . Therefore fracture transmissivity is given by:

$$T = \frac{Q \ln(r_o) - \ln(r_i)}{2\pi(h_i - h_o)} \quad (2)$$

For the experimental setup $r_o = 30$ mm, $r_i = 1.96$ mm, $h_o = 0.05$ m and $h_i \sim 100$ m, transmissivity can simply be calculated from:

$$T = 1.183 \times 10^{-12} \frac{Q}{P_p} \quad (3)$$

if the fluid flux (Q in $\mu\text{l}\cdot\text{hr}^{-1}$) and pore pressure (P_p in kPa) are known. This relationship was used to calculate the transmissivity of the fracture throughout the experiment. A correction could be made for the change in contact area between the blocks, and hence the outer radius of the fracture, however scoping calculations demonstrated this had only a negligible effect on the overall calculation compared with the uncertainty of how the fracture contact area changed with time.

4.2.2.6 Calculation of self-sealing potential (SSP)

Experience has shown that there is considerable variation in flow in repeat experiments. For example, in the current study the stable flow stage for samples of Opalinus Clay showed variation between 6.6 $\mu\text{l}/\text{h}$ and 207 $\mu\text{l}/\text{h}$, nearly two orders of magnitude variation. The fracture topology is measured to ascertain whether variation in flow is related to the surface characteristics of the fracture. However, flow is likely to be associated with asperities and fracture roughness is not a measure of mismatch between the top and bottom fracture surface and therefore an estimate of the properties of asperities.

The experiment was designed to determine three different flow magnitudes: initial water flow, steady water flow, and water flow during shearing. From these three parameters it was aimed to determine the change in flow as a result of (1) hydration of the fracture and (2) shear along the fracture. The change in flow determines the self-sealing potential of the rock. Therefore, self-sealing potential is defined as:

$$SSP_{H_2O} = \frac{\text{Flow of water}_{initial}}{\text{Flow of water}_{steady}} \quad \text{and} \quad SSP_{\tau} = \frac{\text{Flow of water}_{steady}}{\text{Flow of water}_{shear}}$$

This measure of self-sealing potential removes the variation in flow and defines a proportional variation. It is still expected that variation will exist but that this approach removes a large part of the variation. It should be noted that that $SSP > 1$ means that gas flow is reduced. Therefore, a SSP_{H_2O} of 2 means that hydration of the fracture has resulted in a halving of the gas flow. Conversely, $SSP < 1$ means that flow has increased. Therefore, an SSP_{τ} of 0.5 means that flow has doubled because of shearing.

4.2.2.7 Calibration

The apparatus comprised three syringe pumps, three load cells, one pore pressure sensor, one sensor for measuring displacement, and one induction sensor for measuring vertical displacement. Each type of device had a different calibration routine and/or cycle between repeat measurements.

Only two of the syringe pumps could be calibrated as the third was modified to give direct drive to system and as such didn't need calibration. The syringe pumps were calibrated at regular intervals by pressurising at 0 (atmospheric), 2.5, 5, 7.5, 10, 7.5, 5, 2.5, and 0 MPa. At each stage the pressure reading of a Fluke pressure calibrator was noted to give precise pressure measurement. The Fluke calibrator was itself re-calibrated by the manufacturer on an annual basis to industry standards. A similar approach was used for the pore pressure transducer; however, it was pressurised at 0, 0.8, 1.6, 2.4, 3.2, 4, 3.2, 2.4, 1.6, 0.8, and 0 MPa.

The displacement devices were only re-calibrated at the end of the experimental programme. For all devices the manufacturer supplied calibration was initially assumed. Re-calibration was performed using calibration blocks, which were manufactured to high standard and allowed the devices to be displaced by known distances. By using multiple calibration blocks over a range of lengths, it was possible to confirm calibration of all three devices.

The load cells were not easily accessible and re-calibration was not straightforward. Therefore, manufacturer supplied calibrations were adopted and at the end of the experimental programme, the calibration was confirmed. To calibrate the load cells, the device was removed from the apparatus and placed within a small hydraulic load-frame. Each load cell was placed one at a time in series with a calibration load cell device. The load cells were loaded over a range of steps and the electrical output was noted against the load reading of the calibration device. The latter was re-calibrated annually by the manufacturer to industry standards.

For all calibration data the slope, intercept, and R^2 was calculated, the latter being used to ascertain whether the calibration had been of sufficient quality, with R^2 expected to be close to unity. As well as R^2 , graphs of the calibration were also inspected. Where necessary, calibration was repeated if R^2 was not acceptable. During the experimental programme, no device showed significant deviation from the initial calibration.

4.2.3 Research plan

Table 7 summarises the planned test programme. For Callovo-Oxfordian claystone and Opalinus Clay, a total of eight tests each were planned. This programme included a repeat shear test at ambient conditions to investigate repeatability, a series of tests initially fractured at ambient condition and flow investigated at a range of temperatures, and a series of tests where fracturing and flow were investigated at raised temperature. These eight tests described repeatability, defined the relationship between temperature and flow for both fractures formed at ambient conditions (during repository construction), and at raised temperature (post-closure). A reduced plan was made for Boom Clay, with a total of five tests. Two of these were repeat tests at ambient conditions. The remaining tests investigated flow in fractures that formed at temperature.

Note: The test name denotes the important experimental parameters: the letters denote the rock type; the first two numbers describe the temperature of initial shearing; the last two numbers describe the temperature of the repeat shear stage; the final letter (not always used) denotes a repeat test.

Table 7 - Planned experimental programme.

Rock	Test number	Temperature of fracture (°C)	Temperature of flow stage (°C)
Callovo-Oxfordian claystone	COX2020a	20	20
	COX2020b	20	20
	COX2045	20	45
	COX2065	20	65
	COX2090	20	90
	COX4545	45	45
	COX6565	65	65
	COX9090	90	90
Opalinus Clay	OPA2020a	20	20
	OPA2020b	20	20
	OPA2045	20	45
	OPA2065	20	65
	OPA2090	20	90
	OPA4545	45	45
	OPA6565	65	65
	OPA9090	90	90
Boom Clay	BC2020a	20	20
	BC2020b	20	20
	BC4545	45	45
	BC6565	65	65
	BC9090	90	90

4.1 Results and discussion

At the time of reporting, a total of 13 shear experiments had been completed. This included all the experiments planned in Opalinus Clay and enough experiments in Callovo-Oxfordian claystone to make statements about the influence of temperature on shear properties and flow. None of the experiments using Boom Clay had been conducted.

Table 8 - Summary of experiments completed. Note: tests in red have yet to be conducted and will be complete by the end of the project.

Rock type	Normal load (MPa)	Pore pressure (MPa)	Temperature of initial shear	Status
Opalinus Clay	3.6	1	Ambient	1 2 3 4 5

	3.6	1	Raised	45 67 90
Callovo-Oxfordian	3.6	1	Ambient	1 2 3 4 5
	3.6	1	Raised	45 67 90
Boom Clay	3	1	Ambient	1 2
	3	1	Raised	45 67 90

It is not necessary to report the detail of every test. Therefore, one test is introduced in detail to describe the features seen and the method used to calculate parameters. Following this description, the results will concentrate on comparisons between tests. All tests showed typical behaviour. The selected example had additional features of note.

4.1.1 Example test: OPA2065 (FPR_23_055) – Opalinus Clay

Test OPA2065 (FPR_23_055) was started 10:00am on the 6th June 2023 and was completed at 12:41 on the 20th June 2023, a total of 14 days duration. The test was conducted on Opalinus Clay with the shear direction parallel to bedding. The initial shear stage was conducted at ambient temperature (~20°C), with the flow and repeat shear stages conducted at 65°C.

4.1.1.1 Initial shear

The first stage of the experiment takes the intact cylindrical sample of around 53 mm height and 60 mm diameter and creates a shear fracture at the midplane, creating two halves of the sample around 26 mm in height. Figure 10 shows the results of the initial shear stage. Figure 10a shows the stress result. A normal load of 3.5 MPa was placed on the sample, but this can be seen to have increased as the sample was sheared (Figure 10b). This is commonly seen in the direct shear experiments. As the sample begins to move it results in the loading beam to slightly move from vertical, resulting in an increase in the load recorded by the two normal load cells. It is believed that the change seen was not problematic and did not require correction. The shear stress response is relatively complex. Initially a steep gradient is seen in shear stress, which becomes a linear response from a strain of 0.01 onwards. The linear region of the stress-strain relationship represents the shear modulus and has a magnitude of 49 MPa. A linear response is seen until the first highlighted event line at a strain of 0.038. At this time, the shear stress starts to deviate from linear. However, relatively quickly the sample returns to the same stress-strain linear relationship. Therefore, the deviation represents some form of shear stress relief in the sample and may indicate the onset of fracturing. This event does correspond with a reduction in normal stress, which suggests that the loading beam has returned to vertical, and some movement of the sample has occurred. Normal displacement of the sample also occurred, suggesting the formation of dilatant fracture. Shear stress continued to increase until it reached a peak of 1.98 MPa, as shown by the second event line. Following peak stress, a decrease in stress of 0.25 MPa occurred, followed by a short-lived increase in stress. A second peak in stress occurred at a strain of 0.042 with a magnitude of 1.79 MPa, as highlighted by the third event line. Again, this corresponds to an increase in normal displacement and a change in normal load. This event is followed by a gradual decrease in shear stress and is interpreted as being the onset of stable sliding along the fully formed shear fracture. A fully formed residual strength is not achieved by the limit of shear of the apparatus, although Figure 10a shows an estimate of residual strength. Throughout this stable sliding phase, normal displacement continued to increase. Figure 10d shows the temperature of the sample during the experiment. Although temperature

did vary during the shear test, it is not a significant change and no changes in temperature correspond with changes in experimental parameters.

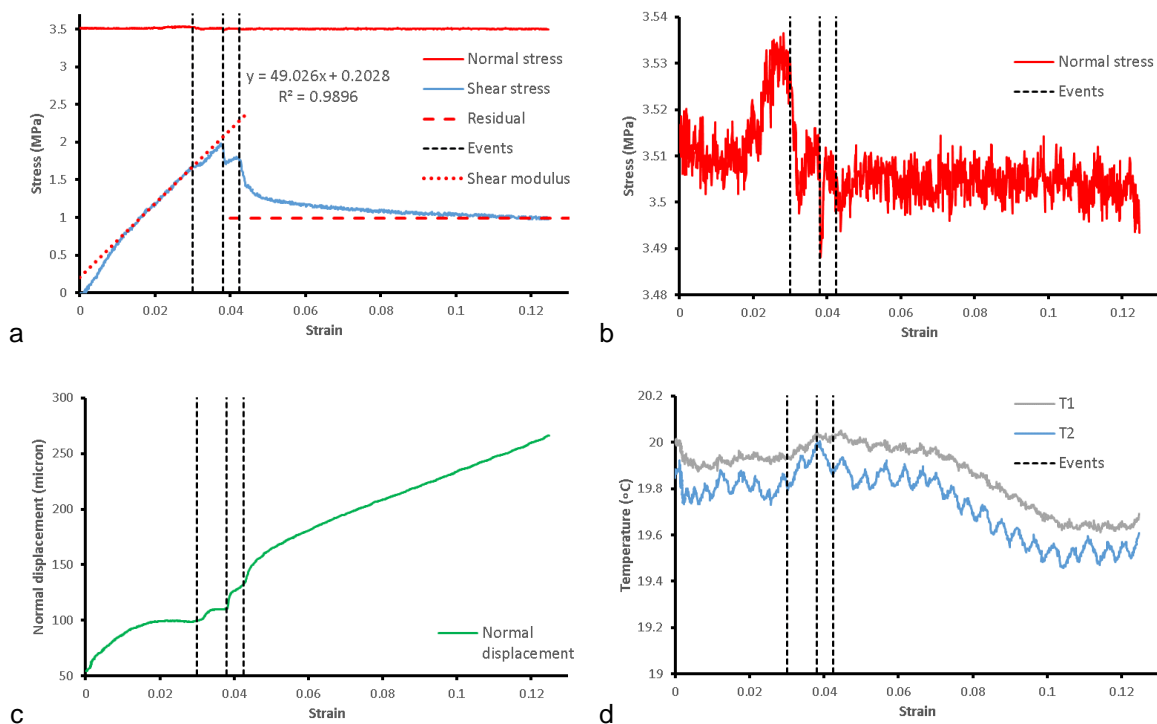


Figure 10 - Initial shear stage of test OPA2065. a) Stress response; b) Normal stress; c) Normal displacement; d) Temperature of the sample.

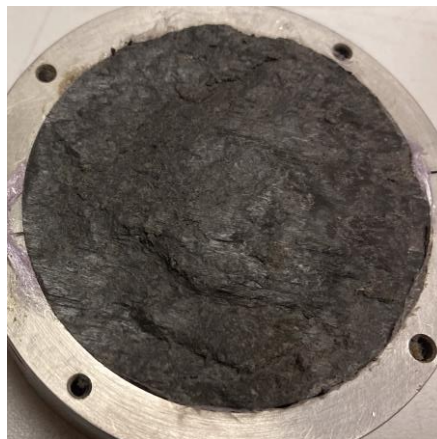


Figure 11 - Photograph of the fracture surface formed in the top sample.

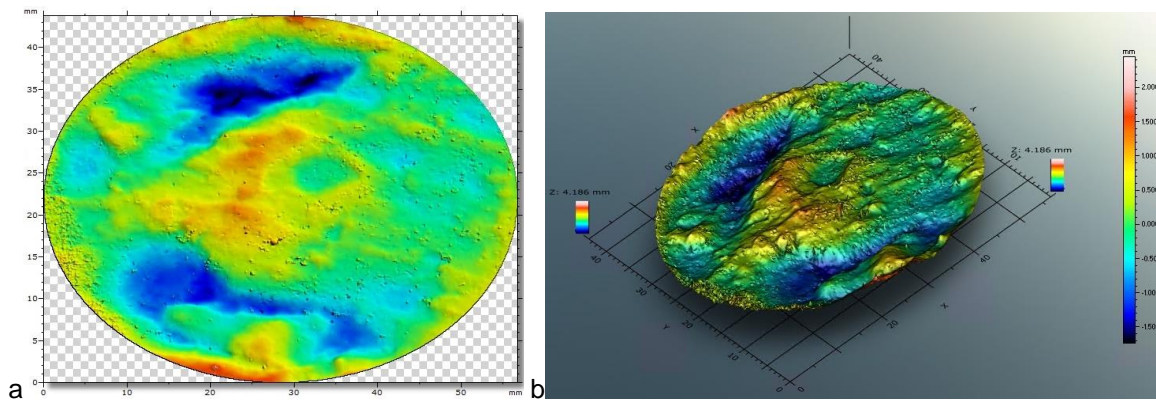


Figure 12 - Topology of the fracture of test OPA2065 after initial shearing.

4.1.1.2 Flow stage

After the shear fracture had been formed and scanned, a 4mm hole was drilled in the top fracture surface to add an injection bore. The fracture surfaces were re-aligned during re-assembly of the apparatus and normal load was created once more. Figure 13 summarises the results for the flow stage of the experiment. As shown, little of significance happened in stress (Figure 13a) prior to the repeat shear (Figure 13a; described later). The sample underwent a high degree of dilation as water was injected into the fracture and the clay swelled (Figure 13c).

Figure 14 shows the flow of water into the fracture during the flow stage of the experiment. As can be seen, flow was initially very high, greater than 4,500 $\mu\text{l/h}$ (Figure 14a). However, this quickly reduced to a level of approximately 100 $\mu\text{l/h}$ (Figure 14ab). The data were carefully scrutinised to estimate the initial flow of water. At the start of injection, it is common for the pipework from the injection pump to the tip of the injection bore to retain a quantity of air. In addition, the asperities of the fracture will be air filled after re-assembly. The syringe pump was operated at a low pressure to flush air from the system and quickly pressure was sustained. At the time it was deemed that the system had been flushed of air. The syringe pump was then set to a constant pressure of 1000 kPa. This gave the initial spike in flow. Once 1000kPa had been generated in the fracture, flow was then deemed a real flow into the fracture. As highlighted in Figure 14ac, initial flow was defined as an average of 916 $\mu\text{l/h}$. Flow quickly reduced to a steady value, this time with an average flow of 113 $\mu\text{l/h}$. From these two values of flow, the sealing potential for water (SSPH_{2O}) can be defined as 8.1. Therefore, the flow of water into the fracture resulted in a decrease in flow of almost one order of magnitude. In the current test, flow reduced from the initial high level to a steady flow relatively quickly. In many tests, this reduction was slow. However, this tended to occur in tests where the overall flow rate was less than that seen in the current test.

Figure 14bc shows that active shearing along the fracture had a significant impact on flow properties. Flow reduced from an average of 113 $\mu\text{l/h}$ to a new steady flow of 16.2 $\mu\text{l/h}$. From these two values of flow the self-sealing potential for shear (SSP \square) can be defined; in this case 6.98. Again, almost one order of magnitude reduction in flow. Therefore, for Opalinus Clay at 65°C, hydration of fractures reduces flow by one order of magnitude and shear movement along the fracture reduces flow also by one order of magnitude. However, as shown in Figure 14bc, continued shear resulted in an increase and then a decrease in flow. The increase in flow had an average flow rate of 34.1, more than twice the lowest value of flow. By the end of the shear stage, flow had almost reduced back to its lowest level. It should be noted that this increase in flow was only seen in a couple of tests and was not the normal behaviour seen. It is interpreted that continued shear resulted in significant mismatch between the two faces of the fracture and that this resulted in an increase in flow. Further movement and closure of the mismatch resulted in the reduction of flow.

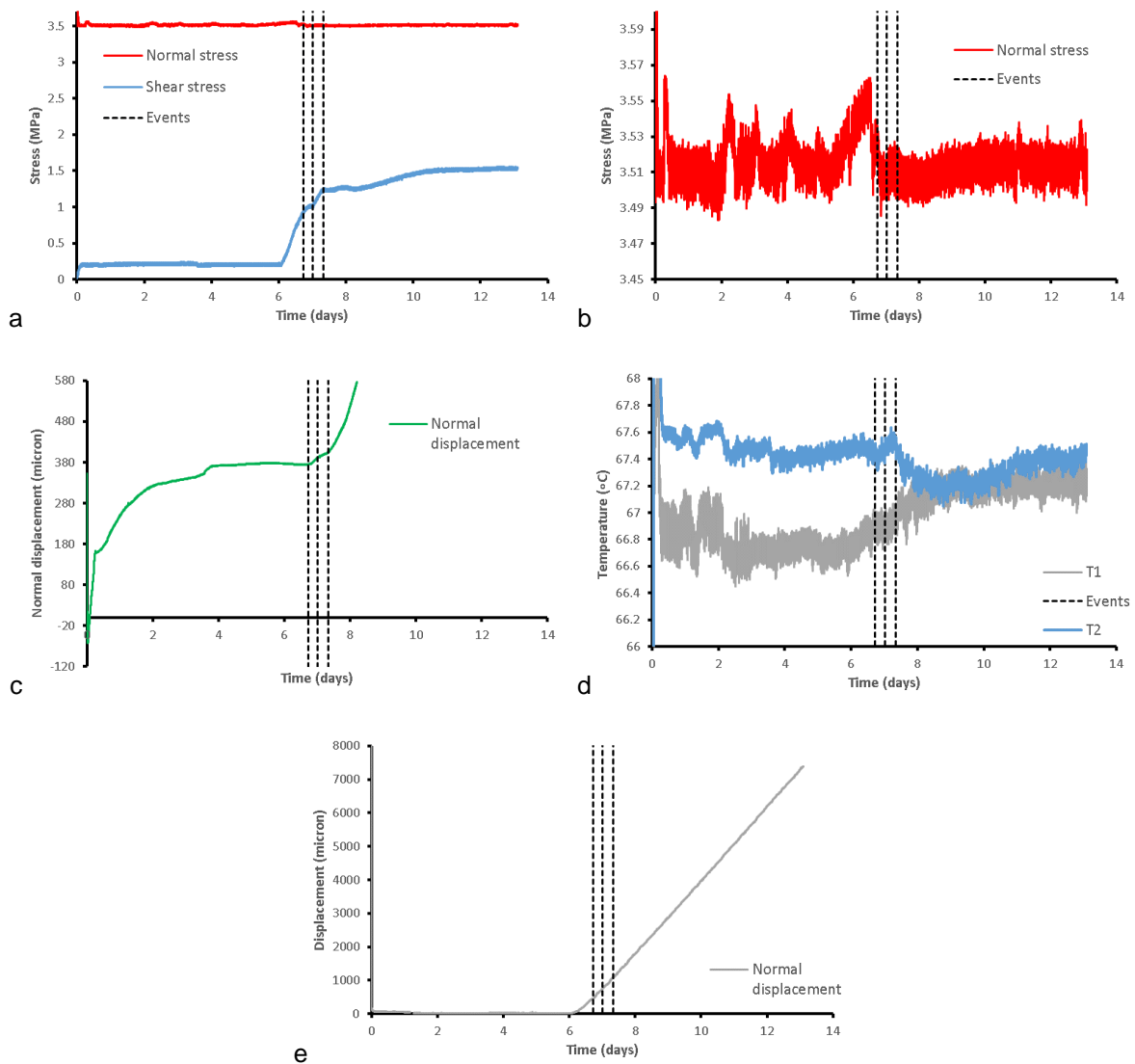


Figure 13- Flow shear stage of test OPA2065. a) Stress response; b) Normal stress; c) Normal displacement; d) Temperature of the sample; e) Shear movement.

In summary, hydration was seen to reduce fracture flow by one order of magnitude, with active shear reducing flow by a further order of magnitude.

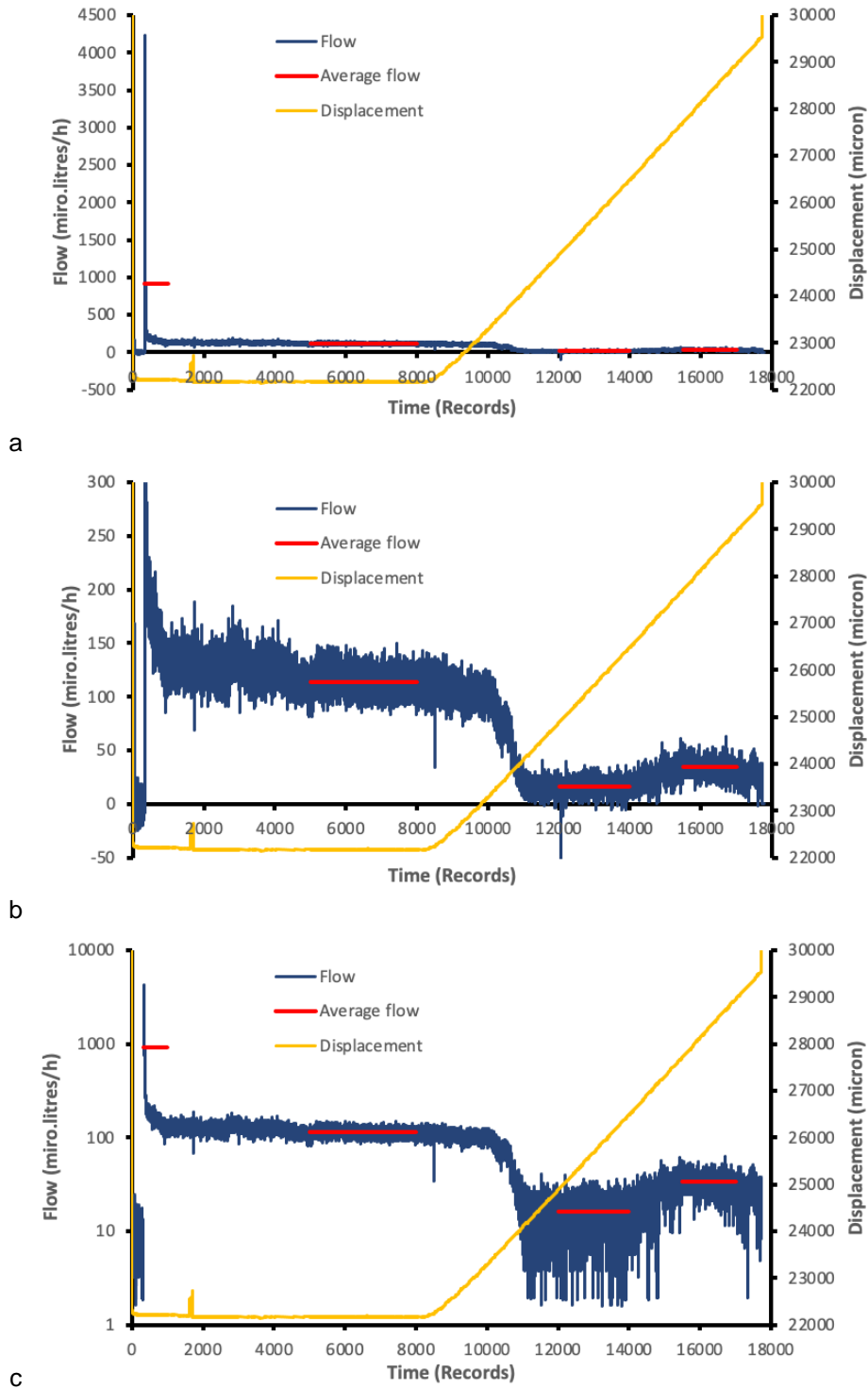


Figure 14 - Flow during test OPA2065. a) Flow; b). Detail of flow; c) Log of flow.

4.1.1.3 Repeat shear

Figure 15 shows the repeat shear stage of the experiment in detail. Shear was started at Day 6.06 (Figure 13e). This resulted in shear stress increasing quickly (Figure 15a) with no change in normal displacement (Figure 15c). The linear stress-strain response (Figure 15a) defines the shear modulus, and for the repeat shear is 86.7 MPa. The first event line highlights when the data deviates from the linear. This is likely to be the first movement along the fracture. It corresponds with a decrease in

measured normal stress (Figure 15b), which as outlined earlier is likely to be a return to vertical of the normal loading frame. Normal displacement (Figure 15c) also showed an increase at this time. However, the second event line shows the time when shear stress started to increase again, before reaching a peak at the third event line. This could be interpreted as peak stress. However, as the fracture continued to shear, shear stress increased, as did normal displacement. Peak stress has been defined later in the experiment at 1.53 MPa when considering all other repeat shear tests. The acceleration of displacement suggests that the two fracture faces were sliding past one another on a slope, increasing the overall height of the sample.

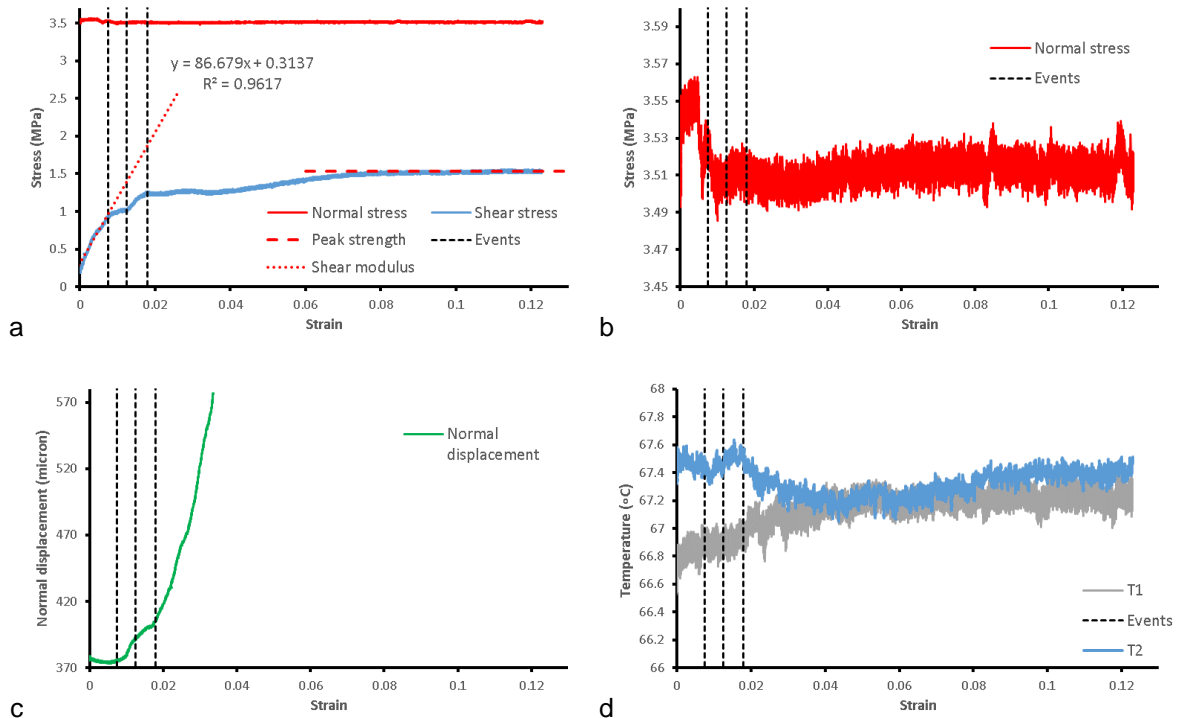


Figure 15 - Repeat shear stage of test OPA2065. a) Stress response; b) Normal stress; c) Normal displacement; d) Temperature of the sample.

Figure 16 compares the shear test results for the two phases of shear testing in the current test. In a standard shear experiment, it is expected to see elastic-brittle-plastic behaviour, with the brittle stage defining the peak strength and the plastic behaviour defining the residual strength. Re-shearing of the fracture would expect to see elastoplastic behaviour, with a peak strength almost equal to the initial residual strength, or for stable sliding to occur on repeat testing at a residual strength equal to the residual strength seen for the intact sample. This is not seen in the current data. It could be noted that the initial departure from a linear stress-strain response (event line 1 in Figure 15) would have resulted in a peak strength equal to the residual strength of the intact sample. This might suggest that the fracture began to “lock” as it moved, and that greater stress was required to overcome this locking, resulting in higher levels of shear stress than expected. The stress response from the repeat stage may highlight three episodes of “locking” of the fracture. This has resulted in dissimilar residual strengths. Also unusual is the shear modulus of the two stages. In the repeat shear, the shear modulus is higher than for the intact rock. This would suggest the fractured sample was more compliant than the intact rock. This is unlikely and suggests that the shear displacement recorded may have underestimated true displacement of the two blocks, possibly as some lateral movement of the top block occurred. It should be noted that the initial and repeat shear phases of the experiment were conducted at different temperatures.

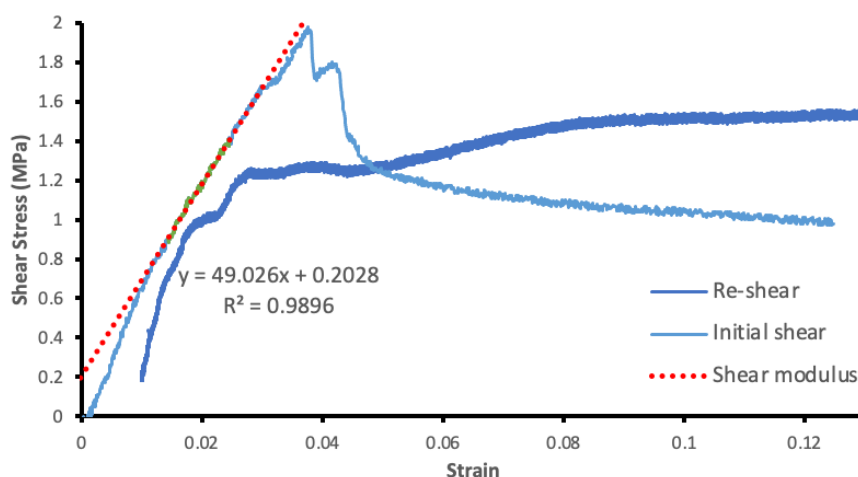


Figure 16 - Comparison of shear test results for both shear tests conducted on sample OPA2065.

Figure 17 shows a photograph of the two fracture surfaces during decommissioning of the test. Some brown staining is apparent, although it is believed this is burnt cling-film that encased the sample when in the apparatus. Some polishing is apparent. While the colouration seen in Figure 17 appears much lighter than in Figure 11, this is largely down to differences in lighting conditions. No significant colouration differences were noted between tests conducted in this, or Eurad-GAS shear experiments and suggests that samples had not significantly dried. In fact, one failed test was taken from the rig and showed significant drying effects within 24 hours of air exposure.



Figure 17 - Photograph of the fracture surface formed after repeat shearing.

Figure 18 shows the laser scan results for the shear surfaces shown in Figure 17. The “form” of the surface has been removed to reveal the roughness of the surface. The roughness of the fracture was determined to be 0.451 mm and 0.438 mm for the bottom and top samples respectively, RMS roughness was 0.571 mm and 0.583 mm, and peak to valley height was 3.522 mm and 3.693 mm. No significant differences are seen in the surface data between the top and bottom fracture surfaces. It can be noted that roughness, RMS roughness, and peak to valley height all reduced between the initial shear and the re-shear.

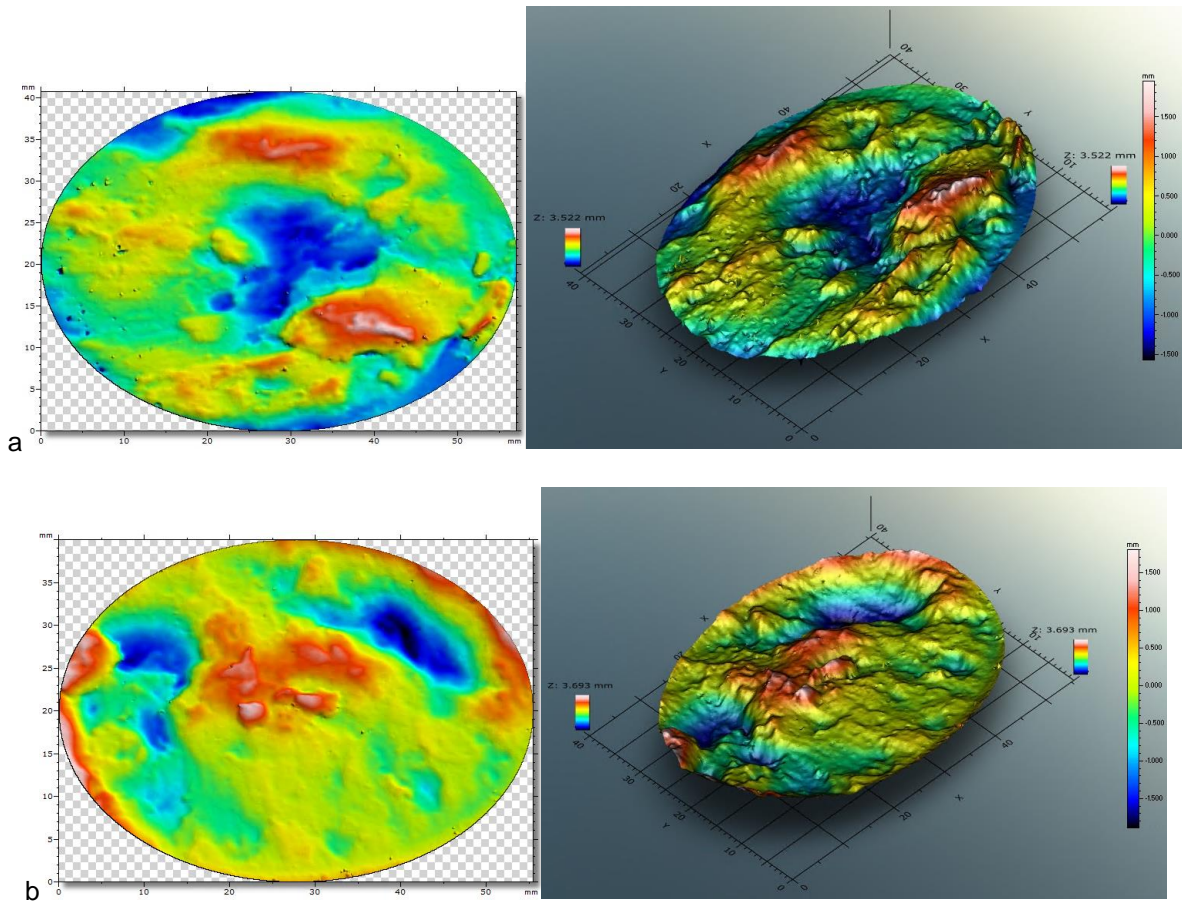


Figure 18 - Topology of the fracture of test OPA2065 after re-shearing. a) Bottom fracture face; b) Top fracture face.

4.1.1.4 Results from test OPA2065

Table 9 - Results for test OPA2065.

Test	OPA2065
Sample number	FPR_23_055
Date start	06/06/2023
Date end	20/06/2023
Quality	Good
Rock	OPA
Orientation	Parallel
Diameter	59.45 mm
Height	53.24 mm

Weight	357.53 g	
Density	2.419 g/cc	
	Initial	Re-shear
Average temperature	19.8 °C	67.2 °C
Average normal stress	3.51 MPa	3.51 MPa
Peak strength	1.98 MPa	1.53 MPa
Shear modulus	49.0 MPa	86.7 MPa
Maximum strain	0.13	0.12
Residual strength	0.99 MPa	1.51 MPa
Average roughness	0.465 mm	0.445 mm
RMS roughness	0.597 mm	0.577 mm
Peak to Valley height	4.343 mm	3.608 mm
Initial flow of water	916 µL/hr	
Stable flow of water	113 µL/hr	
Flow of water during shear	16.2 µL/hr	
SSP _{H₂O}	8.08	
SSP _τ	6.98	

4.1.2 Comparison of all tests

At the time of reporting, thirteen tests had been completed, with at least another nine shear tests to be completed before the end of the project. Of the thirteen completed tests, nine tests were conducted using Opalinus Clay, with four tests using Callovo-Oxfordian claystone. Therefore, all tests had been completed in Opalinus Clay, with enough tests to make statements about the influence of temperature on fracture properties in COx. Table 10 and Table 11 show all the achieved data for the thirteen experiments reported.

4.1.3 Repeatability in Opalinus Clay

Figure 19 shows results for Opalinus Clay on repeat tests. Figure 19a shows the stress-strain result for the two tests conducted for repeatability purposes, tests OPA2020a and OPA2020b. As can be seen, significant differences occur between the two tests. Note: test results have been transposed along the x-axis for display purposes.

Figure 19a shows that test OPA2020b had a varying stress-strain response in the first 0.01 strain. This can be attributed to the characteristics of direct shear rigs. Once a linear stress-strain response had been established, defining the shear modulus, the two samples show a similar slope. Once shear stress started to deviate from linear this is when dissimilarities are seen between the two tests. Test OPA2020a

showed a rounded peak in shear stress, with a peak of 2.28 MPa, with shear stress gradually progressing to a residual stress of 1.51 MPa. In test OPA2020b, there was a more abrupt transition from linear stress-strain response with a peak shear stress of 2.9 MPa and a quick reduction in shear stress, losing around 1 MPa in shear stress rapidly. This was followed by a reducing shear stress at a rate similar to test OPA2020a, with a minimum residual stress of 1.35 MPa. Therefore, comparing the two tests, both had a similar shear modulus, one showed classic elastic-brittle-plastic behaviour with a high peak shear stress and lower residual strength compared with the other test, that showed more gradual brittle behaviour. This suggests that test OPA2020b formed a simple fracture that relieved considerable shear stress and allowed simple slip along the fracture. In tests OPA2020a, a more gradual formation of a slip plane occurred and probably means that multiple parallel fractures were formed.

The full picture is more complicated when considering all tests conducted in Opalinus Clay when initially sheared at ambient temperature (Figure 19b). It must be considered that all these five tests were conducted as identical as possible. The three additional tests shown in Figure 19b show different results to the two tests shown in Figure 19a. Tests OPA2045b and OPA2065 show similar response to one another. These have a lower slope in stress-strain, indicating that these samples are not as compliant as tests OPA2020a and OPA2020b. Both tests show multiple peaks, as described earlier, suggesting that multiple fractures formed, with the initial fracture “locking” before a stable slip plane was created. Test OPA2090 shows very different results. In this test, there is no brittle response, with elastoplastic behaviour seen. The elastic region has a similar slope to the repeatability tests OPA2020a and OPA2020b. The form of the stress-strain response is similar to results achieved for re-shear tests. This suggests that the sample may have either had a pre-existing bedding plane weakness, or that it failed during test assembly. If care is not taken during setting up the experiment, it is possible to cause tilt of the top block assembly if the swan-neck arrangement transmitting shear stress from the top sample assembly to the shear load cell is not properly supported at the shear load cell. Tilting can cause the sample to split along the bedding plane and was known to have occurred in test OPA2045a, leading to repeat of the test. In this latter test, the sample was slightly larger than a 60 mm diameter and as a result it was difficult to load the upper sample collar into the sample holder, resulting in tilting and accidental fracture of the sample. This was not seen in tests OPA2090. However, this test was also slightly larger than 60 mm diameter and this may have caused the sample to break during assembly. No test conducted in Opalinus Clay in any of the shear apparatus at BGS has shown a stress-strain result similar to test OPA2090 and therefore it is concluded this sample fractured prior to the start of shearing. It can be concluded that repeatability in Opalinus Clay is not as good as hoped in direct shear. This means that considerable spread in data is likely.

Table 10 - Results for all tests. Note: OPA – Opalinus Clay; COx – Callovo-Oxfordian claystone; + good test; - incomplete test.

Number	Rock type	Test number	FPR No.	Date start	Date end	Quality	Sample diameter	Sample height	Sample Weight	Average density	Initial shear					Re-shear					Flow						
											Temperature	Normal stress	Peak strength	Stiffness	Maximum strain	Residual strength	Temperature	Normal stress	Peak strength	Stiffness	Maximum strain	Residual strength	Initial flow of water	Settled flow of water	Flow during shear	SSP _{H2O}	SSP _t
							mm	mm	g	g/cc	°C	MPa	MPa	MPa		MPa	°C	MPa	MPa	MPa		MPa	μL/hr	μL/hr	μL/hr		
1	OPA	OPA2020a	FPR-22-080	20/12/2022	09/01/2023	+	59.81	52.90	364.30	2.45	19.85	3.61	2.28	101.2	0.131	1.51	20.26	3.48	1.20	56.71	0.144		8529	206.5	8.27	41.30	24.99
2	OPA	OPA2020b	FPR-22-082	10/01/2023	26/01/2023	+	59.49	53.05	364.48	2.47	21.78	3.63	2.90	125.9	0.106	1.35	21.08	3.51	0.72	91.09	0.181	0.68	1866	28.60	26.71	65.23	1.07
3	COx	COx2020a	FPR-22-052	26/01/2023	13/02/2023	+					21.06	3.61	4.49	144.1	0.000	1.95	20.52	3.49	0.89	64.86	0.092	0.82	9993	75.51	6.01	132.33	12.56
4	OPA	OPA9090	FPR-22-083	06/04/2023	02/05/2023	+	59.87	51.69	356.96	2.45	92.35	3.54	6.33	179.4	0.100	1.85	96.74	3.57	2.50	112.6	0.115	2.42	11.05	6.64	6.50	1.67	1.02
5	OPA	OPA6565	FPR-22-098	22/03/2023	05/04/2023	+	59.54	52.89	358.67	2.44	68.08	3.55	2.50	68.76	0.109	1.48	67.59	3.39	1.75	102.9	0.120	1.71	180.2	9.43	9.07	19.12	1.04
6	OPA	OPA4545	FPR-22-079	06/03/2023	22/03/2023	+	60.02	52.46	366.71	2.47	45.64	3.53	3.43	157.6 5	0.107	1.53	46.01	3.61	1.10	146.2	0.128	0.93	2308	53.84	7.89	42.87	6.82
7	OPA	OPA2045a	FPR-22-081	03/05/2023	17/05/2023	-	60.07	53.00	369.67	2.46						45.87	3.55	2.12	127.1	0.118	1.96	30.99	12.11	11.78			
8	OPA	OPA2045b	FPR-23-054	22/05/2023	06/06/2023	+	58.90	53.22	350.39	2.42	18.84	3.45	1.84	40.49	0.136	0.97	45.56	3.50	1.26	111.4	0.104	1.22	87.54	5.17	7.64	16.93	0.68
9	OPA	OPA2065	FPR-23-055	06/06/2023	20/06/2023	+	59.45	53.24	357.53	2.42	19.82	3.51	1.98	49.03	0.135	0.99	67.19	3.51	1.53	86.70	0.123	1.51	916.1	113.4	16.25	8.08	6.98
10	OPA	OPA2090	FPR-23-053	20/06/2023	12/07/2023	+	60.04	53.13	366.56	2.44	19.62	3.48	1.18	93.17	0.146	1.15	94.66	3.51	2.19	84.30	0.168	1.85	40.00	8.32	84.23	4.81	0.10
11	COx	COx9090	FPR-23-058	12/07/2023	25/07/2023	+	59.82	52.91	362.91	2.44	92.07	3.60	5.47	93.17	0.149	2.75	93.63	3.27	2.24	103.3	0.009	1.85	3415	488.5	446.1	6.99	1.10
12	COx	COx6565	FPR-23-061	07/08/2023	15/08/2023	-	59.99	52.80	366.16	2.45	62.52	3.58	5.70	176.1	0.104	2.75	65.05	3.40					37.47	0.74	27418	50.91	0.00
13	COx	COx4545	FPR-23-096	12/09/2023	26/09/2023	-	59.88	53.25	362.89	2.42	45.91	3.61	5.49	176.1	176.1	2.90	46.31	3.52					47101	980.3	16.38	48.05	59.85

Table 11 - Fracture roughness results for all tests. Note: OPA – Opalinus Clay; COx – Callovo-Oxfordian claystone..

Number	Rock type	Test number	FPR No.	Initial shear - bottom			Initial shear - top			Re-shear - bottom			Re-shear - top			Average – Initial shear			Average – Re-shear		
				Roughness	RMS roughness	Peak to valley height	Roughness	RMS roughness	Peak to valley height	Roughness	RMS roughness	Peak to valley height	Roughness	RMS roughness	Peak to valley height	Roughness	RMS roughness	Peak to valley height	Roughness	RMS roughness	Peak to valley height
				mm	mm	mm	mm	mm	mm	mm	mm	mm	mm	mm	mm	mm	mm	mm	mm	mm	mm
1	OPA	OPA2020a	FPR-22-080																0.564	0.719	5.199
2	OPA	OPA2020b	FPR-22-082							0.703	0.893	5.266	0.425	0.544	5.131				0.789	1.041	8.870
3	COx	COx2020a	FPR-22-052							0.869	1.134	9.056	0.709	0.947	8.684				0.469	0.568	3.727
4	OPA	OPA9090	FPR-22-083	0.413	0.524	4.153	0.394	0.520	5.945				0.469	0.568	3.727	0.404	0.522	5.049	0.388	0.499	3.800
5	OPA	OPA6565	FPR-22-098	0.538	0.677	5.173	0.506	0.647	5.641	0.351	0.444	3.400	0.425	0.553	4.200	0.522	0.662	5.407	0.426	0.544	5.008
6	OPA	OPA4545	FPR-22-079	0.383	0.482	3.563	0.325	0.400	2.885	0.430	0.544	5.202	0.421	0.543	4.814	0.354	0.441	3.224	0.274	0.368	3.229
7	OPA	OPA2045a	FPR-22-081							0.280	0.348	2.822	0.268	0.388	3.635				0.584	0.710	4.030
8	OPA	OPA2045b	FPR-23-054	0.527	0.661	4.991	0.525	0.644	4.468	0.538	0.662	3.958	0.629	0.758	4.102	0.526	0.653	4.730	0.445	0.577	3.608
9	OPA	OPA2065	FPR-23-055	0.503	0.646	4.499	0.427	0.548	4.186	0.451	0.571	3.522	0.438	0.583	3.693	0.465	0.597	4.343	0.396	0.515	4.519
10	OPA	OPA2090	FPR-23-053	0.392	0.504	4.071	0.351	0.441	4.145	0.442	0.563	4.763	0.349	0.467	4.275	0.372	0.473	4.108	0.748	0.936	6.091
11	COx	COx9090	FPR-23-058	1.013	1.256	8.007	0.868	1.054	6.658	0.794	1.005	6.460	0.702	0.866	5.721	0.941	1.155	7.333	1.005	1.238	8.137
12	COx	COx6565	FPR-23-061	1.059	1.328	9.317	0.954	1.163	7.186				1.005	1.238	8.137	1.007	1.246	8.252			
13	COx	COx4545	FPR-23-096	1.893	2.413	15.100	1.814	2.271	12.498							1.854	2.342	13.799			

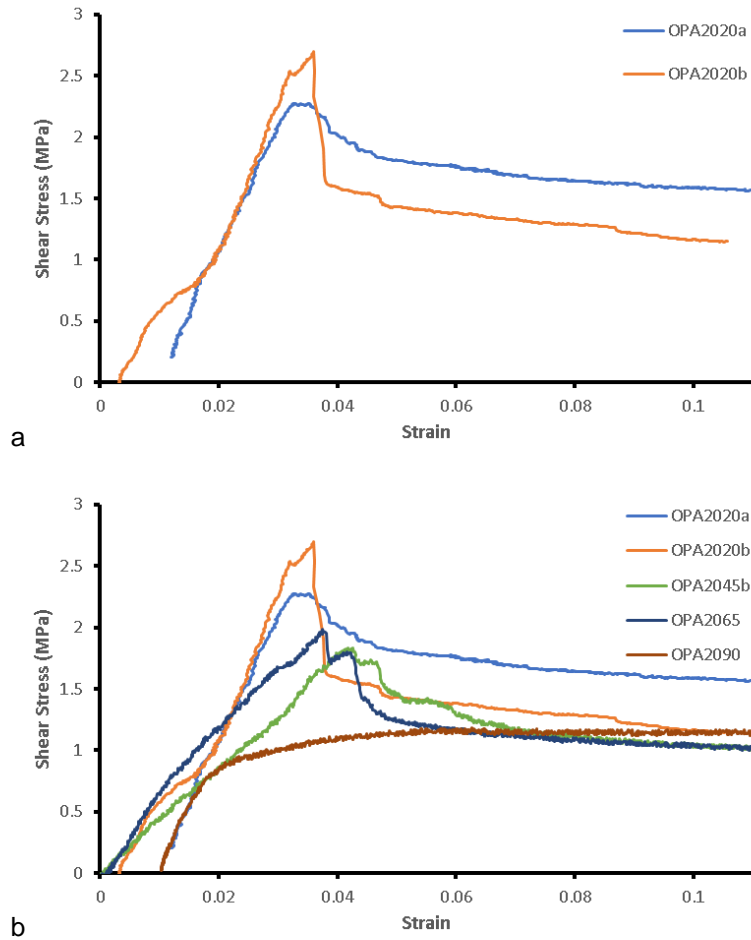


Figure 19 - Repeatability of shear data in Opalinus Clay. a) Repeatability tests; b) All tests initially sheared at ambient temperature.

4.1.4 Influence of temperature on shear strength in Opalinus Clay

Figure 20 shows the stress-strain results of mechanical shear of Opalinus Clay over a range of temperatures, with Figure 21 showing the results in more detail. Figure 20 shows that all four of the shear tests showed a similar linear stress-strain result, with test OPA6565 showing this general trend early in the test history before transitioning to a lower modulus. Figure 20a shows similar form for all four tests with a clear linear-brittle-plastic response. A small increase in peak shear strength is seen between tests conducted at 20 and 45 °C. However, the test at 65 °C shows a lower peak shear stress. This suggests that sample OPA6565 failed prematurely as a fracture formed parallel with the bedding direction along a pre-existing weakness. The test conducted at 90 °C shows considerably greater strength. This either highlights that test OPA6565 failed prematurely, or the relationship between strength and temperature is non-linear and greatly increases between 65 and 90 °C. Figure 21 shows that peak shear strength, shear modulus, and residual strength all increase with temperature. However, these plots also show the considerable spread seen in data at ambient temperatures. Considering all data and their variability, the trend is likely as the test conducted at 90 °C has a much greater value than the spread seen at 20 °C and is therefore a real increase.

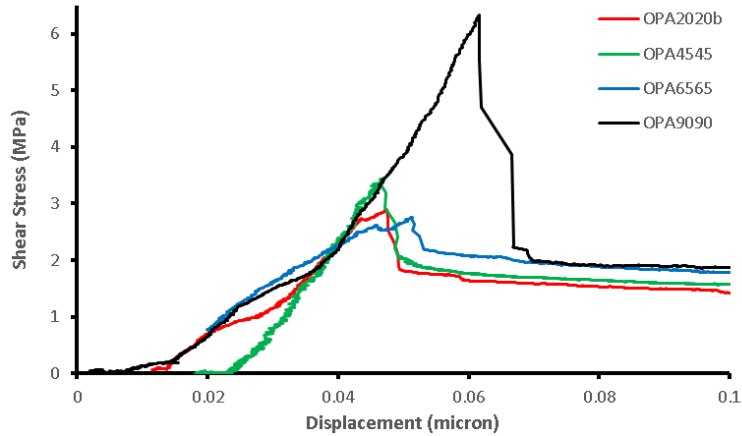


Figure 20 - Shear stress-strain result for four tests conducted over a range of temperatures in Opalinus Clay.

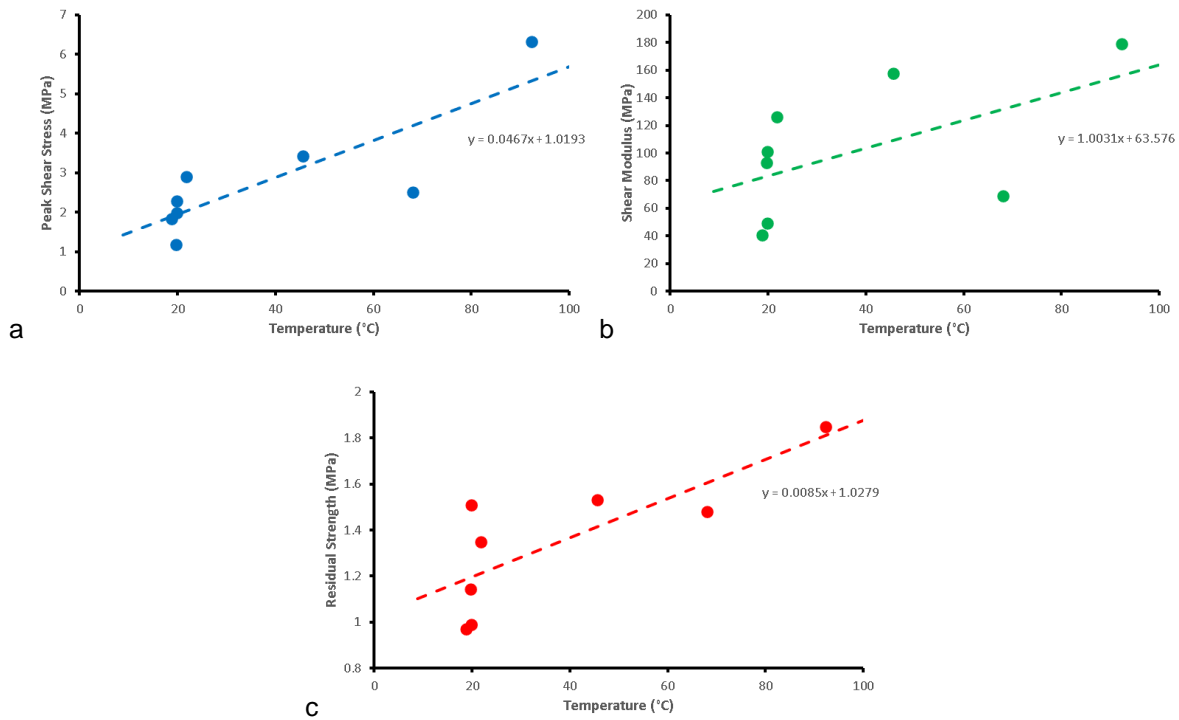


Figure 21 - Relationship between shear properties and temperature for Opalinus Clay. a) Peak shear strength; b) Shear modulus; c) residual strength.

4.1.5 Self-sealing potential of Opalinus Clay

Figure 22 shows the results of self-sealing potential in Opalinus Clay. Figure 22a shows the results of self-sealing potential as a result of hydration (SSP_{H_2O}). All tests showed a reduction in flow, therefore all results have a magnitude greater than 1. Two sets of data are displayed. The blue circles show the data for fractures that were initially fractured at ambient temperature, while the red circles show the data that were initially shear, and subsequently re-sheared, at elevated temperature. Both show a similar relationship, with self-sealing potential reducing with temperature. However, tests that are fractured at temperature have a greater self-sealing potential than those sheared at ambient temperature. Figure 22b also shows a reduction in self-sealing potential as a result of shear with temperature (SSP_{τ}).

However, the spread in the data is much greater than seen in SSP_{H2O}. Even considering the spread of data, the data do suggest that self-sealing potential by shear also reduces with temperature.

In conclusion, for Opalinus Clay, the effectiveness of self-sealing processes reduces at elevated temperatures.

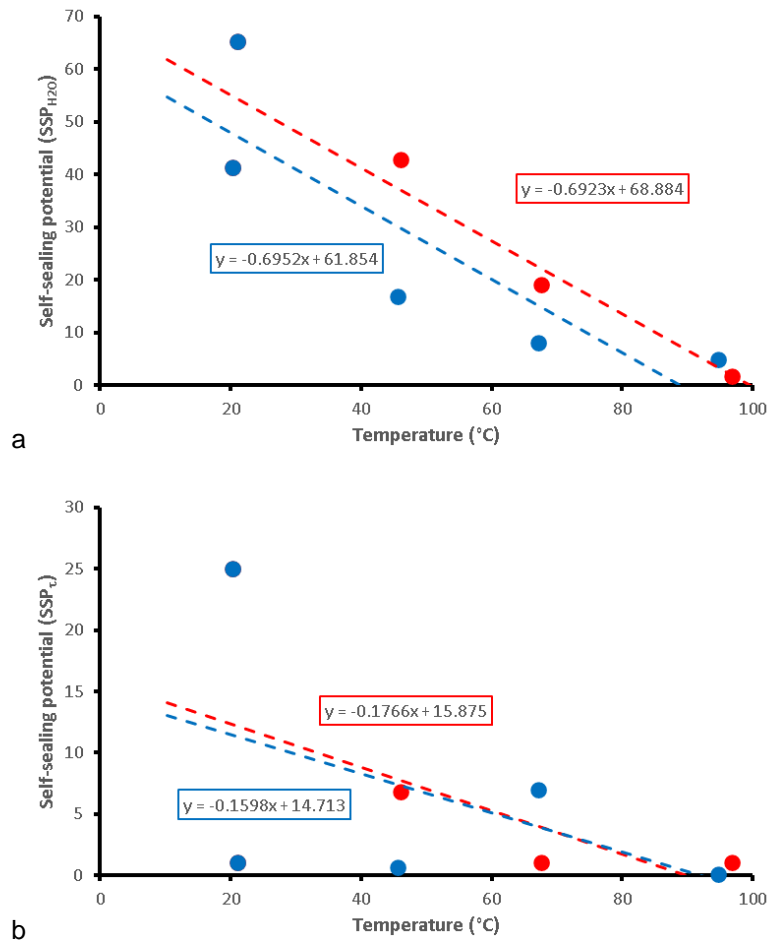


Figure 22 - Influence of temperature on self-sealing potential. a) Self-sealing potential as a result of hydration; b) Self-sealing potential as a result of active shear.

4.1.6 Fracture topology of sheared Opalinus Clay

Figure 23 shows the surface scan data for Opalinus Clay. Figure 23a shows the average of the two fracture surfaces of fracture roughness. The blue circles show that there appears to be little variation in roughness for the initial shear data. The red circles show that on repeat shear there is a change in fracture roughness, with roughness decreasing with increased temperature. The different relationships suggest that the presence of water during the repeat shear plays a role in altering fracture roughness. A similar result is seen for RMS roughness (Figure 23b), with little change in roughness for the initial shear, with a reduction in shear with temperature for the re-shear phase. The picture is more complex for peak to valley height (Figure 23c). In the initial shear data, there is a small increase in height with temperature. However, peak to valley height reduces with temperature for the re-shear data. All three datasets suggest that little alteration is seen in fracture topology for shear fractures created at different temperatures in initially intact samples. The presence of water during the re-shear phase results in the reduction in fracture roughness and peak to valley height. As self-sealing potential (SSP_{H2O}) is a function

of temperature, and fracture roughness alters with temperature, it is likely that fracture roughness plays a role in the effectiveness of fractures to self-seal.

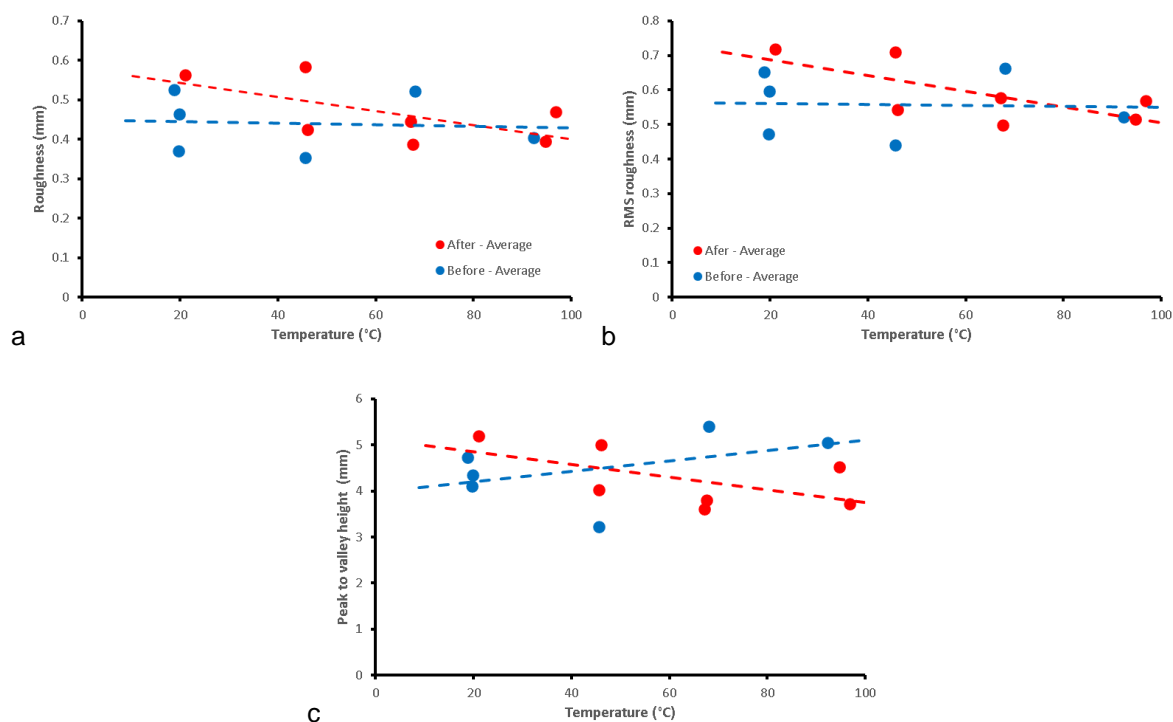


Figure 23 - Surface analysis of the laser scan data from Opalinus Clay. a) Roughness; b) RMS roughness; c) Peak to valley height.

4.1.7 Repeat shear in Opalinus Clay

Figure 24 shows the shear properties for Opalinus Clay during the repeat shear stage of the experiment. As can be seen, relationships are better defined than for the intact samples as each temperature has at least two re-shear experiments. A strong relationship is seen with increasing peak strength with temperature. At 100 °C, Opalinus Clay is 1.4 MPa stronger than at 20 °C. On re-shear, peak strength increases by 0.175 MPa per 10 °C. This compares with an increase of 0.467 MPa per 10 °C for the intact samples. Therefore, the strength increase in the intact samples is 2.7 times greater than seen in re-sheared samples. A similar result is seen for residual strength (Figure 24c), with residual strength increasing by nearly a factor of four between 20 and 100 °C. On re-shear, residual strength increases by 0.178 MPa per 10 °C. This compares with an increase of 0.085 MPa per 10 °C for the intact samples. Therefore, the strength increase in the intact samples is half that seen in re-sheared samples. The relationship for shear modulus (Figure 24b) is more difficult to define. Generally, a small increase is seen, suggesting that the stiffness of the sample increases with temperature. However, the spread in data is considerable and confused by the results seen at 45 °C. A small increase in shear modulus is suggested on re-shear, compared with a much more defined increase seen in the intact samples. It can be concluded that shear properties change with temperature, with higher temperatures resulting in increased peak strength, residual strength, and increased stiffness.

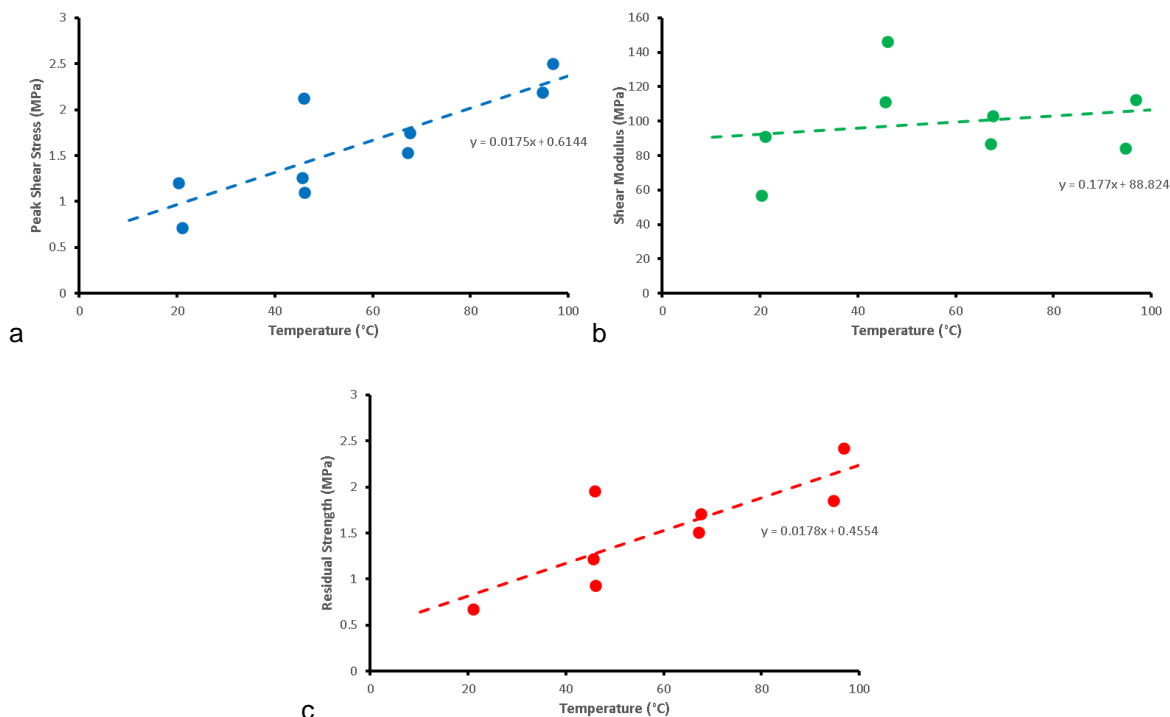


Figure 24 - Relationship between shear properties and temperature for repeat shearing in Opalinus Clay. a) Peak shear strength; b) Shear modulus; c) Residual strength.

4.1.8 Results for Callovo-Oxfordian claystone

The dataset for Callovo-Oxfordian claystone is incomplete at the time of reporting. However, four tests were completed at the four test temperatures in order to make preliminary statements about the role of temperature on self-sealing in Callovo-Oxfordian claystone.

Figure 25 shows the stress-strain results of the four tests, while Figure 26 shows the corresponding shear parameters. Figure 25 shows that the form of the stress-strain response was very similar for the four experiments. There were some differences in the initial response of the samples, although this can be attributed to “bedding in” of the apparatus and sample. All four tests progressed to a similar linear stress-strain relationship, defining the shear modulus. The overall form of the stress-strain response was smoother than seen in Opalinus Clay. At 20 °C a very smooth peak stress and transition to residual stress is seen. A similar response is seen at 45 °, while at 65 and 90 °C more brittle behaviour was seen with stress drops as the fracture slid. This shows that the mechanics of the test became more brittle at elevated temperatures. Figure 26a shows that peak strength generally increased with temperature. However, in detail, the tests at 45, 65, and 90 °C showed similar strength, especially considering the spread of data described above for Opalinus Clay. Residual strength (Figure 26c) also showed an increase with temperature, but again the tests at 45, 65, and 90 °C showed similar residual strength. In contrast, shear modulus was seen to decrease with increasing temperature (Figure 26b). This suggests that Callovo-Oxfordian claystone is less compliant at elevated temperatures. However, it has to be noted that the results at 45, 65, and 90 °C showed similar results.

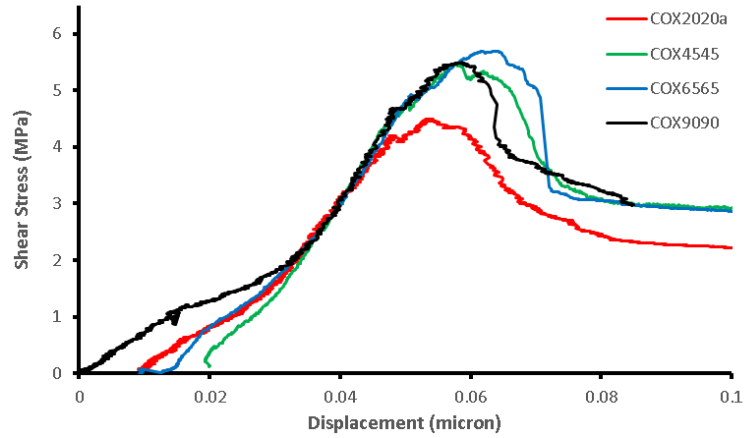


Figure 25 - Shear stress-strain result for four tests conducted over a range of temperatures in Callovo-Oxfordian claystone.

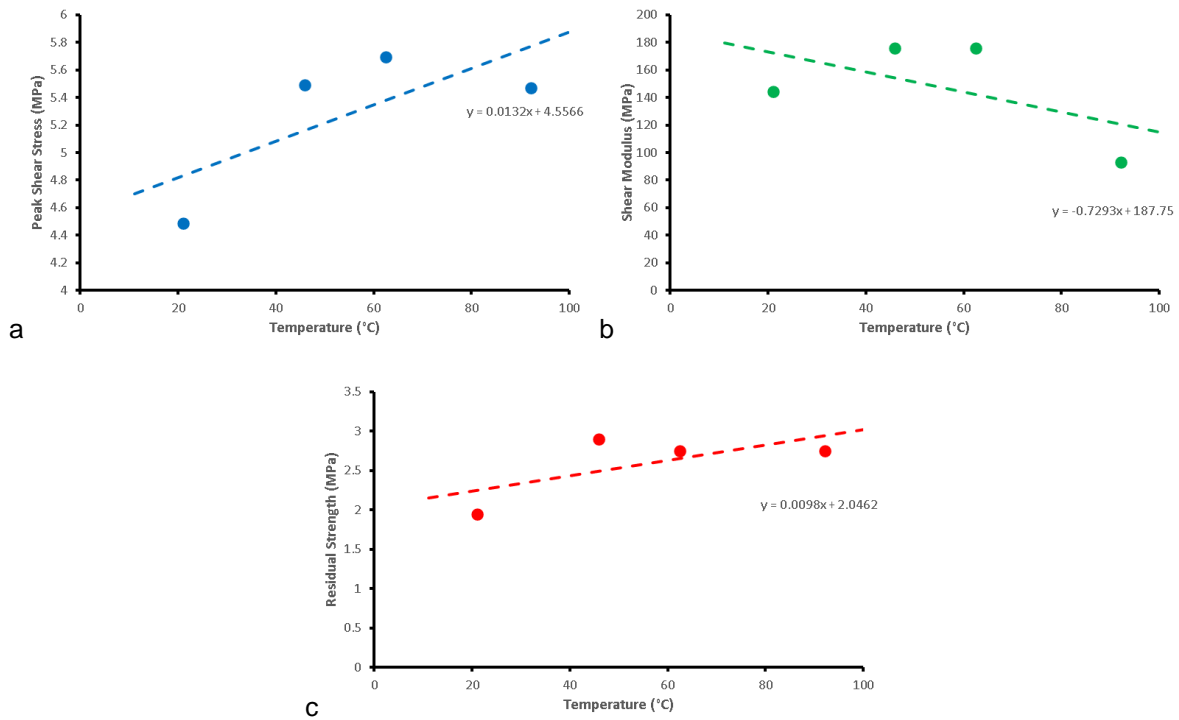


Figure 26 - Relationship between shear properties and temperature for Callovo-Oxfordian claystone. a) Peak shear strength; b) Shear modulus; c) Residual strength.

Figure 27 shows the result for self-sealing potential for Callovo-Oxfordian claystone. As shown, self-sealing potential because of water (SSP_{H_2O}) reduces in COx with increased temperature (Figure 27a). This is a marked reduction, with SSP_{H_2O} of 132 at 20 °C, reducing to 7 at 90 °C. That is nearly a two order in magnitude reduction in the effectiveness of self-sealing as a result of water flow. Therefore, at elevated temperatures the fractures are less likely to self-seal. Figure 27b also shows a reduction in self-sealing potential as a result of shear (SSP_{τ}). It must be noted that the spread in data is considerable and as a result is not yet clear whether this reduction is a considerable one, or a moderate one. The preliminary data for Callovo-Oxfordian claystone suggest that the favourable self-sealing properties of the rock reduce with temperature.

Two of the four tests conducted in Callovo-Oxfordian claystone need repeating because of problems encountered during repeat shearing. In addition, another four tests are required to describe the self-sealing properties for fractures formed at ambient temperatures. These additional six tests will expand the dataset and allow clearer statements to be made on the role temperature plays on shear properties and self-sealing potential in Callovo-Oxfordian claystone.

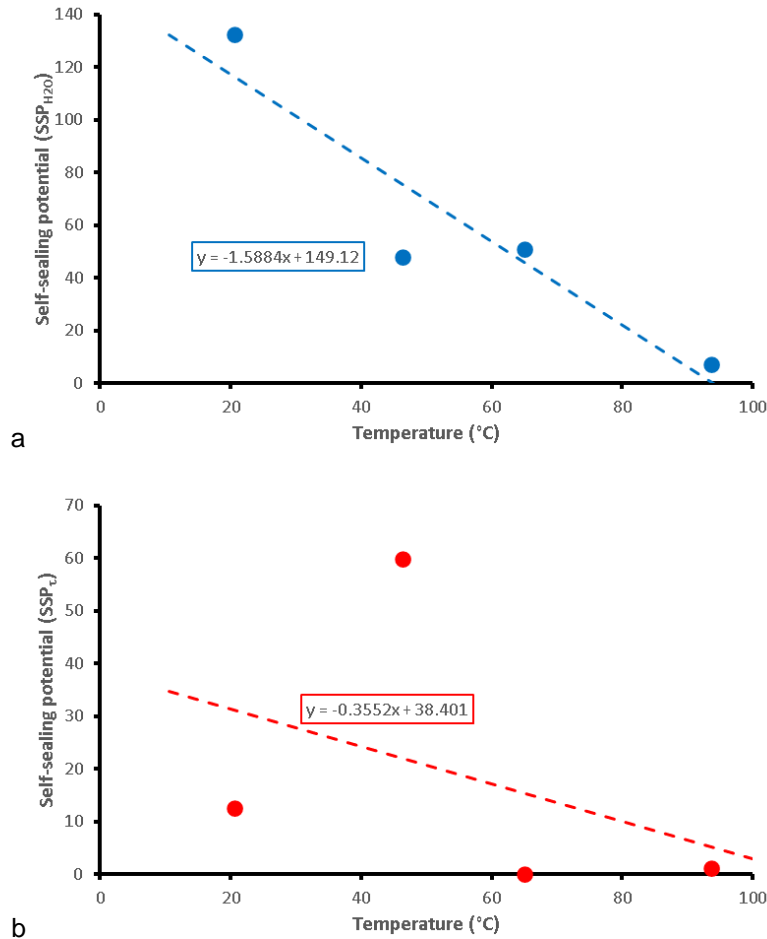


Figure 27 - Influence of temperature on self-sealing potential in Callovo-Oxfordian claystone. a) Self-sealing potential as a result of hydration; b) Self-sealing potential as a result of active shear.

4.2 Conclusion

At the time of reporting, a total of 13 of at least 21 shear experiments had been completed. The experimental programme was late to start because of the Covid-19 pandemic and delays to the modification of the apparatus. All planned experiments in Opalinus Clay had been completed, with enough experiments in Callovo-Oxfordian claystone to make statements about the influence of temperature on shear properties and flow. None of the experiments using Boom Clay had been conducted. Each experiment took around two weeks to complete. The initial shearing of intact samples took around 1 day, followed by one week of hydraulic flow into the fracture, and a further week with continued hydraulic flow while the sample was actively sheared.

Two repeatability tests were conducted in Opalinus Clay, with three further tests conducted at similar conditions. It can be concluded that repeatability in Opalinus Clay was not as good as hoped in direct

shear experiments. This means that considerable spread in data is seen. However, even considering the spread in data, relationships can be seen that show the influence of temperature.

Temperature was seen to have a considerable effect on the shear properties of Opalinus Clay. All tests showed elastic-brittle behaviour, with peak shear stress increasing by 0.47 MPa per 10 °C temperature. Residual strength also increased with temperature at a rate of 0.09 MPa per 10 °C. Shear modulus showed considerable spread in the data, but also showed an increase with temperature. The shear data were influenced by the test conducted at 65 °C that appears to have fractured prematurely because of an existing weakness in the sample. Repeat shear in Opalinus Clay also showed a clear increase in peak strength of 0.175 MPa per 10 °C and residual strength of 0.178 MPa per 10 °C. A small increase in shear modulus was seen but with considerable spread in the data. Therefore, in intact and re-sheared Opalinus Clay, strength and compliance increase with temperature. The increase was greater in intact OPA.

The influence of temperature on self-sealing processes in host rocks was the primary focus of the experimental study. Considerable variation was seen in the flowrate into the fracture that could not be described by fracture surface characteristics. Therefore, two different self-sealing potential (SSP) coefficients were defined: a) as a result of hydraulic flow along the fracture (SSP_{H_2O}); b) as a result of active shear along the fracture while hydraulic flow continued (SSP_{τ}). The SSP coefficient describes the proportional change in flow as opposed to the absolute change in flowrate.

Self-sealing potential was seen to change with temperature in Opalinus Clay. A clear relationship was seen with SSP_{H_2O} , with a reduction in self-sealing capacity with increasing temperature. At a temperature of 90 °C, the self-sealing potential was negligible. A difference was seen between SSP_{H_2O} for fractures that were formed at ambient temperature and those formed at temperature, although this may simply be explained by natural variation between samples. This result suggests that SSP_{H_2O} is better in fractures that have formed at temperature. This may be related to differences in fracture topology. Considerable spread of results was seen for self-sealing potential because of active shear (SSP_{τ}). However, a reduction in SSP_{τ} was seen with increasing temperature. In conclusion, for Opalinus Clay, the effectiveness of self-sealing processes reduces at elevated temperatures.

All fracture surfaces were laser scanned following the initial and re-shear stages of the experiment, giving four fracture topology scans per test. Little variation was seen in roughness characteristics for the initial shear samples, with a reduction in roughness seen during re-shear. For peak to valley height, an increase was seen with temperature for the initial shear samples, with a reduction seen for the re-shear tests. All three datasets suggest that little variation is seen in fracture topology for shear fractures created at different temperatures in initially intact samples. The presence of water during the re-shear phase results in the reduction in fracture roughness and peak to valley height. As self-sealing potential (SSP_{H_2O}) is a function of temperature, and fracture roughness alters with temperature, it is likely that fracture roughness plays a role in the effectiveness of fractures to self-seal.

The dataset for Callovo-Oxfordian claystone is incomplete at the time of reporting. However, four tests were completed at the four test temperatures to make preliminary statements about the role of temperature on self-sealing in Callovo-Oxfordian claystone. The stress-strain response of the four tests conducted over the full range of temperatures showed a similar form, although as temperature increased the response was more brittle. Peak strength was seen to increase by 0.13 MPa per 10 °C, with residual stress increasing by 0.01 MPa per 10 °C. Shear modulus reduced with temperature, although this result may be influenced by a low modulus seen at the highest temperature. Callovo-Oxfordian claystone therefore increases in strength with temperature but has a reducing stiffness.

Self-sealing processes in Callovo-Oxfordian claystone were seen to greatly change over the range of temperatures investigated. At ambient temperatures, SSP_{H_2O} of COx was 132 and reduced to just 7 at 90 °C. Therefore, a near two-order of magnitude reduction was seen in the effectiveness of self-sealing because of water flow was seen. A reduction was also seen in the effectiveness of self-sealing because of active shear (SSP_{τ}), although the reduction was not as marked as for water and the data showed

considerable spread. The preliminary data for Callovo-Oxfordian claystone suggest that the favourable self-sealing properties of the rock reduces with temperature and becomes almost negligible at 90 °C.

5. General conclusions

The present report “D7.3 - Technical report on thermal effects on near field properties” is the final deliverable for subtask 2.1. Laboratory experiments were performed on candidate clay host rocks to provide answers about the impact of temperature on the self-sealing processes. Different testing cells (triaxial, oedometric and shear ring) and monitoring tools (X-ray and neutron tomography) have been used by the different partners to analyse, at different test stages and temperatures, the evolution of crack volume and permeability of fractured samples due to water percolation. Only Callovo Oxfordian claystone (COx) and Opalinus clay (OPA) were studied up to now.

There are three main processes involved in the self-sealing process: intraparticle swelling due to crack resaturation, inter-particle swelling due to osmotic effects, plugging of fracture by particles aggregation. The mineralogical composition of the COx claystone influences the self-sealing process. Generally speaking, the self-sealing process is fast at the beginning (a few hours of a few days depending on the initial crack opening) of the test and then stabilizes with time (within a few weeks). Thanks to the self-sealing process, the permeability of the COx claystone samples is partially restored ($\sim 10^{-18}$ - 10^{-19} m²) compared to the initial permeability of the healthy (i.e., without fracture) claystone ($\sim 10^{-20}$ - 10^{-21} m²).

Many parameters could influence the efficiency of the self-sealing process which is defined by the rate and amplitude of decrease in the crack permeability and by the physical closure of the crack:

- First, the calcium carbonate content. The higher the calcium carbonate content (and therefore the lower the clay content), the less effective the self-sealing process, whatever the sample orientation (parallel or perpendicular). To have an effective sealing, it is necessary to have a carbonate content lower than 40%.
- Second, the sample orientation (parallel or perpendicular to the bedding plane). The clay sheets oriented in parallel to the initial artificial crack surfaces (lips), and then parallel to the cylindrical core sample axis and water flow direction, favour probably a faster swelling of crack surfaces. However, the influence of sample orientation is not obvious and it seems that the self-sealing process is equally efficient for both parallel and perpendicular orientations.
- Third, the opening of the initial artificial crack influences the kinetic of the self-sealing process. It is faster for tight cracks.
- Four, considering the material heterogeneity (variations in the calcite content) and experimental uncertainties, temperature doesn't seem to have a significant impact on the self-sealing process (permeability decrease and crack volume reduction). At low temperatures, quasi-instantaneous closure is favoured by the formation of a dense network of micro-cracks sub-parallel and close to the interface lips, creating a highly damaged material that fills the interface space. At high temperature (90 °C), the mechanism is more diffuse and secondary cracks are scattered, leading to a more gradual reclosure kinetics which is favoured by a greater diffuse swelling in the whole sample. Then, the crack closure mechanisms are more ductile at higher temperatures. However, the permeability decrease with time is not significantly impacted by the temperature.

To recreate in-situ conditions and analyse the stress effect on the self-sealing process, stress conditions have been introduced with shear experiments (initial shearing of intact samples, then hydraulic flow into the fracture, and finally further hydraulic flow with active shearing). Temperature was seen to have a considerable effect on the shear properties of both COx and Opalinus claystones (increase in peak strength, residual strength and shear modulus). In addition, the effectiveness of self-sealing processes as a result of hydration and shear was seen to reduce significantly at elevated temperatures. Indeed, fracture roughness, which plays likely a role in the effectiveness of fractures to self-seal, is reduced by the presence of water during the re-shear phase and by temperature.

In all these experiments, whatever the experimental conditions and material characteristics (temperature, sample orientation, crack width), self-sealing during water percolation is always an efficient mechanism if the clay content is high enough. This is all the more promising that the duration of the lab experiments is much shorter than the in-situ time scale. The effectiveness of self-sealing processes is only reduced at elevated temperatures if it is associated with significant crack shearing. These results give confidence to the positive impact of the self-sealing process on the restoration of the

initial sealing properties of the clay host rock, even though the effectiveness of self-sealing has still to be confirmed for the Boom clay. This physico-chemical mechanism will allow a good sealing of fractures in the EDZ during the resaturation of the underground structures for radioactive waste storage in clayey rocks, which will guarantee the safety of the site. However, these results have to be confirmed with additional similar experiments to better analyse the impact of some parameters on the self-sealing process. For example; in all the self-sealing experiments, synthetic solutions, which are supposed to be sufficiently chemically balanced with the rock to prevent any structural damage due to geochemical reactions, were used. If the activity (ionic strength) of these solutions is lower than the native porewater (in equilibrium with the interlayer water) then swelling by clays hydration can be the main mechanism to caused sealing in the lab experiments. However, EDZ fractures will be invaded in-situ with a porewater of ionic strength of the native porewater, not a lower ionic strength solution, and the self-sealing mechanism could be less efficient than in lab experiments. Therefore, it would be interesting in the future to know how the water activities compare and to perform self-sealing experiments with waters with different chemical composition to verify if the water chemistry has a significant influence on the self-sealing efficiency. This would also help with the assessment of how realistic a sealing mechanism is.

Acknowledgements

The experiments presented by CNRS(ULorraine) were carried out with the experimental devices available in the HGM experimental platform (Université de Lorraine-CNRS – <http://georessources.univ-lorraine.fr/fr/content/hydrogeomecanique>).

References

Andra. (2005). Dossier Argile 2005.

Armand, G., Conil, N., Talandier, J. and Seyedi, D.M. (2017) Fundamental aspects of the hydromechanical behaviour of Callovo-Oxfordian claystone: from experimental studies to model calibration and validation. *Computers and Geotechnics*, 85, pp.277-286.

ASTM Standard (2009) Standard guide for assessment of surface texture of non-porous biomaterials in two dimensions. F2791-09.

Auvray, C., Grgic, D., Morlot, C., Fourreau, E., & Talandier, J. (2015). X-Ray Tomography Applied to Self-Healing Experiments on Argillites. 13th ISRM International Congress of Rock Mechanics, Montréal, (Québec, Canada).

Bastiaens, W., Bernier, F., & Li, X. L. (2007). SELFRAC: Experiments and conclusions on fracturing, self-healing and self-sealing processes in clays. *Physics and Chemistry of the Earth, Parts A/B/C*, 32(8–14), 600–615. <https://doi.org/10.1016/j.pce.2006.04.026>.

Beerten, K, Leterme, B (2012) Physical geography of north-eastern Belgium – the Boom Clay outcrop and sub-crop zone SCK-CEN report ER-202 12/Kbe/P-2 60p.

Bernier, F, Li, XL, and Bastiaens, W (2007) Twenty-five years' geotechnical observation and testing in the Tertiary Boom Clay formation, *Géotechnique* 57(2) 229–237.

Blanchart, P, Faure, P, De Craen, M, Bruggeman, C, and Michels, R (2012) Experimental investigation on the role of kerogen and clay minerals in the formation of bitumen during the oxidation of Boom Clay, *Fuel* 97, 344–351.

Coll, C. (2005). Endommagement des roches argileuses et perméabilité induite au voisinage d'ouvrages souterrains [PhD Thesis]. Université Joseph-Fourier - Grenoble I.

Cuss, R.J., and Harrington, J.F. (2016) An experimental study of the potential for fault reactivation during changes in gas and porewater pressure. *International Journal of Greenhouse Gas Control*, 53, pp.41-55. DOI: 10.1016/j.ijggc.2016.07.028

Cuss, R.J., Harrington, J.F., Sathar, S., and Norris, S. (2015) An experimental study of the flow of gas along faults of varying orientation to the stress-field; Implications for performance assessment of radioactive waste disposal. *Journal of Geophysical Research – Solid Earth*. 120, pp.3932-3945, doi:10.1002/2014JB011333

Cuss, R.J., Harrington, J.F., Sathar, S., Norris, S., and Talandier, J. (2017) The role of the stress-path and importance of stress history on the flow of water along faults; an experimental study. *Applied Clay Science*, 150, pp.282-292, <https://dx.doi.org/10.1016/j.clay.2017.09.029>

Cuss, R.J., Milodowski, A., and Harrington, J.F. (2011) Fracture transmissivity as a function of normal and shear stress: first results in Opalinus clay. *Physics and Chemistry of the Earth*. 36, pp.1960-1971. DOI: 10.1016/j.pce.2011.07.080

Cuss, R.J., Milodowski, A.E., Harrington, J.F. and Noy, D.J. (2009) Fracture transmissivity test of an idealised fracture in Opalinus Clay. *British Geological Survey Commissioned Report*, CR/09/163. 74pp.

Cuss, R.J., Sathar, S., and Harrington, J.F. (2012) Fracture transmissivity test in Opalinus Clay; test conducted on a realistic fracture. *British Geological Survey Commissioned Report*, CR/12/132. 63pp.

Cuss, R.J., Wiseall, A.C., Dobbs, M.R., Parkes, D., Harrington, J.F., Talandier, J., and Bourbon, X. (2018) Experiments on interface processes at the cement/Callovo-Oxfordian Claystone interface and the impact on physical properties; Mechanical and flow properties of fresh interfaces. Proceedings of the 3rd Annual Workshop of the CEBAMA Project, Nantes, France, 17th-18th April, 2018. 10pp.

Cuss, R.J., Wiseall, A.C., Harrington, J.F., Talandier, J., and Bourbon, X. (2019) Experiments on interface processes at the cement/Callovo-Oxfordian claystone interface and the impact on physical properties; mechanical results from the Callovo-Oxfordian claystone. In Proceedings of the Second Workshop of the HORIZON 2020 CEBAMA Project (KIT Scientific Reports; 7752) (Vol. 7752, p. 41). KIT Scientific Publishing.

Cuss, R.J., Wiseall, A.C., Tamayo-Mas, E., and Harrington, J.F. (2018) An experimental study of the influence of stress history on fault slip during injection of supercritical CO₂. *Journal of Structural Geology*, 109, pp.86-98. <https://doi.org/10.1016/j.jsg.2018.01.006>.

De Craen, M, Wang, L, Van Geet, M, Moors, H (2004) Geochemistry of Boom Clay pore water at the Mol site, SCK-CEN-BL-990 04/MDC/P-48, SCK-CEN.

Dehandschutter, B, Vandycke, S, Sintubin, M, Vandenberghe, N, Gaviglio, P, Sizun, JP, Wouters, L, (2004) Microfabric of fractured Boom Clay at depth: a case study of brittle-ductile transitional clay behaviour, *Applied Clay Science*, 26(1-4) pp.389-401.

De La Vaissière, R., Armand, G., & Talandier, J. (2015). Gas and water flow in an excavation-induced fracture network around an underground drift: A case study for a radioactive waste repository in clay rock. *Journal of Hydrology*, 521, 141–156. <https://doi.org/10.1016/j.jhydrol.2014.11.067>.

Di Donna A., Charrier P., Dijkstra J., Andò E., Bésuelle P. (2022). The contribution of swelling to self-sealing of claystone studied through x-ray tomography, *Physics and Chemistry of the Earth, Parts A/B/C*, 127, 103191, doi: 10.1016/j.pce.2022.103191.

Escoffier, S. (2002). Caractérisation expérimentale du comportement hydromécanique des argilites de Meuse/Haute-Marne [PhD Thesis]. Institut National Polytechnique de Lorraine.

Gautschi, A. (2001) Hydrogeology of a fractured shale (Opalinus Clay): Implications for deep geological disposal of radioactive wastes. *Hydrogeology Journal*, 9, pp.97–107

Giot, R., Auvray, C., & Talandier, J. (2019). Self-sealing of claystone under X-ray nanotomography. *Geological Society, London, Special Publications*, 482(1), 213–223. <https://doi.org/10.1144/SP482.4>.

Giot, R., Giraud, A., & Auvray, C. (2014). Assessing the Permeability in Anisotropic and Weakly Permeable Porous Rocks Using Radial Pulse Tests. *Oil & Gas Science and Technology – Revue d'IFP Energies Nouvelles*, 69(7), 1171–1189. <https://doi.org/10.2516/ogst/2013146>.

Giot, R., Giraud, A., Auvray, C., Homand, F., & Guillon, T. (2011). Fully coupled poromechanical back analysis of the pulse test by inverse method. *International Journal for Numerical and Analytical Methods in Geomechanics*, 35(3), 329–359. <https://doi.org/10.1002/nag.897>.

Giot, R., Giraud, A., Guillon, T., & Auvray, C. (2012). Three-dimensional poromechanical back analysis of the pulse test accounting for transverse isotropy. *Acta Geotechnica*, 7(3), 151–165. <https://doi.org/10.1007/s11440-012-0158-7>.

Gratier, J. P., Jenatton, L., Tisserand, D., & Guiguet, R. (2004). Indenter studies of the swelling, creep and pressure solution of Bure argillite. *Applied Clay Science*, 26(1), 459–472. <https://doi.org/10.1016/j.clay.2003.12.035>.

Harrington, J.F., Cuss, R.J., and Talandier, J. (2017) Gas transport properties through intact and fractured Callovo-Oxfordian mudstones. In Rutter, E.H., Mecklenburgh, J. & Taylor, K.G. (eds) *Geomechanical and Petrophysical Properties of Mudrocks*. Geological Society, London, Special Publications, 454, <https://doi.org/10.1144/SP454.7>.

Homand, F., Giraud, A., Escoffier, S., Koriche, A., & Hoxha, D. (2004). Permeability determination of a deep argillite in saturated and partially saturated conditions. *International Journal of Heat and Mass Transfer*, 47(14), 3517–3531. <https://doi.org/10.1016/j.ijheatmasstransfer.2004.02.012>.

Honty, M., and De Craen, M. (2011) Boom Clay mineralogy – qualitative and quantitative aspects, SCK CEN contract: CO-90-08-2214-00 NIRAS/ONDRAF contract: CCHO 2009-0940000, Research Plan Geosynthesis.

Lefranc, M., Beaudoin, B., Chilès, J. P., Guillemot, D., Ravenne, C., & Trouiller, A. (2008). Geostatistical characterization of Callovo–Oxfordian clay variability from high-resolution log data. *Physics and Chemistry of the Earth, Parts A/B/C*, 33, S2–S13. <https://doi.org/10.1016/j.pce.2008.10.053>.

Mohajerani, M. (2011). Etude expérimentale du comportement thermo-hydro-mécanique de l'argillite du Callovo-Oxfordien [PhD Thesis]. Université Paris-Est.

Montes, H. G., Duplay, J., Martinez, L., Escoffier, S., & Rousset, D. (2004). Structural modifications of Callovo-Oxfordian argillite under hydration/dehydration conditions. *Applied Clay Science*, 25(3), 187–194. <https://doi.org/10.1016/j.clay.2003.10.004>.

Nuclear Energy Agency. (2010). Self-sealing of Fractures in Argillaceous Formations in the Context of Geological Disposal of Radioactive Waste. OECD Nuclear Energy Agency.

Pearson, F.J., Arcos, D., Bath, A., Boisson, J.Y., Fernandez, A.M., Gabler, H.E., Gaucher, E., Gautschi, A., Griffault, L., Hernan, P., Waber, H.N. (2003) Geochemistry of Water in the Opalinus Clay Formation at the Mont Terri Laboratory. Mont Terri Project Technical Report 2003-03

Pellenard, P., Tramoy, R., Pucéat, E., Huret, E., Martinez, M., Bruneau, L., & Thierry, J. (2014). Carbon cycle and sea-water palaeotemperature evolution at the Middle–Late Jurassic transition, eastern Paris Basin (France). *Marine and Petroleum Geology*, 53, 30–43. <https://doi.org/10.1016/j.marpetgeo.2013.07.002>.

Robinet, J.-C., Sardini, P., Coelho, D., Parneix, J.-C., Prêt, D., Sammartino, S., Boller, E., & Altmann, S. (2012). Effects of mineral distribution at mesoscopic scale on solute diffusion in a clay-rich rock: Example of the Callovo-Oxfordian mudstone (Bure, France). *Water Resources Research*, 48(5). <https://doi.org/10.1029/2011WR011352>.

Robinet, J.-C., Sardini, P., Siitari-Kauppi, M., Prêt, D., & Yven, B. (2015). Upscaling the porosity of the Callovo-Oxfordian mudstone from the pore scale to the formation scale; insights from the 3H-PMMA autoradiography technique and SEM BSE imaging. *Sedimentary Geology*, 321, 1–10. <https://doi.org/10.1016/j.sedgeo.2015.02.007>.

Rousset, D. and Clauer, N. (2003) Discrete clay diagenesis in a very low-permeable sequence constrained by an isotopic (K–Ar and Rb–Sr) study. *Contributions to Mineralogy and Petrology*, 145(2), pp.182-198.

Sammartino, S., Bouchet, A., Prêt, D., Parneix, J.-C., & Tevissen, E. (2003). Spatial distribution of porosity and minerals in clay rocks from the Callovo-Oxfordian formation (Meuse/Haute-Marne, Eastern France)—Implications on ionic species diffusion and rock sorption capability. *Applied Clay Science*, 23(1), 157–166. [https://doi.org/10.1016/S0169-1317\(03\)00098-X](https://doi.org/10.1016/S0169-1317(03)00098-X).

Stamati O., Andò E., Roubin E., Cailletaud R., Wiebicke M., Pinzon G., Couture C., Hurley R.C., Caulk R., Caillerie D., Matsushima T., Bésuelle P., Bertoni F., Arnaud T., Ortega Laborin A., Rorato R., Sun Y., Tengattini A., Okubadejo O., Colliat J.-B., Saadatfar M., Garcia F.E., Papazoglou C., Vego I., Brisard S., Dijkstra J., Birmpilis G., 2020, spam: Software for Practical Analysis of Materials, *Journal of Open Source Software*, vol. 5 n° 51, p. 2286, doi:10.21105/joss.02286

Stavropoulou E, Andò E, Roubin E, Lenoir N, Tengattini A, Briffaut M and Bésuelle P (2020). Dynamics of Water Absorption in Callovo-Oxfordian Claystone Revealed With Multimodal X-Ray and Neutron Tomography. *Front. Earth Sci.* 8:6, doi: 10.3389/feart.2020.00006.

- Van Geet, M., Bastiaens, W., & Ortiz, L. (2008). Self-sealing capacity of argillaceous rocks: Review of laboratory results obtained from the SELFRAC project. *Physics and Chemistry of the Earth, Parts A/B/C*, 33, S396–S406. <https://doi.org/10.1016/j.pce.2008.10.063>.
- Vis, GJ, and Verweij, JM. (2014) Geological and geohydrological characterization of the Boom Clay and its overburden, OPERA-TNO 411 Technical Report.
- Wemaere, I, Marivoet, J, and Labat, S (2008) Hydraulic conductivity variability of the Boom Clay in north-east Belgium based on four core drilled boreholes, *Physics and Chemistry of the Earth, Parts A/B/C* 33 24-36.
- Wiseall, A.C., Cuss, R.J., Hough, E, and Kemp, S.J. (2018) The role of fault gouge properties on fault reactivation during hydraulic stimulation; an experimental study using analogue faults. *Journal of Natural Gas Science and Engineering*, 59, pp.21-34 <https://doi.org/10.1016/j.jngse.2018.08.021>
- Wong, T, Batjes, DAJ, and de Jager, J, (Eds.; 2007) *Geology of the Netherlands*. Herent: Royal Netherlands Academy of Arts and Sciences.
- Yu, HD, Chen, WZ, Jia, SP, Cao, JJ, and Li, XL (2012), Experimental study on the hydro-mechanical behaviour of Boom clay, *International Journal of Rock Mechanics and Mining Sciences* 53 159-165.
- Yven, B., Sammartino, S., Géraud, Y., Homand, F., and Villiéras, F. (2007) Mineralogy, texture and porosity of Callovo-Oxfordian argillites of the Meuse/Haute-Marne region (eastern Paris Basin). *Mémoires de la Société géologique de France*, 178, pp.73–90.